NO_x Emissions Modelling of Turbofan Engines through Chemical Reactor Network

Master Thesis Aerospace Engineering

Juliet Sophie Huiskes

Cover image: Ansel Huang (Unsplash) [1]

Delft University of Technology

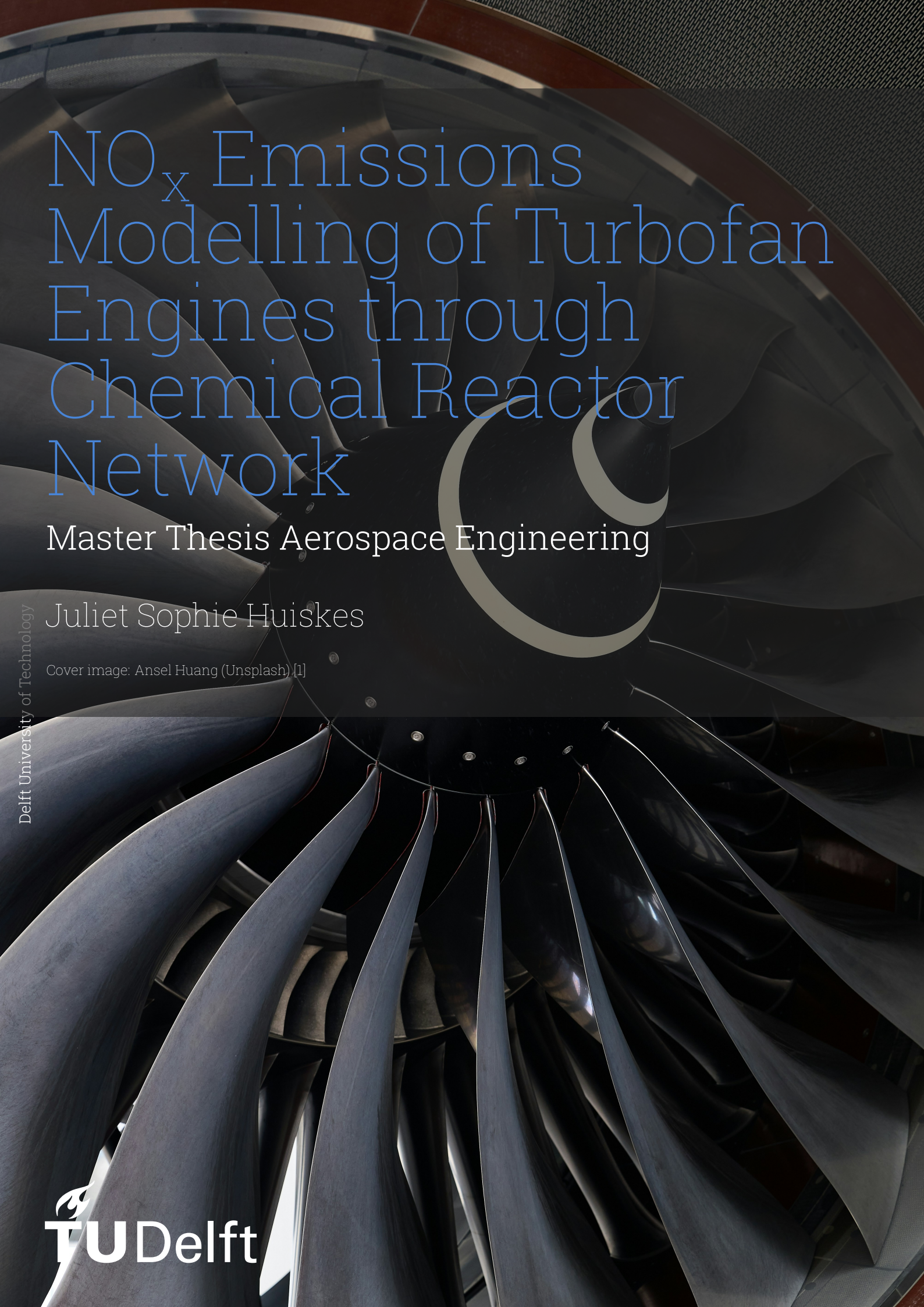

TU Delft

NO_x Emissions Modelling of Turbofan Engines through Chemical Reactor Network

by

Juliet Sophie Huiskes
Student number: 4532856

to obtain the degree of
Master of Science

at the Delft University of Technology,
to be defended publicly on Thursday, December 18, 2025 at 9:00.

Supervisors:	Prof. A. Gangoli Rao
	Dr. F. Yin
Daily supervisor:	T. Eker

Thesis Committee:	Prof. A. Gangoli Rao,	TU Delft, Supervisor
	Dr. F. Yin,	TU Delft, Chair
	Dr. P. P. Sundaramoorthy,	TU Delft, Examiner
	T. Eker,	TU Delft, Additional

An electronic version of this thesis is available at `http://repository.tudelft.nl/`.

TU Delft

Acknowledgements

I would like to thank the people who supported me throughout this thesis.

I am very grateful to Turhan for his continuous help, explanations and patience. I also thank Arvind and Feijia for giving me the opportunity to work on this topic and for their guidance when it was needed.

A big thanks goes to my boyfriend Sahil, who supported me in every possible way. He encouraged me throughout this entire process and listened to endless stories about my thesis, even when the technical parts made no sense to him. Whenever things became too stressful, he would spoil me by picking up food so I could take a break and relax. Having someone who always showed interest, care and patience made this journey so much easier.

I want to thank my dad, whose unwavering support has been one of the foundations that allowed me to reach this point. He always welcomed me back home to Aruba whenever I needed a break, giving me the space to recover and feel grounded again. I also wish to acknowledge my mom for her role in shaping the path that led me here.

I am grateful to my sister Georgia, who has always been there for me and with whom I had long weekly calls that made all the difference during stressful periods. I also want to thank my best friend Lucy, whose friendship and perfectly timed distractions brought me calm and laughter when I needed it most.

I am thankful as well for Matthijs and Lucas, who were my closest friends throughout my mechanical engineering years. I missed their unseriousness and all the joking around more than they know, especially during the intense moments of this master.

I also want to thank the friends I made during the master. Katarina became both an academic and a personal friend, and her support and company meant a great deal to me, especially when I first transitioned from mechanical to aerospace engineering. And a special mention goes to Jeff, who is overseas and still sends me Dutch memes to this day.

To all of you, thank you for supporting me along the way.

Juliet Sophie Huiskes
Delft, December 2025

Abstract

This thesis develops a chemical reactor network (CRN) model for an RQL aero-engine combustor and uses it to study water injection and NO_x formation across realistic operating conditions. The model includes parallel primary-zone subzones to represent mixture inhomogeneity, detailed gas-phase chemistry and residence-time based zone sizing. It is validated against ICAO LTO emissions for the CF6-80C2B1F and Trent XWB-84 and reproduces the expected NO_x and CO trends, including the idle CO peak.

For each operating point, the combustor geometry is kept fixed while the primary-zone equivalence ratios and the mixing parameter are optimised. This same methodology is applied at cruise using cruise-specific inlet conditions. The CRN predicts NO_x within the measured in-flight range; BFFM2 also falls within this band, while P3T3 remains close to it. Only the CRN resolves the internal mixture structure and reaction pathways.

Water-to-fuel sweeps show that water injection consistently reduces NO_x, with the strongest effect at high thrust where baseline temperatures are highest. CO increases mainly at idle and approach due to lower burnout temperatures. Reaction-pathway analysis confirms that thermal NO remains the dominant mechanism and that water suppresses existing pathways by reducing temperature and radicals.

Overall, the CRN provides an accurate and computationally efficient framework for analysing water injection and predicting emissions at both LTO and cruise, while resolving the internal combustor processes that are inaccessible to simpler correlation-based methods.

Contents

List of Figures

List of Tables

Nomenclature

Abbreviations

Abbreviation	Definition
AP	Approach operating point
BFFM2	Boeing Fuel Flow Method 2 correlation
CAEP	Committee on Aviation Environmental Protection (ICAO technical committee)
CF6	GE CF6-80C2B1F turbofan engine
CO	Carbon monoxide
CO_2	Carbon dioxide
C/O	Climb-out operating point
CR60	Cruise operating point at 60 kN
CR70	Cruise operating point at 70 kN
CRN	Chemical Reactor Network
DNS	Direct Numerical Simulation
DZ1	Dilution zone 1
DZ2	Dilution zone 2
EASA	European Union Aviation Safety Agency (EU aviation regulator)
EI	Emission index
FAA	Federal Aviation Administration (United States aviation authority)
HC	Unburned hydrocarbons
ICAO	International Civil Aviation Organization
ID	Idle operating point
ISA	International Standard Atmosphere
LES	Large-Eddy Simulation
LTO	Landing and Take-Off cycle
NO	Nitric oxide
NO_2	Nitrogen dioxide
NO_x	Oxides of nitrogen
nvPM	Non-volatile particulate matter
P3T3	Correlation based on combustor inlet pressure and temperature
PDF	Probability density function
PSR	Perfectly stirred reactor
PZ1	Primary zone 1
PZ2	Primary zone 2
RANS	Reynolds-Averaged Navier-Stokes
RQL	Rich-Quench-Lean combustor
SZ	Secondary zone
T/O	Take-off operating point
XWB-84	Rolls-Royce Trent XWB-84 turbofan engine

Symbols

Symbol	Definition	Unit
A/F	Air-fuel mass ratio	–
A/F_{st}	Stoichiometric air-fuel ratio	–
c_p	Specific heat at constant pressure	$\text{J}\,\text{kg}^{-1}\,\text{K}^{-1}$
d	Characteristic injector or mixing length scale	m
Da	Damköhler number	–
E	Emission index	$\text{g}\,\text{kg}^{-1}$ fuel
EI_{CO}	CO emission index	$\text{g}\,\text{kg}^{-1}$ fuel
EI_{NO_x}	NO_x emission index	$\text{g}\,\text{kg}^{-1}$ fuel
F	Net thrust	kN
h	Specific enthalpy	$\text{J}\,\text{kg}^{-1}$
L_m	Mixing length scale	m
m	Mass	kg
$\dot{m}$	Mass flow rate	$\text{kg}\,\text{s}^{-1}$
$\dot{m}_{\text{fuel}}$	Fuel mass flow rate	$\text{kg}\,\text{s}^{-1}$
$\dot{m}_{\text{air}}$	Air mass flow rate	$\text{kg}\,\text{s}^{-1}$
$\dot{m}_{\text{H}_2\text{O}}$	Injected water mass flow	$\text{kg}\,\text{s}^{-1}$
P	Pressure (static or total)	Pa
P_3	Compressor outlet (combustor inlet) pressure	Pa
Q_{LHV}	Lower heating value of the fuel	$\text{J}\,\text{kg}^{-1}$ fuel
s	Unmixedness (mixing) parameter	–
T	Temperature	K
T_3	Compressor outlet temperature	K
T_{ad}	Adiabatic flame temperature	K
V_{zone}	Reactor zone volume	m^3
w_i	Quadrature weight of subzone i	–
X_i	Mole fraction of species i	–
Y_i	Mass fraction of species i	–
δ	Non-dimensional ambient pressure ratio	–
ϕ	Local equivalence ratio	–
$\bar{\phi}$	Mean equivalence ratio	–
ϕ_{PZ1}	Equivalence ratio in primary zone 1	–
ϕ_{PZ2}	Equivalence ratio in primary zone 2	–
ϕ_{SZ}	Equivalence ratio in the secondary zone	–
ϕ_{DZ1}	Equivalence ratio in dilution zone 1	–
σ	Standard deviation of equivalence-ratio distribution	–
τ	Residence time	s
τ_{ref}	Reference residence time	s
τ_{num}	Numerically measured residence time	s
τ_q	Quench time scale	s
τ_{chem}	Chemical time scale	s
$\lambda_{w/f}$	Water-to-fuel mass ratio	–

1

Introduction

Aviation enables global mobility and economic development, but it also contributes to anthropogenic climate forcing and local air-quality degradation [2], [3]. Although aircraft account for only a few percent of global emissions, their exhaust is released at high altitude, where it exerts disproportionate chemical and radiative impacts on the atmosphere [4]. To sustain the continued growth of air transport in an environmentally responsible way, the reduction of combustion emissions has become one of the most important challenges in propulsion research.

In the exhaust of gas-turbine engines, NO_x and CO are of particular concern [5], [6]. NO_x affects both tropospheric ozone formation and radiative forcing [4], while CO indicates incomplete oxidation and affects air quality near airports [3]. Modern aero-engine combustors must therefore balance low emissions with reliable operation over a wide range of power settings and ambient conditions. This is not a trivial task: lower flame temperatures suppress NO_x but can slow CO oxidation, and lean operation tends to reduce efficiency and stability [7]. These trade-offs define the physical limits of current combustor technology [5].

Most civil aero-engines use the *Rich-burn, Quick-quench, Lean-burn* (RQL) combustor configuration to achieve acceptable emissions while maintaining stability and efficiency [5], [8]. In this concept, combustion begins in a fuel-rich primary zone, is rapidly mixed with air in a quench region, and continues in a lean secondary and dilution zone [5]. This sequence lowers peak temperature and oxygen availability, reducing thermal NO_x production compared with older single-zone designs [6]. Nevertheless, further emission reductions within this framework are difficult because the mechanisms that control NO_x and CO formation depend sensitively on local equivalence ratio, temperature, and residence time [6], [7].

One promising approach to overcome these limitations is water injection [9]. Introducing water into the combustor increases the heat capacity of the mixture and lowers flame temperature, directly suppressing the thermal NO_x pathway [10]. Water injection also alters the distribution of radicals and can influence the oxidation of CO and unburned hydrocarbons [11]. While its basic effect on temperature is well established, the overall balance between NO_x reduction, CO emissions, and combustion stability under realistic engine conditions remains uncertain. Understanding these coupled effects is necessary to evaluate whether water injection can contribute meaningfully to the development of cleaner propulsion systems [9].

At the same time, the ability to predict emissions accurately across operating conditions is becoming increasingly important. Experimental data are limited to a few power settings [12], and high-fidelity computational fluid-dynamics simulations with detailed chemistry are too costly for full engine studies [13]. Low-order chemical reactor networks offer an alternative: they capture the dominant physics and chemistry at manageable computational cost and allow systematic exploration of design and operating parameters [14]. However, such models are typically validated at ground conditions and their extrapolation to cruise or altitude operation remains challenging.

1.1. Knowledge Gap

Despite significant progress in combustor design and modelling, important questions remain unanswered [15]. The quantitative impact of water injection on NO_x and CO emissions across the full range of operating conditions has not been established [9]. While experiments and simplified analyses show clear NO_x reduction with added water [10], the associated changes in CO and flame behaviour are less predictable [11]. Moreover, current predictive models seldom extend beyond the landing-take-off regime, leaving the effect of altitude and cruise operation largely unexplored. A consistent modelling framework that connects these regimes and explains the underlying formation mechanisms is still lacking.

1.2. Research Questions

This thesis addresses these gaps through detailed reactor-network modelling of an aero-engine RQL combustor with and without water injection. The main research question guides the work:

What is the effect of water injection on NO_x emissions in an aero-engine combustor across operating conditions?

The following sub questions help in answering the main question:

1. How can predictive modelling be extended to cruise conditions despite limited experimental data for validation?
2. What is the extent of NO_x emission reduction achievable with water injection at different operating conditions?
3. What are the dominant pathways and mechanisms of NO_x formation under water-injected conditions in an RQL combustor?

1.3. Report Structure

This thesis is organised to guide the reader from the background and motivation of the study to the development, validation and application of the CRN model. Chapter 2 introduces RQL combustion, NO_x formation mechanisms and relevant measurement information. Chapter 3 describes the CRN framework, including the parallel primary-zone subzones, residence-time formulation and implementation of water injection. The performance of the CRN is evaluated in Chapter 4 through validation against CF6 and XWB LTO emissions and available cruise data. Chapter 5 summarises two commonly used engineering methods (P3T3 and BFFM2) for comparison. Chapter 6 presents the main results of this thesis, including dry operation, water-injection sweeps and reaction-pathway analysis. The findings are interpreted in Chapter 7, followed by the conclusions and answers to the research questions in Chapter 8. Recommendations for future work are given in Chapter 9.

2

Theoretical Background

2.1. Fundamentals of Hydrocarbon Combustion

Combustion in aero-engine combustors is controlled by the interplay between fuel chemistry, local mixture composition, temperature and the residence time available for reactions. Although practical flames involve complex turbulence-chemistry interaction, their behaviour is well understood in terms of a few core variables: the equivalence ratio, ϕ, the structure of the radical pool, heat-release pathways and the time scales governing oxidation. This section summarises the essential concepts needed to interpret the behaviour of an RQL combustor and the chemical-reactor-network model employed in this work.

2.1.1. Mixture strength and stoichiometry

Jet-A is a mixture of hydrocarbons that can be represented generically by $C_\nu H_\mu$. Complete stoichiometric combustion with air requires

$$C_\nu H_\mu + \left(\nu + \frac{\mu}{4}\right) O_2 \;\rightarrow\; \nu CO_2 + \frac{\mu}{2} H_2O.$$

Because air contains nitrogen, the corresponding stoichiometric air-fuel ratio is

$$\left(\frac{A}{F}\right)_{\text{st}} = \frac{4\nu + \mu}{\nu}\,\frac{M_{\text{air}}}{M_{O_2}}.$$

Local mixture strength is quantified through the equivalence ratio,

$$\phi = \frac{(F/A)_{\text{actual}}}{(F/A)_{\text{st}}}.$$

Rich mixtures correspond to $\phi > 1$ and contain insufficient oxygen for full oxidation, while lean mixtures ($\phi < 1$) contain excess air. The temperature and composition of the flame depend strongly on ϕ: rich mixtures form large pools of intermediate radicals, stoichiometric mixtures achieve the highest flame temperatures, and lean mixtures stabilise at lower temperatures with slower oxidation rates.

2.1.2. Adiabatic flame temperature

In an adiabatic, well-mixed system, the temperature rise is governed by a global energy balance,

$$T_{\text{ad}} \approx T_{\text{in}} + \frac{\dot{m}_f Q_{\text{LHV}}}{\sum_i \dot{m}_{p,i}\,\bar{c}_{p,i}},$$

where T_{in} is the inlet mixture temperature and $\bar{c}_{p,i}$ are mean specific heats of the combustion products. The adiabatic flame temperature peaks near $\phi \approx 1$ because both radical concentrations and heat-release efficiency are maximal in this regime. This dependence underpins the behaviour of thermal NO formation.

When water is injected upstream of the flame, an additional heat-capacity term $\dot{m}_w c_{p,w}$ is added to the denominator, reducing the temperature rise. The resulting temperature suppression alters the NO-CO trade-off discussed later.

2.1.3. Chain-branching and radical pool formation

Hydrocarbon oxidation proceeds through a radical chain mechanism. Although hundreds of reactions may be involved in a detailed mechanism, the core structure can be summarised in three stages:

1. **Initiation.** Small amounts of radicals are produced by thermal dissociation or reaction of the parent fuel:
$$\mathrm{RH} \rightarrow \mathrm{R} + \mathrm{H}.$$
2. **Chain branching.** These radicals drive the high-temperature acceleration of the flame through reactions such as
$$\mathrm{H} + \mathrm{O_2} \rightarrow \mathrm{O} + \mathrm{OH}, \qquad \mathrm{O} + \mathrm{H_2} \rightarrow \mathrm{H} + \mathrm{OH}.$$
The resulting pool of H, O and OH largely determines the rate of oxidation.
3. **Termination.** At lower temperatures or with excess air, radicals recombine:
$$\mathrm{H} + \mathrm{OH} + \mathrm{M} \rightarrow \mathrm{H_2O} + \mathrm{M}.$$
This reduces the overall reaction rate.

The concentration of OH is especially important because it governs the conversion of CO to CO_2. Reaction pathways for major intermediates depend on temperature, pressure and ϕ, which explains the zone-dependent chemistry observed in rich, quench and lean regions of an RQL combustor.

2.1.4. Fuel oxidation sequence and main intermediates

Hydrocarbon fuels typically follow a staged oxidation sequence:

$$\text{Fuel} \rightarrow \text{alkyl radicals} \rightarrow \text{oxygenated radicals} \rightarrow \mathrm{CO} \rightarrow \mathrm{CO_2}.$$

The transformation to CO is fast under most aero-engine conditions, whereas the final conversion from CO to CO_2 is comparatively slow and requires a strong OH pool:

$$\mathrm{CO} + \mathrm{OH} \rightarrow \mathrm{CO_2} + \mathrm{H}.$$

This pathway is rate-controlling in the lean and dilution zones and is strongly temperature dependent. Hence, CO emissions reflect both the thermal history and the available residence time.

2.1.5. Time scales and the Damköhler number

Combustion behaviour is governed by the competition between mixing, convection and chemical time scales. A characteristic flow time for any zone is

$$\tau = \frac{\rho V}{\dot{m}},$$

while the chemical time τ_{chem} depends on the dominant reaction rate for that mixture. Their ratio is expressed through the Damköhler number:

$$\mathrm{Da} = \frac{\tau}{\tau_{\mathrm{chem}}}.$$

Large Da indicates kinetically fast chemistry that can approach equilibrium within the available residence time. Small Da corresponds to kinetically limited conditions, incomplete oxidation and, at the extreme, lean blowout.

The RQL concept manipulates Da by selecting different ϕ and temperature conditions in each zone, exploiting the rapid chemistry of rich mixtures while minimising time spent near stoichiometry and ensuring sufficient lean residence time for CO burnout.

2.1.6. Summary

The core elements of combustion physics relevant to this work therefore include the strong dependence of temperature and radical chemistry on mixture strength, the staged oxidation from fuel to CO_2, and the control exercised by flow and chemical time scales. These principles underpin the pollutant formation mechanisms and motivate the zone-based architecture of RQL combustors.

2.2. Pollutant Formation Mechanisms

The formation of CO and NO_x in gas-turbine combustors is determined by the local mixture strength, temperature history and the time available for oxidation. Although detailed mechanisms involve hundreds of reactions, their behaviour in practical aero-engine flames can be interpreted through a small set of dominant pathways. The descriptions below summarise the mechanisms relevant to hydrocarbon-air combustion without fuel-bound nitrogen, based on established gas-turbine combustion studies [15], [16].

2.2.1. Nitrogen-oxide formation pathways

Nitrogen oxides in gas-turbine exhaust consist primarily of nitric oxide (NO), with smaller fractions of nitrogen dioxide (NO_2) formed by post-flame oxidation. Several kinetic routes contribute to NO formation in hydrocarbon combustion, the relative importance of which depends on temperature, equivalence ratio and pressure. For fuels without chemically bound nitrogen, the dominant mechanisms are:

1. the thermal or Zeldovich mechanism,
2. the prompt (Fenimore) mechanism,
3. the N_2O-intermediate mechanism,
4. the NNH mechanism.

These mechanisms are well established in jet-engine studies and form the basis of contemporary NO_x modelling [15].

Thermal NO (Zeldovich mechanism)

At the high temperatures reached near stoichiometric conditions, atmospheric nitrogen reacts with O, O_2 and OH through the extended Zeldovich sequence:

$$N_2 + O \rightleftharpoons NO + N, \tag{2.1}$$

$$N + O_2 \rightleftharpoons NO + O, \tag{2.2}$$

$$N + OH \rightleftharpoons NO + H. \tag{2.3}$$

The first reaction has the highest activation energy and therefore controls the overall rate. Because both the reaction rate and the concentration of atomic oxygen increase rapidly with temperature, thermal NO formation grows approximately exponentially with T. Maximum formation occurs on the slightly lean side of stoichiometry, where sufficient oxygen is available to sustain rapid oxidation despite slightly lower flame temperatures.

Prompt NO (Fenimore mechanism)

Prompt NO forms at the leading edge of the flame front, within very short residence times. It originates from reactions of small hydrocarbon radicals, primarily CH, with molecular nitrogen:

$$N_2 + CH \rightarrow HCN + N, \tag{2.4}$$

$$N_2 + C \rightarrow CN + N. \tag{2.5}$$

The intermediate species (HCN, CN, NCN) are then rapidly oxidised by O and OH to form NO. Because these radicals exist only in a thin layer at the flame front, prompt NO is most pronounced in moderately rich conditions where CH production is high. This mechanism explains the non-zero NO concentration observed when extrapolating measured NO back to zero residence time in laminar-flame experiments and is especially relevant in rich primary zones of aero engines.

N_2O-intermediate mechanism

At lower temperatures or under lean conditions, the reaction of N_2 with O in the presence of a third body M forms nitrous oxide:

$$N_2 + O + M \rightleftharpoons N_2O + M. \tag{2.6}$$

N_2O is short-lived at gas-turbine pressures and reacts primarily via

$$N_2O + O \rightarrow NO + NO, \tag{2.7}$$

producing two NO molecules.

Because this route requires a third body and has relatively low activation energy, it can dominate NO formation at low temperature, high pressure or lean operation, such as at idle and approach power.

NNH pathway

Another low-temperature route proceeds through the NNH intermediate:

$$N_2 + H \rightarrow NNH, \tag{2.8}$$

$$NNH + O \rightarrow NO + NH. \tag{2.9}$$

This mechanism becomes relevant when atomic hydrogen is available but temperatures are insufficient to sustain rapid Zeldovich kinetics. It shares some common intermediates with prompt NO and increases in importance under rich conditions. At high temperature, competing reactions convert NNH to N_2 or N_2O, reducing its net contribution.

For modern aero-engines operating at high pressure, thermal NO formation via the extended Zeldovich mechanism overwhelmingly dominates total NO, as confirmed both experimentally and through detailed kinetic models.

2.2.2. Carbon-monoxide formation and oxidation

CO is an inevitable intermediate in hydrocarbon oxidation. Its concentration in the exhaust depends on where and how the fuel-air mixture transitions through the reaction sequence

$$\text{Fuel} \rightarrow CO \rightarrow CO_2.$$

Formation routes

CO forms for two main reasons:

- **Rich conditions:** insufficient oxygen availability leads to incomplete oxidation of the fuel. Large hydrocarbon fragments and oxygenated radicals decompose to CO before complete conversion to CO_2 is possible.
- **Lean or moderate conditions at high temperature:** CO_2 partially dissociates to CO via

$$CO_2 + M \rightleftharpoons CO + O + M.$$

Both effects are observed in practical combustors: rich primary zones generate CO through incomplete oxidation, while lean post-flame regions can re-generate CO thermally if temperatures remain high.

Oxidation to CO_2

The dominant oxidation route is

$$CO + OH \rightarrow CO_2 + H,$$

which makes CO burnout strongly dependent on the local OH pool. Slower, temperature-sensitive channels involving HO_2 contribute in cooler or leaner regions:

$$CO + HO_2 \rightarrow CO_2 + OH, \tag{2.10}$$

$$H + O_2 + M \rightarrow HO_2 + M. \tag{2.11}$$

Because all of these reactions slow sharply with decreasing temperature, CO emissions are particularly sensitive to the lean-zone residence time and the thermal impact of dilution or water injection. Lower temperatures reduce NO formation but can leave too little time or radical availability for completing CO oxidation.

2.3. Reaction Mechanisms and Kinetic Modelling

Accurate prediction of NO_x and CO emissions in a Chemical Reactor Network requires a kinetic scheme that resolves the dominant high-temperature oxidation and nitrogen pathways. In this work the *original* Jet-A surrogate mechanism developed by Dagaut [17], [18] is used. This mechanism was formulated and validated using shock-tube and jet-stirred reactor (JSR) experiments on kerosene oxidation over a wide temperature interval relevant to aero-engine combustors.

2.3.1. The Dagaut mechanism

Dagaut's mechanism represents Jet-A using a surrogate consisting of key hydrocarbon classes found in aviation fuels. The oxidation chemistry follows the canonical high-temperature pathways of kerosene oxidation: hydrogen abstraction, β-scission, oxygen addition, and the formation and consumption of the major radical pool (H, O, OH). The Dagaut kerosene mechanism has been validated against Jet-Stirred Reactor data over roughly 800-1300 K and 1-40 bar, Rapid-Compression-Machine data down to $\tilde{6}50$ K, and shock-tube data up to 1800 K at low to intermediate pressures [17].

Nitrogen chemistry is included through the classical thermal and NNH routes, enabling prediction of NO under fuel-rich and fuel-lean conditions. The core reactions,

$$O + N_2 \rightarrow NO + N, \tag{2.12}$$

$$N + O_2 \rightarrow NO + O, \tag{2.13}$$

$$N + OH \rightarrow NO + H, \tag{2.14}$$

constitute the high-temperature Zeldovich paths known to dominate NO formation above roughly 1500 K [7], [19]. The mechanism therefore captures the main sensitivities of thermal NO to temperature, equivalence ratio and residence time in the RQL architecture.

The version used in this thesis is the *original* Dagaut Jet-A surrogate mechanism, not the later high-pressure extensions published after the mid-2000s. Its suitability for the present RQL CRN is supported by three aspects well documented in the literature:

1. **Experimentally anchored surrogate formulation.** The surrogate and oxidation scheme reproduce global kerosene oxidation trends and major-species behaviour in shock-tube and JSR studies [17], [18].
2. **Explicit treatment of high-temperature NO pathways.** The mechanism includes the necessary thermal and NNH reactions that dominate NO formation in rich primary zones and during the quench-lean transition [7], [19].
3. **Computational feasibility for multi-zone CRNs.** Compared to very large mechanisms (e.g. Jet-Surf, HyChem), the original Dagaut scheme contains far fewer species while retaining the routes most relevant to high-temperature NO and CO. This makes it well suited for parallel architectures and large sweeps [20], [21].

Two limitations of the Dagaut mechanism should be noted when interpreting CRN results:

- **No low-temperature chemistry.** Negative-temperature-coefficient (NTC) behaviour and two-stage ignition pathways are not included. This is not a limitation for the present work because RQL combustors operate at high temperature.
- **No soot precursor or PAH growth chemistry.** This is acceptable since soot is not modelled and the study focuses on NO_x, CO and the effect of water injection.

In summary, the original Dagaut Jet-A surrogate mechanism offers an appropriate balance between physical fidelity and computational efficiency for predicting NO_x and CO formation in an RQL combustor model across multiple operating conditions.

2.4. Rich-Quench-Lean Combustion Fundamentals

The rich-quench-lean (RQL) concept structures combustion into three axial regions with distinct equivalence ratios, mixing characteristics and timescales. This arrangement allows aero-engine combustors to achieve stable ignition, rapid traversal of the high-NO regime and efficient lean burnout [15], [22]. The general temperature and NO-CO behaviour was discussed earlier; the present section focuses on the mixing physics and reaction environments specific to each RQL stage.

2.4.1. Primary (Rich) Zone

The primary zone operates fuel-rich, typically $1.2 \lesssim \phi \lesssim 1.8$, to ensure robust ignition and to generate the radical pool required for stable combustion across the entire operating envelope. Rich conditions

promote rapid thermal cracking of kerosene components into smaller fragments and intermediates [16]. Conceptually, the breakdown follows the sequence

$$C_\nu H_\mu \rightarrow C_2H_x,\ C_1H_y \rightarrow CO,\ H_2,\ CH_i \rightarrow CO_2,\ H_2O,$$

with radicals such as H and OH forming rapidly due to short chemical timescales relative to the hydrodynamic residence time.

In this region, nitrogen chemistry is influenced by the abundance of hydrocarbon fragments. Prompt-NO (Fenimore-type) pathways become active through reactions such as $CH + N_2 \rightarrow HCN + N$, followed by oxidation of HCN to NO [15]. Although prompt NO contributes mainly in rich or moderate-temperature conditions, it is significantly weaker than the thermal mechanism that dominates near stoichiometry.

Practical primary zones are far from homogeneous. Recirculation, fuel spray atomisation and incomplete small-scale mixing produce a distribution of local equivalence ratios, which strongly influences NO formation during quenching [14]. This spatial inhomogeneity is a defining feature of RQL systems.

2.4.2. Quick-Quench Region

The quench zone rapidly mixes the rich primary products with secondary air. The goal is to minimise residence time near stoichiometric conditions, where thermal NO formation is maximal [22]. The relevant timescale is the quench mixing time,

$$\tau_q = \frac{L_m}{U_c},$$

where L_m is the distance required for the injected jets to mix with the core flow and U_c the core-stream velocity. The penetration and mixing of these jets depend on the jet-in-crossflow momentum-flux ratio,

$$J = \frac{\rho_j U_j^2}{\rho_c U_c^2},$$

which determines how rapidly the jets distribute across the combustor height.

Empirical scaling laws of the form

$$\frac{L_m}{H} \sim C\, J^n \left(\frac{d}{H}\right)^m$$

(with $n \approx 0.5$ and $m \approx 0.3$) describe how geometry and momentum govern quench effectiveness [23]. Stronger jet penetration reduces the time spent in the high-NO regime and therefore lowers the thermal NO carried into the lean zone.

Because the incoming primary stream contains a broad range of local ϕ values, subvolumes originating from richer pockets cross stoichiometric conditions more slowly and remain hotter for longer [14]. The interaction between this inhomogeneity and the finite quench mixing time is a major determinant of the final NO_x emissions in RQL systems.

2.4.3. Lean and Dilution Region

Downstream of the quench, the mixture becomes globally lean. The temperature is lower and the chemistry is dominated by the slow oxidation of CO and partially oxidised intermediates. The principal pathway,

$$CO + OH \rightarrow CO_2 + H,$$

proceeds at a rate highly sensitive to both temperature and OH concentration, making this region the controlling step for CO burnout [16], [21]. As temperature decreases, minor nitrogen pathways involving N_2O or NNH may contribute small additional amounts of NO, but thermal NO originating upstream remains dominant.

The dilution zone introduces additional air primarily to set the turbine inlet temperature and provide liner cooling. This further drop in temperature effectively freezes the chemistry; thus, NO and CO exiting this zone represent the final emissions to be compared with ICAO-certified values.

2.4.4. Interplay of Timescales and Implications

Across the RQL sequence, combustion behaviour is shaped by the competition between hydrodynamic and chemical timescales. In the rich zone, radical production proceeds rapidly (Da $\gg 1$), while in the quench zone, the mixing time τ_q competes directly with thermal-NO kinetics [22]. In the lean zone, the increase in the CO-oxidation time scale brings Da closer to unity, making CO emissions particularly sensitive to residence time and local temperature [21].

These implications complete the physical basis on which all low-order CRN representations of RQL combustors rely. The following section therefore steps back to the wider modelling hierarchy, contrasting full CFD with reduced-order CRNs before turning to specific CRN formulations used in aero-engine research.

2.5. Combustion Modelling Approaches

The modelling implications outlined above arise purely from the staged combustion physics of RQL burners. Before describing how these processes are represented in chemical-reactor networks, it is useful to situate CRNs within the broader hierarchy of combustor modelling approaches.

No single modelling approach can capture all scales efficiently, so a hierarchy of numerical strategies is used, each balancing physical detail against computational cost [13], [24]. At one extreme, Direct Numerical Simulation (DNS) provides full resolution of turbulence and chemistry. At the other, reduced-order reactor networks neglect spatial structure but retain detailed kinetics, enabling fast parametric studies. Between these limits lie the geometry-resolving Computational Fluid Dynamics (CFD) approaches that dominate design and research practice.

2.5.1. Computational Fluid Dynamics (CFD)

CFD solves the conservation equations for mass, momentum, energy, and species within the actual combustor geometry, coupling them with models of turbulence, heat transfer, and chemistry. The instantaneous equations are filtered or averaged to make computation feasible, leading to three main approaches: Direct Numerical Simulation (DNS), Large-Eddy Simulation (LES), and Reynolds-Averaged Navier-Stokes (RANS).

In DNS, all relevant scales of motion and reaction are resolved directly, making it the most physically exact representation. It has provided benchmark data for flame-turbulence interaction and ignition kernels, but its computational demand restricts it to simplified laminar or low-Reynolds-number flames [24]. LES resolves the large, energy-containing eddies and models only the sub-grid fluctuations. It captures transient behaviour, coherent structures, and unsteady flame dynamics, which are essential in lean-premixed gas-turbine combustors [25]. LES has been used successfully for sector simulations of aero-engine combustors, revealing mechanisms of oscillation, quenching, and pollutant formation that RANS cannot reproduce [26]. However, each LES case may require weeks of runtime even on high-performance clusters.

RANS, by contrast, replaces all turbulent fluctuations with statistically averaged quantities, providing steady-state fields for velocity, temperature, and species. This makes RANS the practical backbone of industrial design and certification studies [13]. Turbulence chemistry interaction is represented using models such as the eddy-dissipation concept, eddy break-up, finite-rate closures, or presumed/transported PDF methods. These approaches reproduce the global flow and temperature fields but rely on simplified reactions and mixing assumptions that limit their ability to predict slow-kinetics pathways governing NO_x and CO formation. Full-chemistry RANS or LES simulations that include thousands of reactions remain computationally infeasible for multi-point emission prediction or for parametric studies such as water-injection sweeps. Consequently, CFD cannot practically provide detailed pollutant trends across the operating envelope, motivating the use of low-order but chemically detailed alternatives.

2.5.2. Chemical Reactor Networks in the CFD Context

While CFD provides spatially resolved predictions of velocity, temperature and major-species fields, its practical use in combustor emission studies is limited by the need for turbulence-chemistry closures and the prohibitive cost of detailed kinetics. Even reduced-chemistry RANS or LES simulations typically contain only global or skeletal reaction sets, making them unsuitable for resolving the slow radical pathways that control NO and CO formation. For this reason, CFD is often combined with chemically detailed post-processing frameworks.

Chemical Reactor Networks (CRNs) occupy this reduced-order end of the modelling hierarchy. Instead of resolving geometry, the combustor is represented by a set of ideal reactors whose residence times and mixing patterns are prescribed from engineering knowledge or from CFD-derived flow information. This allows the full chemical mechanism to be applied at negligible cost compared to CFD.

In the CFD setting, CRNs therefore serve as a *complement* rather than an alternative: CFD captures the flow physics, recirculation and temperature fields, while CRNs supply detailed chemistry using these fields as boundary conditions. This division of roles explains the widespread use of CRNs in aero-engine research, as it enables parametric studies, mechanism sensitivity analysis, and pollutant prediction across operating conditions that would be infeasible to compute with full CFD.

2.6. Chemical Reactor Network Modelling in Aero-Engine Research

With the modelling hierarchy established, this section reviews the range of chemical reactor network (CRN) formulations used in aero-engine research. These models differ in how they approximate mixing, residence time and staging. Reviewing them provides the necessary context for positioning the parallel-subzone approach developed in this thesis. Two frequently used reactor types are perferctly stirred reactors (PSR) and plug flow reactors (PFR).

A PSR is a conceptual, perfectly stirred, steady-state reactor with a prescribed residence time. It has one uniform state and the outlet equals the well-mixed contents. A PFR is a one-dimensional model where the state depends on axial position x rather than time. There is no back-mixing, and the flow is steady; it can be represented in terms of temperature profiles and species along the length.

2.6.1. Serial PSR-PFR Chains

A foundational CRN topology consists of a PSR representing the primary combustion zone, followed by a PFR capturing post-flame oxidation. Shakariyants [15] applied such PSR-PFR chains to investigate NO and CO formation in lean-direct-injection configurations, demonstrating that when residence times are chosen consistently with engine conditions, the serial structure reproduces the major emission trends. Dewanji [22] adopted a similar two-reactor architecture in the analysis of LDI combustor performance, using the PSR to resolve ignition and primary reactions and the PFR to represent secondary oxidation and burnout. Merino Madrid [16] likewise used PSR-PFR sequences when developing and calibrating CRNs for different Jet-A surrogate fuels.

Serial networks are most effective when the mixture fraction evolves smoothly downstream, and when each region can be approximated as either fully mixed (PSR) or dominantly convective (PFR). Their limitations arise in contexts, such as rich-quench-lean (RQL) architectures, where strong spatial inhomogeneity in the primary zone and abrupt mixing events challenge the assumptions of homogeneity and one-dimensional progression.

2.6.2. Multi-PSR Networks

To incorporate finite-rate mixing and recirculation effects, several researchers have used networks composed of multiple PSRs in series or parallel. Shakariyants [15] investigated multi-PSR networks to improve representation of intermediate-temperature chemistry, particularly for mechanisms involving N_2O and prompt-NO precursors. Dewanji [22] used two- and three-PSR configurations to assess the impact of residence-time distribution on NO_x and CO in staged combustor concepts. Merino Madrid [16] similarly demonstrated that supplementing a primary PSR with one or more auxiliary PSRs helps model the effect of reduced mixing intensity in LDI injectors.

Although multi-PSR networks introduce flexibility, each reactor remains internally homogeneous. Consequently, they cannot capture the wide distribution of local equivalence ratios present in primary zones of practical RQL combustors, where emissions are dominated by a small fraction of near-stoichiometric pockets.

2.6.3. Sector-Based CRNs with Prescribed Air Splits

Another class of CRN models divides the combustor into physical zones based on design data, sector rig measurements or air-flow specifications. Each zone is represented by an ideal reactor with prescribed fuel and air fractions. This approach is common in engineering design studies where structural information is available and zone identification is unambiguous.

Sampat [20] constructed CRNs by importing zone boundaries and air partitions from CFD, assigning residence times according to local flow rates. Brink [21] applied a zonal CRN to evaluate how fuel composition influences NO_x and CO formation, using primary, secondary and dilution reactors to emulate the staging strategy of turbofan combustors. Sector-based networks also appear in Dewanji's PhD study [22], where air fractions and reactor volumes were derived from design geometry and pressure-drop considerations.

These models align naturally with staged architectures and are useful when air splits are known. However, their assumption of perfect mixing within each zone precludes representation of the sub-scale mixture inhomogeneity that strongly affects thermal NO formation. Reactors operating at zone-averaged ϕ values cannot resolve the near-stoichiometric micro-regions where NO production is maximal.

2.6.4. Modelling Unmixedness in CRN

To represent incomplete mixing explicitly, Bisson et al. [14] introduced CRNs based on probability-density functions for mixture fraction or equivalence ratio. The primary-zone ϕ distribution is discretised into a set of parallel PSRs, each with a distinct local equivalence ratio, ϕ_i, and quadrature weight. The reactor outlets are then mixed adiabatically before feeding the lean oxidation region.

This formulation captures the physical dependence of thermal NO on the rich-stoichiometric tail of the distribution. Bisson et al. showed that predictions of CO and NO_x converge only when the number of subzones exceeds one hundred, indicating that fine resolution of ϕ is required to represent the full range of local conditions. PDF-based models therefore bridge the gap between homogeneous CRNs and geometry-resolving CFD. Their drawbacks are increased computational cost and the need for careful treatment of pressure consistency and residence-time specification across many parallel reactors.

2.6.5. Relation of This Thesis to Existing CRN Approaches

The CRN developed in this thesis builds upon the unmixedness philosophy of PDF-based networks and adapts it to the specific structure of RQL combustors. Its primary-zone model consists of a set of parallel subzones, each assigned a local equivalence ratio ϕ_i drawn from a mean-preserving distribution parameterised by the mixing variable, s. This construction captures the inhomogeneity of mixture fraction seen experimentally and described in detailed modelling studies [14], [15].

A second refinement is the definition of reactor volumes such that all primary subzones share the same hydrodynamic residence time. Instead of imposing geometric volumes, each subzone volume is computed from its mass flow rate and a common target residence time, ensuring that chemical time is treated consistently. This avoids artefacts seen in earlier sector-based networks, where volume slicing could bias the influence of rich or lean regions [20], [22].

Downstream, the quench region, lean burn and dilution zones are represented by a combination of PFR and PSR elements, with all mixing steps performed adiabatically at a fixed reference pressure. This ensures thermodynamic consistency and preserves the correct sensitivity of CO burnout and NO formation to temperature and radical availability.

Relative to earlier CRN approaches, the present model offers several benefits:

- **Direct sensitivity to mixing quality.** The parameter s governs the width of the ϕ distribution, allowing unmixedness to be mapped directly to emission behaviour in a mechanistic manner consistent with PDF-derived insights [14].
- **Accurate representation of nitrogen chemistry.** Each subzone solves detailed kinetics, capturing the varying balance among thermal, prompt, N_2O and NNH pathways across the ϕ spectrum [15].
- **Improved prediction of CO burnout.** Downstream PFR segments represent the slow OH-driven conversion of CO to CO_2, aligning with recommendations in prior CRN analyses [21], [22].
- **Computational efficiency.** Because the primary subzones are independent reactor networks, they can be solved in parallel without numerical coupling issues, enabling rapid evaluation across operating conditions.

In summary, the present CRN combines the physical expressiveness of unmixedness-based models with the efficiency and stability required for multi-condition aero-engine emission prediction. Its structure

is well suited to capturing the NO-CO trade, the temperature sensitivity of water injection and the staging behaviour characteristic of RQL architectures.

2.7. ICAO engine emission standards and measurement methods

The International Civil Aviation Organization (ICAO) defines global standards for aircraft engine emissions under Annex 16, Volume II of the Convention on International Civil Aviation [27]. These standards specify measurement procedures and certification limits for gaseous species including carbon monoxide (CO), unburned hydrocarbons (HC), and oxides of nitrogen (NO_x), as well as for smoke and non-volatile particulate matter (nvPM). They apply to all subsonic turbojet and turbofan engines with rated thrust greater than 26.7 kN and have been progressively tightened through successive CAEP amendments [28].

2.7.1. The reference LTO cycle

Certification measurements are performed over a prescribed landing and take-off (LTO) cycle, representing operation below 915 m (3000 ft). The LTO cycle consists of four thrust modes: take-off (100%), climb-out (85%), approach (30%), and idle (7%), each with fixed times-in-mode of 0.7, 2.2, 4.0, and 26.0 minutes respectively. All measurements are corrected to International Standard Atmosphere (ISA) sea-level static conditions with a reference absolute humidity of 0.00634 kg H_2O per kilogram of dry air. The reported pollutant mass D_p is divided by rated thrust F_{00} to obtain the certification parameter D_p/F_{00} in g kN^{-1}, or expressed as an emission index

$$\mathrm{EI}_i = \frac{\dot{m}_i}{\dot{m}_f},$$

where $\dot{m}_i$ is the mass flow of species i and $\dot{m}_f$ is the fuel flow, yielding units of g kg^{-1} fuel.

2.7.2. Measurement conventions of NO_x

For NO_x, Annex 16 defines the measured quantity as the sum of nitric oxide (NO) and nitrogen dioxide (NO_2), calculated as if all nitrogen oxides were in the form of NO_2 [27, App. 3 § 3.3]. This means that both NO and NO_2 are weighted by the molar mass of NO_2 (46 g mol^{-1}) when computing emission indices, rather than by their respective true molecular masses. The chemically correct emission index would be computed as

$$\mathrm{EI}_{\mathrm{NO_x,true}} = \frac{M_{\mathrm{NO}}}{M_{\mathrm{N}}}\,\mathrm{EI}_{\mathrm{NO}} + \frac{M_{\mathrm{NO_2}}}{M_{\mathrm{N_2}}}\,\mathrm{EI}_{\mathrm{NO_2}},$$

where each term is weighted by its actual molecular mass. In contrast, the ICAO convention defines

$$\mathrm{EI}_{\mathrm{NO_x,ICAO}} = \frac{M_{\mathrm{NO_2}}}{M_{\mathrm{N}}}\left(\mathrm{EI}_{\mathrm{NO}} + \mathrm{EI}_{\mathrm{NO_2}}\right),$$

so that all nitrogen oxides are expressed on an NO_2 mass basis. The relative bias introduced by this convention is illustrated by the fractional form

$$\frac{\mathrm{EI}_{\mathrm{NO_x,ICAO}}}{\mathrm{EI}_{\mathrm{NO_x,true}}} = \frac{46}{30}\,\frac{x_{\mathrm{NO}} + x_{\mathrm{NO_2}}}{x_{\mathrm{NO}} + 1.53\,x_{\mathrm{NO_2}}},$$

where x_{NO} and $x_{\mathrm{NO_2}}$ are the molar fractions of each component. For typical engine exhaust, where about 80 percent of NO_x appears as NO, this ratio is approximately 1.47, confirming that ICAO-reported NO_x values are roughly 50 percent higher than the true chemical mass.

The rationale for using NO_2 weighting is threefold. First, it ensures measurement alignment: chemiluminescent NO_x analyzers oxidize NO to NO_2 before detection, and their calibration is inherently expressed in NO_2 mass units [29]. Second, it reflects atmospheric relevance: after exhaust release, NO rapidly oxidizes to NO_2, which is the species of primary concern for local air quality and ozone formation [30]. Third, it maintains global reporting uniformity: adopting a single molar-mass basis prevents engine-to-engine bias when emission indices are reported in grams per kilogram of fuel, thereby ensuring that all certification and databank values remain directly comparable [28]. The use of the 46 g mol^{-1} basis is therefore intentional and embedded in all ICAO and FAA reporting procedures.

2.7.3. Measurement of other species

Hydrocarbon emissions are determined using a heated flame-ionization detector (FID) at 160 ± 15 °C, calibrated with propane and reported as methane equivalent. This method does not integrate all organic species but selectively responds to lighter, saturated hydrocarbons while under-responding to oxygenated or aromatic compounds [30], [31]. Partial condensation and losses of semi-volatile species in the sampling system further bias the measured value. Consequently, the “ICAO HC” metric represents an instrument-specific signal rather than the true total unburned hydrocarbon mass.

2.7.4. Procedures, precision limits, and databank consistency

ICAO Annex 16, Volume II defines the procedures by which gaseous emissions are measured, corrected, and reported for certification purposes. These procedures apply to the four reference LTO modes and are expressed through a sequence of instrument requirements, calibration-gas tolerances, and data-handling rules that together determine the intrinsic precision of CO and NO_x emission indices [27]. A concise summary of the definitions and tolerances relevant for this work is provided in Table 2.1.

Annex 16 defines the emission index EI_i as the mass of pollutant per unit mass of fuel, corrected to reference atmospheric conditions and, if necessary, to a reference standard engine. The total pollutant mass emitted over the LTO cycle, D_p, is obtained by integrating the corrected emission index with the fuel mass flow and the prescribed LTO times-in-mode. The certification quantity D_p/F_{00} expresses the cycle-integrated pollutant mass per unit rated thrust and forms the basis for comparison with regulatory limits. These procedures are defined in Part III, Chapter 2 and Appendix 3 of Annex 16 and provide the reference point for all values published in the ICAO Engine Emissions Databank.

A key reporting feature is that NO and NO_2 are aggregated as NO_x on an NO_2 mass basis. This convention is mandated explicitly in Annex 16, Appendix 5, Attachment E and repeated in the EASA databank introduction. It matches the operation of chemiluminescent analyzers, which detect NO_2 after quantitative oxidation of NO in the sample stream, and ensures uniformity across engines and certification tests. While this introduces a systematic offset relative to the chemically correct mass of NO + NO_2, it is a deliberate and well established convention and is followed in this work to ensure consistency with ICAO data.

Annex 16 also specifies detailed performance requirements for the analyzers used for CO, CO_2, HC and NO_x. Zero and span drift, linearity and repeatability must remain within approximately $\pm 2\,\%$ of full scale for the duration of a test, and calibration gases must meet certified tolerances of $\pm 2\,\%$ of nominal concentration or a small absolute concentration, depending on species. These limits are stated in Appendix 5 (Attachments A-D) and directly bound the accuracy of concentration measurements at typical LTO levels. In addition, Appendix 3, Attachment F requires the measurement of fuel mass flow to be accurate within $\pm 2\,\%$ when used to derive emission indices or D_p/F_{00}. Taken together, these tolerances imply that the combined uncertainty of CO and NO_x emission indices under normal LTO conditions lies at the level of a few per cent. Variations between model predictions and certification data smaller than these margins cannot be interpreted as physically meaningful differences.

The EASA introduction to the ICAO Engine Emissions Databank further notes that small inconsistencies of order $2\,\%$ may appear between tabulated values such as D_p/F_{00} and the corresponding quantities recomputed from reported fuel flows, times in mode and emission indices. These arise from rounding, intermediate-field truncation and differences in data handling rather than from measurement error. For this reason, discrepancies at or below this level fall within the intrinsic precision of the databank and should not be viewed as reflecting true differences in engine behaviour. Throughout this work, all comparisons with ICAO-certified CO and NO_x emission indices respect these precision limits.

2.7.5. Implications for modeling

Because chemical reactor network (CRN) or computational fluid dynamics (CFD) models compute complete species concentrations, they cannot replicate the selective response of a FID or the sampling losses inherent to the measurement system. Any apparent agreement between simulated and ICAO “HC” data would therefore be coincidental or the result of redefining the modeled quantity to mimic the instrument’s response function [32], [33]. For this reason, physically meaningful model validation focuses on CO and NO_x, which are directly measurable and chemically well defined.

Table 2.1: Summary of ICAO Annex 16, Volume II definitions and tolerances relevant for CO and NO_x emission indices.

Quantity	Definition and tolerances
Emission index EI_i	Mass of pollutant per mass of fuel ($g\,kg^{-1}$), corrected to reference conditions and LTO mode following Annex 16 EI procedures.[a]
Cycle mass and D_p/F_{00}	LTO-integrated pollutant mass D_p divided by rated thrust F_{00}, using prescribed thrust modes and times.[b]
NO_x definition	NO + NO_2 expressed entirely as NO_2 mass for reporting and comparison; consistent with chemiluminescent analyzer operation.[c]
Analyzer accuracy	NDIR (CO, CO_2) and FID (HC) analyzers must meet drift, linearity and repeatability limits typically within ± 2 % of full scale; calibration gases within ± 2 % or $\pm$ 2 ppm.[d]
NO_x analyzer and converter	Chemiluminescent NO_x analyzers and converters subject to equivalent ± 2 % performance limits and certified calibration-gas tolerances.[e]
Flow and fuel-flow accuracy	Fuel-flow measurement used for EI calculation must be accurate within ± 2 %.[f]Combined analyzer and flow tolerances imply overall EI precision of a few percent.
Databank internal consistency	EASA notes that published D_p/F_{00} values may differ by ~ 2 % from values recomputed from EI, fuel flow and times due to rounding and data handling.[g]

[a] Annex 16 Vol. II, App. 3 §7.2 and App. 5 Att. E define EI computation and corrections.
[b] Annex 16 Vol. II, Part III Ch. 2 §2.1.4-2.1.4.3 and §2.4.–2.4.3.
[c] Annex 16 Vol. II, App. 5 Att. E; EASA EDB Introduction §4.
[d] Annex 16 Vol. II, App. 5 Att. A-D.
[e] Annex 16 Vol. II, App. 5 Att. C.
[f] Annex 16 Vol. II, App. 3 Att. F.
[g] EASA EDB Introduction §3 and §6.2.

2.7.6. Limitations of the ICAO databank

The ICAO Engine Emissions Databank compiles certified data for engines in production, measured under static, sea-level conditions. The database is valuable for comparison and regulatory compliance but has intrinsic limitations. It reflects emissions only below 915 m and does not represent cruise conditions. The reported fuel flows exclude bleed and power off-takes, and small inconsistencies may exist between datasets because of rounding and differing measurement times for gaseous and nvPM species [28]. Therefore, the databank provides a consistent baseline for LTO-cycle emission comparison but cannot by itself describe in-flight emission behavior or the detailed chemistry of hydrocarbon oxidation.

2.7.7. Relevance to this work

In predictive modeling of RQL combustors, emission indices for CO and NO_x are compared against the ICAO-certified values, adopting the NO_2-equivalent convention for NO_x to ensure consistency. Hydrocarbon measurements, by contrast, are not modeled because their instrument-specific bias prevents meaningful physical comparison. This approach follows standard practice in aero-engine emission modeling, where CO and NO_x constitute the two robust and reproducible targets for validation.

2.8. Parallel Subzones and Unmixedness Representation

The preceding sections introduced the CRN modelling framework and its relation to both RQL physics and earlier formulations. This section now describes the specific parallel-subzone architecture developed in this thesis, building on the unmixedness-based concepts reviewed in Section 2.6 but providing the detailed implementation used in the simulations.

Primary-zone mixing in practical aero-engine combustors is incomplete, so the local equivalence

ratio ϕ is distributed around a mean value $\bar{\phi}$. The spread of this distribution determines the fraction of mixtures near stoichiometry encountered during quench, where thermal NO formation rates are highest. Reactor-network models emulate this physics using parallel subzones that burn independently at different local ϕ_i and mix downstream.

2.8.1. Statistical description of unmixedness

Imperfect mixing is represented by an unmixedness parameter, s, that controls the width of the equivalence-ratio distribution $f_\Phi(\phi;\bar{\phi},S)$. The distribution is normalized and mean-preserving:

$$\int f_\Phi(\phi;\bar{\phi},S)\,d\phi = 1, \qquad \int \phi\, f_\Phi(\phi;\bar{\phi},S)\,d\phi = \bar{\phi},$$

and its variance $\sigma_\phi^2(S)$ increases with s. A broader distribution yields a larger fraction of $\phi \approx 1$ pockets and therefore higher NO formation during quench. Physically, s maps the degree of mixture inhomogeneity caused by fuel-air spray structure, recirculation, and jet-in-crossflow penetration [23], [34].

A widely used formulation, adopted in the CRN of Bisson et al. [14] and in several aero-engine studies, is a normal distribution:

$$f(\phi) = \frac{1}{\sqrt{2\pi\sigma^2}} \exp\left[-\frac{(\phi-\phi_{\mathrm{PZ}})^2}{2\sigma^2}\right],$$

with the standard deviation defined through the mixing parameter

$$\sigma = s\,\phi_{\mathrm{PZ}}.$$

This provides a direct physical interpretation: $s = 0$ is perfectly mixed, and larger s corresponds to broader inhomogeneity.

Figure 2.1 illustrates how the mixing parameter s broadens the equivalence-ratio distribution at fixed $\bar{\phi}$, and how this continuous $f_\Phi(\phi;\bar{\phi},S)$ is discretised into parallel subzones used in the reactor network.

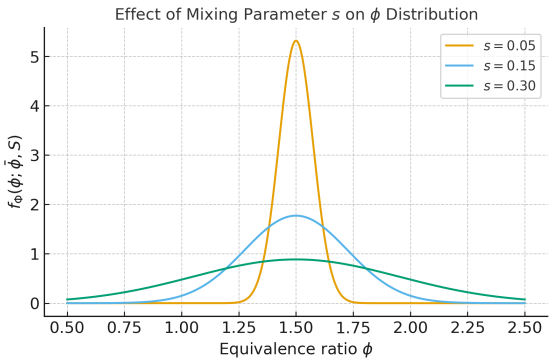

(a) Continuous probability density $f_\Phi(\phi;\bar{\phi},S)$ for three values of the unmixedness parameter s at fixed mean equivalence ratio $\bar{\phi}_{\mathrm{PZ}}$. Larger s broadens the distribution and increases the probability of near-stoichiometric pockets.

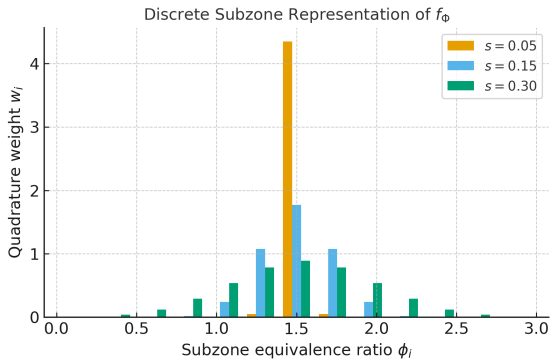

(b) Discrete primary-zone subzones obtained by quadrature of $f_\Phi(\phi;\bar{\phi},S)$ into N parallel reactors with local ϕ_i and weights w_i. Each bar represents one subzone, solved as an independent PSR with identical hydrodynamic residence time.

Figure 2.1: Effect of the unmixedness parameter s on the primary-zone equivalence-ratio distribution and its discretisation. (a) Continuous probability density $f_\Phi(\phi;\bar{\phi},S)$. (b) Corresponding discrete subzones used in the parallel-reactor network, approximating $\langle g(\phi)\rangle = \int g(\phi) f_\Phi(\phi;\bar{\phi},S)\,\mathrm{d}\phi$ by $\sum_i w_i g(\phi_i)$.

2.8.2. Parallel-subzone construction

Let the primary zone be partitioned into N subzones. Each subzone i is assigned a local equivalence ratio ϕ_i obtained by discretizing $f(\phi)$ over the range

$$[\phi_{\mathrm{PZ}} - 3\sigma\,,\ \phi_{\mathrm{PZ}} + 3\sigma],$$

which covers 99.7% of the normal distribution. In the method of Bisson et al., the mixture fraction allocated to each PSR is proportional to the area of $f(\phi)$ over that interval [14]. Each subzone is

solved as a well-stirred ideal-gas reactor with identical hydrodynamic residence time τ_{PZ}. The outlet streams are then mixed adiabatically at a fixed pressure to feed the downstream secondary and dilution zones. A numerical quadrature of the form

$$\langle g(\phi)\rangle \approx \sum_{i=1}^{N} w_i\, g(\phi_i), \qquad \sum_i w_i = 1,$$

ensures that global properties are consistent with the imposed $\bar{\phi}$ and s.

2.8.3. Convergence behaviour and literature evidence

Predicted emissions depend on how finely the ϕ-distribution is resolved across the N subzones. This behaviour was quantified explicitly by Bisson et al. [14], who performed a systematic convergence study for CO and NO_x at all four ICAO LTO power settings. For each value of N, the full CRN was re-solved and the relative error

$$\Delta EI_X(N) = \frac{|EI_X(N) - EI_X(\infty)|}{EI_X(N)}, \qquad X \in \{CO, NO_x\},$$

was evaluated. Tolerances of $\pm 15\%$ for CO and $\pm 5\%$ for NO_x were adopted (following Allaire's CRN calibration work [35]). Figure 2.2 (taken from [14]) shows the resulting convergence behaviour.

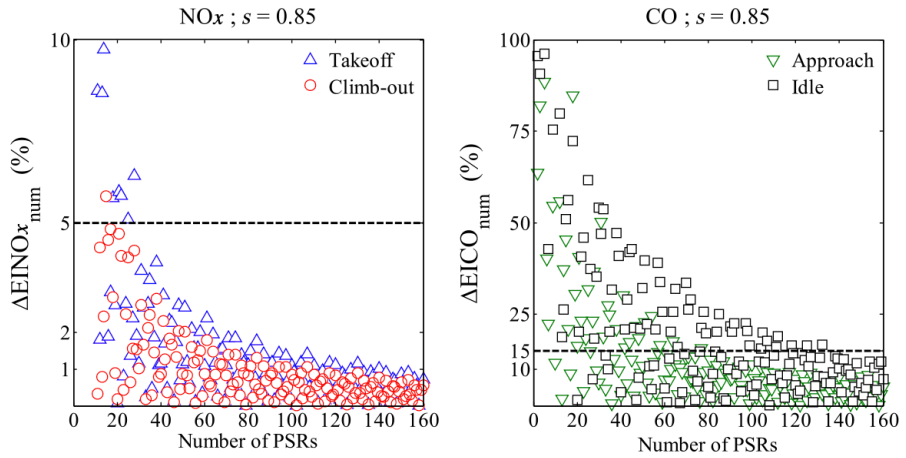

Figure 2.2: Relative error of computed CO and NO_x emission indices as a function of the number of parallel primary-zone PSRs, courtesy of Bisson et al. [14]. The dashed lines indicate the $\pm 15\%$ (CO) and $\pm 5\%$ (NO_x) tolerances. Convergence is reached only beyond approximately $N \approx 100$ subzones. The authors selected $N = 135$ PSRs to satisfy both tolerances for all four ICAO LTO configurations.

The study demonstrated three key points:

1. Predictions of CO and NO_x change significantly for low N, especially between $N = 5$ and $N = 50$.
2. NO_x is more sensitive than CO, because it is dominated by the near-stoichiometric tail of $f(\phi)$.
3. Convergence is not achieved until $N > 100$; the authors therefore selected $N = 135$ PSRs for all power settings.

These results emphasise that resolving the rich-stoichiometric tail of the ϕ-distribution requires a large number of parallel reactors. Using too few subzones artificially narrows the distribution and suppresses the high-temperature pockets that drive thermal NO formation.

Choice of operating points for convergence testing

Bisson et al. performed convergence checks at all ICAO LTO conditions, but the most sensitive cases were retained for Figure 2: *CO at approach/idle* (lean burnout limited) and *NO_x at takeoff/climb* (thermal-NO limited). This aligns with the general recommendation in RQL modelling:

test CO at lean, low-T points; test NO_x at high-T points.

These extremal power conditions stress opposite ends of the NO-CO trade-off and therefore provide a robust convergence criterion.

2.8.4. Relation between s and flow physics

Bisson et al. treat s as a calibration parameter tuned using measured EI_{CO} and $EI_{\mathrm{NO_x}}$, weighted by power level (Eq. (4) in their paper). Physically, s reflects the level of mixture inhomogeneity generated by spray breakup, local recirculation, and secondary-air jet mixing. Experimental work by Pompei and Heywood [36] and later military-engine studies [37] show the same trend: poorer mixing (lower Reynolds number or weaker jet penetration) increases the spread of ϕ.

Implications for emissions

For fixed $\bar{\phi}$, increasing s broadens $f(\phi)$, raises the probability of near-stoichiometric regions, and increases thermal-NO formation. The effect on CO is non-monotonic. Stronger unmixedness produces rich pockets that improve CO burnout downstream, but excessive broadening can also generate overly lean, cool regions that limit oxidation. Parallel subzones therefore offer a compact and mechanistically transparent way to represent imperfect mixing and to assess how water injection modifies the temperature-dependent NO-CO balance in each subzone.

3

Methodology

This chapter presents the methodology used to construct and solve a chemical reactor network (CRN) for the CF6 combustor using the Cantera library in Python. This combustor, specifically the CF6-80C2B1F, makes for a good baseline model because of known input parameters. Every reacting element is represented by an `IdealGasReactor`, supported by reservoirs and flow controllers. The architecture follows the physical rich-quench-lean (RQL) structure while respecting Cantera's constraints on interconnecting `ReactorNet` objects. All equations, zone definitions and mass flows map directly onto the implementation in the `CF6Engine` class. The structure of this chapter mirrors the execution sequence of the code to provide an explicit one-to-one correspondence between the numerical model and the theoretical description. Details on all parts of this methodology can be found on the Cantera website [38].

3.1. Input Data and Boundary Conditions

3.1.1. Data sources

The model requires four sets of boundary inputs for each LTO power setting: P_{03}, T_{03}, fuel mass flow and total core-air mass flow. These come from two external sources:

- **ICAO Engine Emissions Databank** provides only the fuel mass flow and the certified emission indices for NO_x, CO and HC.
- **Telidevara** [8] provides:
  - core-air mass flow $\dot{m}_{\text{air}}$,
  - compressor-exit total pressure P_{t3},
  - compressor-exit total temperature T_{t3},
  - combustor-zone volumes.

  These were obtained by running the *Gas Turbine Simulation Program* (GSP) for the CF6 and subsequently using *Aerocomb* to compute the geometric distribution of combustor volumes.

Thus, the ICAO database provides the fuel-bound inputs, whereas all flow and thermodynamic conditions are supplied by Telidevara's study.

The values implemented in `set_conditions()` are presented in Table 3.1. Pressures appear as bars in the Python code and are converted to Pascals internally.

Table 3.1: CF6 combustor inlet conditions used in the model.

Quantity	Takeoff	Climbout	Approach	Idle
P_{03} [Bar]	30.48	26.42	12.14	5.88
T_{03} [K]	796.56	768.54	626.44	508.71
$\dot{m}_{\text{fuel}}$ [kg/s]	2.29	1.91	0.69	0.24
$\dot{m}_{\text{air}}$ [kg/s]	124.10	109.97	58.06	33.00

Telidevara [8] computed the CF6 combustor-zone volumes using Aerocomb. The total volume consists of 0.06875 m^3, volumes of individual zones are shown in Figure 3.1.

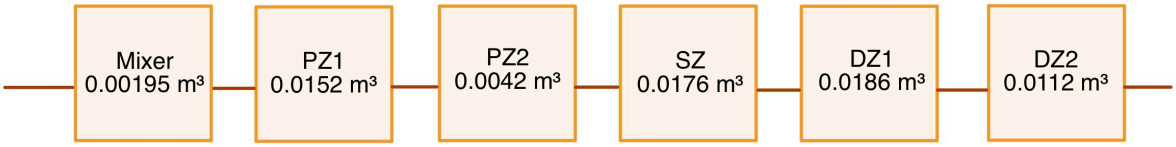

Figure 3.1: Schematic of the individual volumes used by Telidevara [8].

The mixer in this thesis model is not treated as a physical reactor. Its mixing operation is algebraic and instantaneous, so to conserve the total geometric volume, the Aerocomb mixer volume is reassigned to PZ1:

$$V_{\text{PZ1,model}} = V_{\text{PZ1}} + V_{\text{mix}}.$$

This adjustment is justified because PZ1 is a physical region, while the mixer is just a mathematical definition in this implementation.

For each power setting, `set_conditions()` includes a default set of equivalence ratios,

$$[\phi_{\text{PZ1}}, \phi_{\text{PZ2}}, \phi_{\text{SZ}}],$$

and a default primary unmixedness parameter s.

The constructor allows overrides of $\phi_{\text{PZ1}}, \phi_{\text{PZ2}}, \phi_{\text{SZ}}, s$, the number of primary subzones N and the valve coefficients. Override capability is provided early because these parameters are varied later for:

- optimisation of ϕ and s,
- subzone-convergence testing,
- tuning of valve coefficients to achieve realistic pressure profiles.

3.2. Fuel Surrogate and Stoichiometry

The Dagaut mechanism is used to represent a three-component Jet-A surrogate:

$$\text{NC10H22} : 0.74, \quad \text{PHC3H7} : 0.15, \quad \text{CYC9H18} : 0.11.$$

A helper routine, `_f_st_for_mix`, evaluates the stoichiometric fuel-air mass ratio f_{st} by parsing the molecular composition and air reference mixture.

3.3. Reactor Network Structure

See Figure 3.2 for a schematic of the entire CRN setup. Each section will be explained in detail. The combustor is represented by:

- N parallel `IdealGasReactor`s for PZ1,
- one reactor for PZ2,
- one reactor for the secondary zone,
- two reactors for dilution.

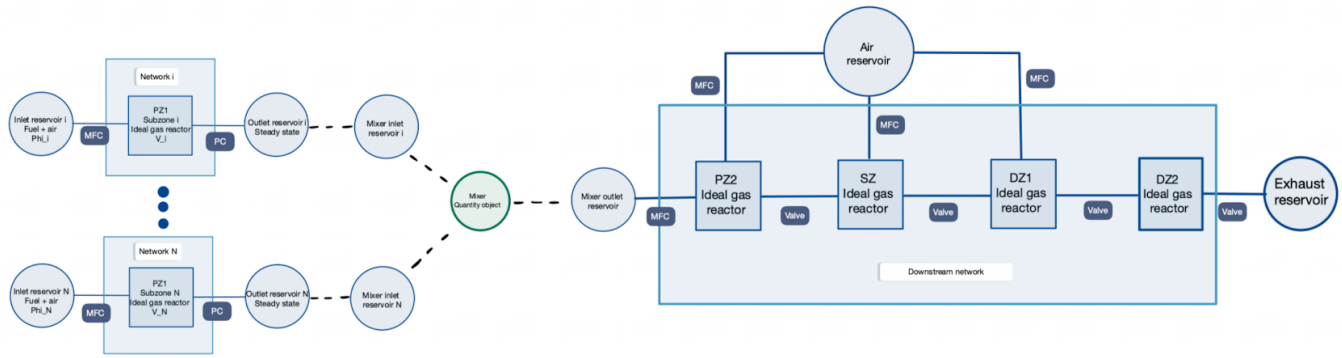

Figure 3.2: Schematic overview of the entire CRN.

The code executes:

1. `set_conditions()`
2. `build_primary_zones()`
3. `add_primary_flows()`
4. `run_primary_net()`
5. `build_mixer_zones()`
6. `mix_streams()`
7. `build_downstream_zones()`
8. `add_downstream_flows()`
9. `run_downstream_net()`

Choice of reactor model

All zones are implemented using Cantera's `IdealGasReactor`. This reactor type solves the homogeneous, zero-dimensional conservation equations for mass, species and energy at fixed volume. It represents a perfectly stirred control volume in which temperature and composition are uniform at every instant.

This choice differs from the plug-flow or perfectly stirred reactor models used in several earlier RQL studies. A PFR introduces axial resolution and requires marching the solution along a spatial coordinate, while a PSR assumes complete and permanent mixing at fixed residence time. In contrast, the `IdealGasReactor` provides the physically correct behaviour for the CRN approach used here: each zone is treated as a well-mixed finite-volume reactor that relaxes to its steady state through the full finite-rate chemistry of the Dagaut mechanism. No artificial mixing or residence-time formulation is needed, since both follow naturally from the reactor volume and the imposed mass flows.

3.4. Primary-Zone Unmixedness Representation

Each PZ1 subzone operates in its own independent `ReactorNet`. This approach is:

- *physically justified*: subzones are independent flow paths with no inter-zone mixing, heat transfer or diffusion,
- *computationally efficient*: it removes unnecessary stiffness and drastically reduces solve times,
- *modular*: it allows future parallelisation across cores.

Each PZ1 subzone is supplied with its own unique fuel-air mixture coming from its own reservoir. That means that when N parallel subzone reactors are created, there are also N reservoirs containing the premixed inlet: see Figure 3.3.

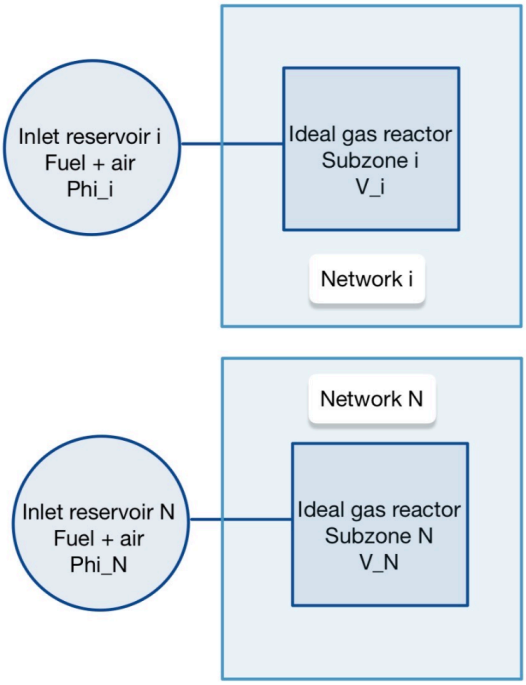

Figure 3.3: Schematic overview of the inlets.

The truncated normal distribution produced by `phi_PZ1` yields

$$\{\phi_{1,i}\}_{i=1}^{N}, \qquad \{w_i\}_{i=1}^{N}$$

with standard deviation $\sigma = s\phi_{\text{PZ1}}$. The upper bound is

$$\phi_{\text{max}} = \phi_{\text{PZ1}} + \texttt{trunc\_factor} \cdot \sigma.$$

Subzones below a minimum lean threshold are clipped to avoid representing blowout-prone mixtures. Because clipping shifts the discrete mean, a function `_invert_truncated_mean` adjusts the underlying normal mean so that:

$$\sum_{i=1}^{N} w_i \phi_{1,i} = \phi_{\text{PZ1}}.$$

This ensures the implemented mean richness exactly matches the imposed one.
Equal hydrodynamic residence time is imposed via:

$$V_i = \dot{m}_i \, \tau_{\text{PZ1}},$$

with the constraint:

$$\sum_{i=1}^{N} V_i = V_{\text{PZ1,model}}.$$

Meaning that each subzone gets assigned a different share of the total volume, based on its residence time. This ensures consistent subzone residence times while preserving the total PZ1 volume (including the mixer addition).

3.5. Primary-Zone Operation

3.5.1. Mass-flow allocation

Each subzone receives:

$$\dot{m}_{\text{fuel},i} = w_i \dot{m}_{\text{fuel}}, \qquad \dot{m}_{\text{air},i} = \frac{\dot{m}_{\text{fuel},i}}{\phi_{1,i} f_{\text{st}}}.$$

The flows are delivered through `MassFlowControllers`.

Mass-flow controllers are used for all fuel and air inlets because the inlet mass flows are known and must be enforced exactly. A pressure-driven device would be physically inappropriate at this location: the upstream "reservoirs" represent pure-species boundary conditions, not real plenums with a defined total pressure. Using a valve would make the inlet mass flow depend on the reactor pressure, which would destroy the intended subzone equivalence ratios and introduce an unphysical feedback between combustion temperature and inlet flow rate. By contrast, a mass-flow controller enforces the prescribed inflow independent of reactor pressure and therefore preserves the desired ϕ-distribution and unmixedness structure in PZ1.

3.5.2. Steady-state integration

Each subzone is solved to steady state in its own `ReactorNet` using:

$$\texttt{atol} = 10^{-15}, \qquad \texttt{rtol} = 10^{-9}.$$

These tolerances ensure accurate radical and intermediate chemistry resolution.

Steady-state solution of the PZ1 subzones

Each PZ1 subzone is solved to steady state in its own `ReactorNet`. The integration proceeds through repeated calls to `advance_to_steady_state()`, which advances the reactor until all state derivatives fall below the specified absolute and relative tolerances. This method follows the full finite-rate chemistry of the Dagaut mechanism and converges to the physically meaningful steady state dictated by the imposed mass flows, reactor volume and mixture composition.

An important property of this procedure is that *the final steady state is independent of the initial reactor conditions*. Even though each subzone is initialised with a mixture at (P_{03}, T_{03}), its composition and temperature are overwritten entirely by the sustained inflow from the premixed fuel-air reservoir. Once the inflow establishes the true equivalence ratio $\phi_{1,i}$, the solver relaxes the reactor to the unique steady state implied by that mixture. All initialisation biases in species or temperature are eliminated automatically during the integration.

Because each subzone runs in its own `ReactorNet`, the stiff ODE system for each reactor is solved independently of the others. This removes artificial numerical coupling and significantly reduces stiffness. The chosen tolerances are sufficiently strict to resolve the fast radical pathways governing ignition, NO production and CO burnout without introducing numerical artefacts. At convergence, each PZ1 reactor provides a consistent temperature, composition and enthalpy for subsequent mixing.

3.6. Mixer Construction

3.6.1. Constraints imposed by Cantera

Because flow devices cannot connect reactors across different `ReactorNets`, each subzone requires:

- an outlet reservoir (see, Figure 3.4),

- a corresponding inlet reservoir feeding the mixer.

Subzone outlet states must be copied explicitly into these inlet reservoirs to avoid stale compositions.

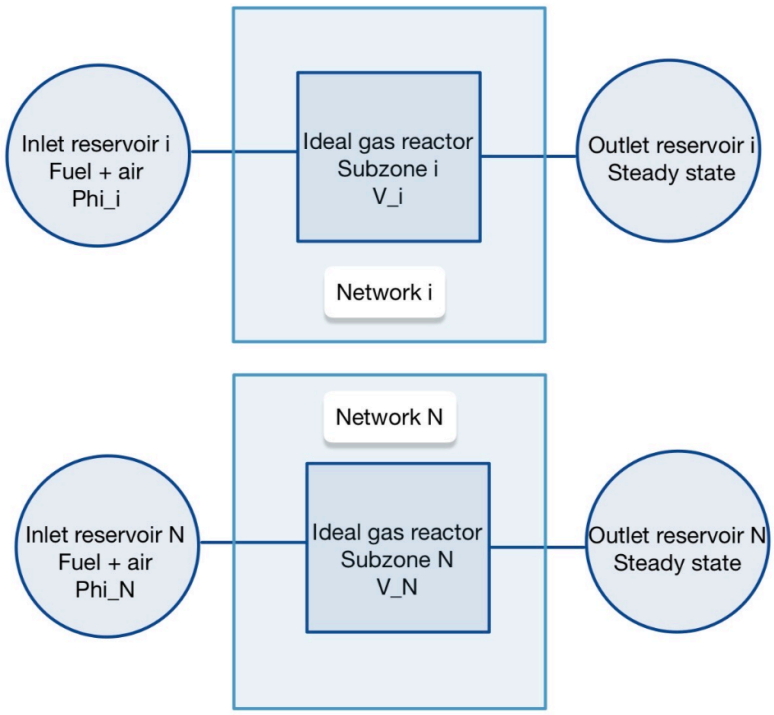

Figure 3.4: Schematic overview of the parallel subzones.

3.6.2. Scientific considerations for mixing

The mixer was designed by considering:

- *IdealGasReactor*-based mixing caused pressure spikes because of the very small mixer volume needed to mimic a spatially compact region.
- A CSTR-based mixer preserved pressure but did not guarantee that inflow overwrote the initial state, allowing initialisation bias in temperature or ϕ to persist.
- Physically, mixing is nearly instantaneous and should not introduce spurious dynamics.

3.6.3. Adopted solution: algebraic mixing via `Quantity`

A Cantera `Quantity` object provides:

- algebraic species and enthalpy averaging,
- no initialisation bias,
- no dynamics,
- guaranteed mass and energy conservation at constant pressure.

The PZ1 exhaust stream is therefore formed through a `Quantity`-based mix, producing a physically consistent inlet to PZ2. The mixer receives only the exhaust gases from the PZ1 subzones; all fresh air required to reach the target ϕ_{PZ2} is added directly to the PZ2 reactor via a separate mass-flow controller. In this way, the mixer represents purely the burned rich primary stream, while the subsequent dilution to the PZ2 equivalence ratio is handled inside the PZ2 reactor itself. See Figure 3.5 for a schematic of the full chain until this point.

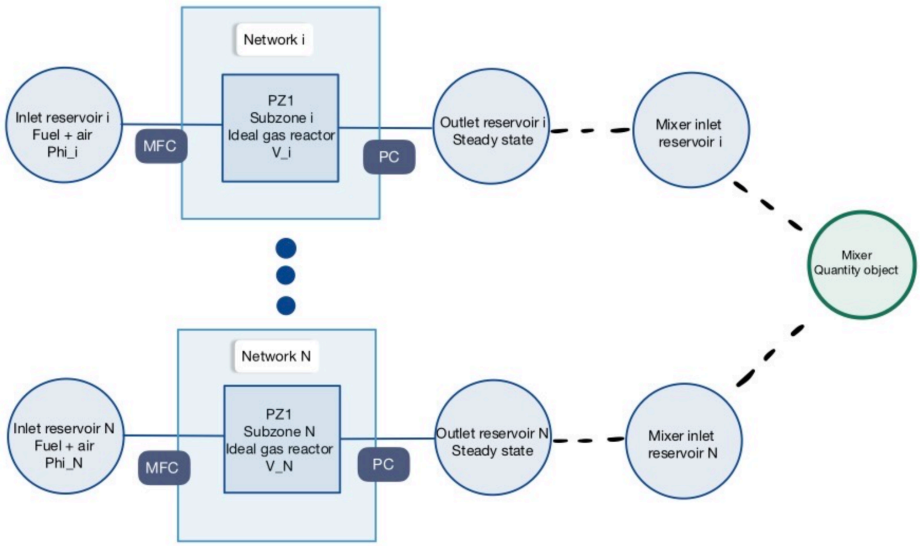

Figure 3.5: Schematic overview of the chain up to the mixer.

3.7. Downstream Zones

PZ2, SZ, DZ1 and DZ2 are instantiated using:

- the inlet state (P_{03}, T_{03}),
- their Aerocomb volumes from Telidevara [8],
- mixtures defined by their target equivalence ratios.

All downstream reactors are initialised at the compressor-exit pressure and temperature because this reflects the physical state of the mixture before any heat release or mixing takes place. The PZ1 exhaust is mixed algebraically at constant pressure and then supplied to PZ2, but the downstream reactors themselves must begin from a neutral, unmixed state. Initialising them at (P_{03}, T_{03}) provides a numerically stable and physically consistent starting point from which the imposed inflows and chemistry drive the solution towards the correct steady state.

Air allocation is computed directly from the equivalence ratios. For example:

$$\dot{m}_{\text{air,PZ2}} = \frac{\dot{m}_{\text{fuel}}}{\phi_{\text{PZ2}} f_{\text{st}}} - \dot{m}_{\text{air,PZ1}}.$$

Similar expressions determine the SZ and DZ1 air flows. A single air reservoir feeds PZ2, SZ and DZ1, each through their own mass flow controller.

The downstream sequence:

$$\text{PZ2} \rightarrow \text{SZ} \rightarrow \text{DZ1} \rightarrow \text{DZ2}$$

is connected through valves with calibrated discharge coefficients.

Valves are used between zones because they offer a simple and numerically stable way to connect successive `IdealGasReactor` objects. A valve imposes a pressure-driven mass-flow relationship, but in this model the valve coefficients are tuned such that the pressure remains effectively uniform across PZ2, SZ, DZ1 and DZ2. This reflects the physical situation in an annular combustor, where pressure variations along the liner are small compared to the absolute combustor pressure. Without this tuning, the default coefficients would introduce artificial pressure differences between zones, which would be non-physical and could destabilise the CRN. Calibrating the valve coefficients is therefore essential to preserve a realistic and numerically consistent combustor pressure field.

3.8. Downstream Steady State

The downstream reactors (PZ2, SZ, DZ1 and DZ2) are solved together in a single `ReactorNet`, shown in Figure 3.6. In contrast to the PZ1 subzones, the downstream zones are coupled through valves and therefore must be integrated as one system. The solver advances the entire chain using `advance_to_steady_state()`, which iteratively integrates the coupled ODE system until all reactors simultaneously satisfy the steady-state criteria.

As in the primary zone, the final solution is independent of the initialisation state. Although each downstream reactor begins at (P_{03}, T_{03}) with a nominal mixture, its composition is completely overwritten by the sustained mass inflow from upstream reactors and air inlets. The reactor evolves toward the thermochemical state dictated solely by:

- the inlet mass flows (PZ1 exhaust, PZ2 air, SZ air, DZ1 air),
- the reactor volumes,
- the finite-rate chemistry,
- the valve mass-flow relationships.

During `advance_to_steady_state()`, the solver handles strong stiffness arising from quenching, NO formation, and CO oxidation in the dilution region. The solution is guaranteed to converge to the unique fixed point of the ODE system for the given boundary conditions. Any spurious transients associated with initialisation decay rapidly and do not influence the final thermodynamic or chemical state.

Once steady state is reached, the outlet of DZ2 is copied into a dedicated reservoir, `final_exhaust`, which forms the basis for emission index calculations. This ensures that the downstream emissions correspond to the true steady-state reactor solution and are not contaminated by intermediate states.

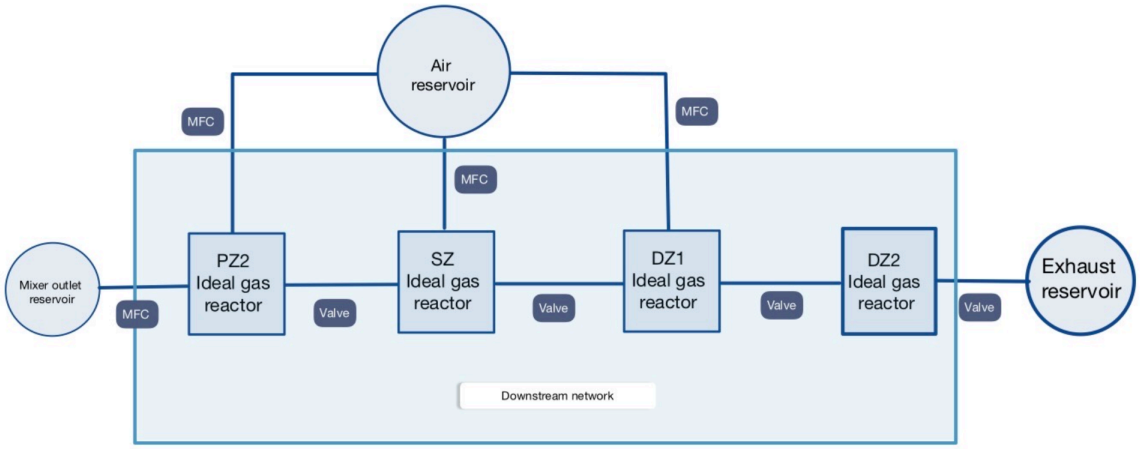

Figure 3.6: Schematic overview of the downstream network.

3.9. Emission Index Calculation

3.9.1. Definitions and NO_2-equivalent weighting

Emission indices are evaluated at the outlet of DZ2 using the steady-state reactor solution. The NO_x emission index follows the ICAO formulation in which NO is converted to an NO_2-equivalent mass using the molar mass ratio $M_{NO_2}/M_{NO} = 46/30$. This ensures direct comparability with the certified ICAO emission indices. Let Y_{NO} and Y_{NO_2} denote the mass fractions at the DZ2 outlet and let $\dot{m}_{out}$ be the total mass flow leaving DZ2. The ICAO-style NO_x mass flow is then

$$\dot{m}_{NO_x,ICAO} = \left(Y_{NO} \frac{46}{30} + Y_{NO_2} \right) \dot{m}_{out}.$$

The corresponding emission index is

$$\mathrm{EI}_{\mathrm{NO_x}} = \frac{\dot{m}_{\mathrm{NO_x,ICAO}}}{\dot{m}_{\mathrm{fuel}}}\, 10^3 \qquad [\mathrm{g/kg\ fuel}].$$

The CO emission index follows the standard definition,

$$\dot{m}_{\mathrm{CO}} = Y_{\mathrm{CO}}\, \dot{m}_{\mathrm{out}}, \qquad \mathrm{EI}_{\mathrm{CO}} = \frac{\dot{m}_{\mathrm{CO}}}{\dot{m}_{\mathrm{fuel}}}\, 10^3.$$

Hydrocarbon emissions are evaluated using a simple flame-ionisation mask that selects all hydrocarbon species detectable by a flame ionisation detector (FID). The carbon molar flow of the selected species is converted to an equivalent CH_4 mass flow and normalised by $\dot{m}_{\mathrm{fuel}}$ to give $\mathrm{EI}_{\mathrm{HC}}$ in g/kg-fuel. This HC index is computed for completeness but not used as an optimisation target. The function `calculate_emission_indices()` returns $\mathrm{EI}_{\mathrm{NO_x}}$, $\mathrm{EI}_{\mathrm{CO}}$ and $\mathrm{EI}_{\mathrm{HC}}$ for use in comparisons with the ICAO limits.

3.9.2. Comparison with ICAO targets and printed diagnostics

Table 3.2: ICAO emission indices for the CF6-80C2B1F (g/kg fuel).

Quantity	T/O	C/O	AP	ID
$\mathrm{EI}_{\mathrm{NO_x}}$	28.11	21.26	8.83	3.73
$\mathrm{EI}_{\mathrm{CO}}$	0.58	0.55	2.37	43.22
$\mathrm{EI}_{\mathrm{HC}}$	0.08	0.09	0.21	9.46

The ICAO reference emission indices for the CF6 are stored in the dictionary `real_targets`, as shown in Table 3.2. A helper routine retrieves the modelled emission indices and prints them alongside the ICAO values together with their relative errors. For instance,

$$\mathrm{Error}_{\mathrm{NO_x}} = \frac{\mathrm{EI}_{\mathrm{NO_x}} - \mathrm{EI}_{\mathrm{NO_x,target}}}{\mathrm{EI}_{\mathrm{NO_x,target}}} \times 100\%,$$

and similarly for CO (and HC if desired). These printed diagnostics are used extensively during optimisation and parameter calibration to quantify how closely the CRN reproduces the certified ICAO emission indices at each LTO power setting.

3.10. Model Verification and Numerical Consistency Checks

The reactor network relies on device based flow connections in which mass flows, pressures and enthalpies are enforced through idealized valves, mass flow controllers and pressure controllers. Although these devices provide a robust framework for composing networks of ideal reactors, they introduce additional degrees of freedom that must be tuned carefully. Before chemically meaningful results can be interpreted, the flow field must be physically consistent. Two aspects require attention in this work. The first is the tuning of valve coefficients to suppress unphysical recirculation and to minimize pressure mismatches across device connections. The second is a convergence study that establishes the required number of parallel PZ1 subzones. Together these steps ensure that the network behaviour remains independent of arbitrary numerical choices.

3.10.1. Tuning valve coefficients for stable flow and pressure consistency

Flow between individual reactors and reservoirs is mediated by Cantera devices, in particular the `Valve`. These devices determine their mass flow from a pressure difference multiplied by a user supplied coefficient. If these coefficients are not chosen carefully, two undesirable effects occur. The first is the risk of backflow and circulation loops within the network. The second is the possibility of pressure drift in downstream reactors because the pressure controller must compete with improperly balanced valve flows. Both effects lead to unrealistic residence times, uncontrolled enthalpy transport and unphysical emission predictions.

To avoid these issues the model is equipped with an iterative tuning routine. It proceeds as follows.

1. The full reactor network is assembled with nominal valve coefficients.

2. The network is advanced toward steady state with chemistry frozen. This isolates the behaviour of the device network and reveals pressure differences and mass flow signs across each valve.
3. The inlet and outlet mass flows of each reactor, as well as the sign and magnitude of the pressure difference across each valve, are analysed. If a valve exhibits backflow or produces an unrealistic pressure drop, its coefficient is reduced or increased according to a proportional update rule.
4. The network is rebuilt with the updated coefficients and the procedure is repeated in a loop until all of the following hold:

    - the mass flow direction through each valve matches the intended topology of the combustor;
    - pressure differences between connected reactors remain negligible (less than 1%) compared to the operating pressure;
    - the pressure controller requires only minimal correction to maintain the global combustor pressure.

This tuning step produces a stable set of valve coefficients that suppresses circulation and maintains a nearly isobaric environment. The final coefficients are then fixed for all subsequent chemically reacting simulations.

3.10.2. Subzone convergence study for the primary zone

Incomplete mixing in the primary zone is represented by N parallel PZ1 subzones that discretise the truncated mixture fraction distribution defined by the unmixedness parameter s (see Section 2.8). The choice of N is purely numerical and must be large enough that predicted emission indices are insensitive to further refinement. To determine a suitable value of N a dedicated convergence script was written, which imports the engine class from the main script and is able to override parameter N.

The study fixes the primary zone mixture parameters to the generic RQL equivalence ratios for each thrust setting and sets $s = 0.7$ so that the convergence will be computed for a relatively high unmixedness. It varies only the number of PZ1 subzones. For the CF6 case considered here the convergence is tested at two operating conditions:

- Approach (AP), where CO is most constraining because of relatively low temperatures.
- Idle (ID), where NO_x is most sensitive because residence times are long and temperatures in the lean burn part of the combustor are modest.

For both AP and ID a high resolution reference solution is first computed with

$$N_{\mathrm{ref}} = 100$$

subzones in PZ1. This reference provides emission indices

$$EI^{\mathrm{ref}}_{\mathrm{NO_x},j}, \qquad EI^{\mathrm{ref}}_{\mathrm{CO},j},$$

for $j \in \{\mathrm{AP}, \mathrm{ID}\}$, where $EI_{\mathrm{NO_x}}$ is the NO_x emission index on the ICAO basis with the NO_2 weighting already applied in the emission post processing. For any candidate number of subzones N the same reactor network is solved and the corresponding emission indices

$$EI_{\mathrm{NO_x},j}(N), \qquad EI_{\mathrm{CO},j}(N)$$

are compared to the reference through the relative errors

$$\Delta_{\mathrm{NO_x},j}(N) = \left| \frac{EI_{\mathrm{NO_x},j}(N) - EI^{\mathrm{ref}}_{\mathrm{NO_x},j}}{EI^{\mathrm{ref}}_{\mathrm{NO_x},j}} \right|, \tag{3.1}$$

$$\Delta_{\mathrm{CO},j}(N) = \left| \frac{EI_{\mathrm{CO},j}(N) - EI^{\mathrm{ref}}_{\mathrm{CO},j}}{EI^{\mathrm{ref}}_{\mathrm{CO},j}} \right|. \tag{3.2}$$

The script uses the following tolerances, defined once and reused for both operating conditions:

$$\Delta_{\mathrm{NO_x},j}(N) \le 0.10, \qquad \Delta_{\mathrm{CO},j}(N) \le 0.15,$$

which correspond to a ten percent tolerance on NO_x and a fifteen percent tolerance on CO. This approach is consistent with the discussion in the background chapter. The selection problem can be written as a constrained search for the smallest N such that both AP and ID satisfy the tolerances,

$$\text{find the minimal } N \quad \text{such that} \quad \Delta_{\mathrm{NO_x},j}(N) \le 0.10, \quad \Delta_{\mathrm{CO},j}(N) \le 0.15 \quad \forall j \in \{\mathrm{AP}, \mathrm{ID}\}. \tag{3.3}$$

In practice the script proceeds in two stages. First, a coarse forward sweep in N is performed for AP. Starting from $N = 20$ and, if the condition is not yet satisfied, either increases or decreases in steps of five. The network is solved and the errors $\Delta_{\mathrm{NO_x,AP}}(N)$ and $\Delta_{\mathrm{CO,AP}}(N)$ are evaluated. The first value of N that satisfies both tolerances is stored as N_{AP}. If no N up to N_{ref} meets the criteria, the reference value $N_{\mathrm{AP}} = N_{\mathrm{ref}}$ is adopted.

Second, the same procedure is applied to ID, starting at N_{AP} since Idle cannot require fewer subzones than already determined for Approach. A coarse sweep in steps of five produces a first acceptable value $N_{\mathrm{ID,coarse}}$. A fine backward sweep is then carried out one by one from $N_{\mathrm{ID,coarse}}$ downwards, and the smallest N that still satisfies both NO_x and CO tolerances at Idle is taken as the final N_{ID}.

All intermediate results, including the absolute emission indices and the percent deviations for both operating points and all tested N, are written to an Excel file for inspection. The procedure showed that both $EI_{\mathrm{NO_x}}$ and EI_{CO} at Approach and Idle stabilise once thirteen subzones are used. This value was therefore adopted as the default number of PZ1 subzones in all subsequent simulations.

3.10.3. Mass flow consistency checks

As an additional verification step, all mass flows entering and leaving each reactor, mixer and device were exported and checked for mass conservation in a spreadsheet. This confirmed that the tuned valve coefficients enforce mass balance within numerical precision and that the intended air split and fuel distribution are preserved exactly at every operating point.

3.11. Water injection implementation in the CRN framework

Water injection is incorporated into the CRN as an optional modification of the primary zone inlet streams. The implementation is kept fully general so that it applies to any combustor geometry. This section explains how injected water is parameterised, how it is mixed into the subzone inlets, and how it propagates through the network without disrupting the established air-fuel budget or equivalence ratio specification.

3.11.1. Parameterisation of injected water

The model introduces a single non-dimensional parameter,

$$\lambda_{w/f} = \frac{\dot{m}_{\mathrm{H_2O}}}{\dot{m}_f}, \tag{3.4}$$

where $\dot{m}_{\mathrm{H_2O}}$ is the mass flow of injected water and $\dot{m}_f$ is the total fuel mass flow at the operating point. The parameter is interpreted as kilograms of gaseous water added per kilogram of fuel and is passed directly to the engine constructor via

```
water_to_fuel = ...
```

A value of $\lambda_{w/f} = 0$ corresponds to the dry reference configuration. The parameter is not redistributed or re-scaled later; it enters only once at the definition of the PZ1 inlet compositions.

3.11.2. Location of water addition within the network

Water is introduced exclusively at the PZ1 inlet, before any subzone calculation. No water is introduced in the secondary, quench or dilution air streams. This ensures that:

1. the fuel and air mass flows remain identical to the dry configuration,
2. all equivalence ratios prescribed for PZ1, PZ2 and SZ remain unchanged,
3. the only modification to the chemical state is the additional steam content and its associated enthalpy and heat-capacity effects.

Thus water affects the entire reactor network only through the detailed thermochemistry after PZ1, not by altering the imposed air budget or mixer design.

3.11.3. Adjustment of PZ1 inlet states

For each PZ1 subzone i the dry inlet mass flows are first computed:

$$\dot{m}_{f,i}^{\text{dry}} = w_i \dot{m}_f, \tag{3.5}$$

$$\dot{m}_{a,i}^{\text{dry}} = \frac{\dot{m}_{f,i}^{\text{dry}}}{\phi_{1,i} f_{\text{st}}}, \tag{3.6}$$

with w_i the subzone weight and f_{st} the stoichiometric fuel-air ratio. Using these, the dry total mass flow is

$$\dot{m}_{\text{dry},i} = \dot{m}_{f,i}^{\text{dry}} + \dot{m}_{a,i}^{\text{dry}}. \tag{3.7}$$

A Cantera `Solution` is then prepared at the compressor exit state (T_{o3}, P_{o3}) and set to the desired dry equivalence ratio. This produces the vector of dry mass fractions Y^{dry} for fuel and air only.

When water injection is enabled, the model derives the fraction of steam to be added such that fuel and air flows remain unchanged. Let

$$r = \lambda_{w/f}, \qquad f_i = \frac{\dot{m}_{f,i}^{\text{dry}}}{\dot{m}_{\text{dry},i}}, \tag{3.8}$$

denote the dry fuel fraction in the subzone inlet. The mass fraction of injected water required to achieve the desired ratio r is

$$Y_{\text{H}_2\text{O},i} = \frac{r f_i}{1 + r f_i}. \tag{3.9}$$

This ensures that

$$\dot{m}_{\text{H}_2\text{O},i} = r \dot{m}_{f,i}^{\text{dry}}, \tag{3.10}$$

while fuel and air mass flows remain exactly at their dry values.

The total inlet mass flow therefore becomes

$$\dot{m}_{\text{wet},i} = \frac{\dot{m}_{\text{dry},i}}{1 - Y_{\text{H}_2\text{O},i}}, \tag{3.11}$$

and the inlet composition is updated to include the added steam,

$$Y_j^{\text{wet}} = (1 - Y_{\text{H}_2\text{O},i}) Y_j^{\text{dry}} \quad \text{for all } j \neq \text{H}_2\text{O}, \tag{3.12}$$

$$Y_{\text{H}_2\text{O}}^{\text{wet}} = Y_{\text{H}_2\text{O},i}. \tag{3.13}$$

The reservoir feeding subzone i is finally set to

$$T = T_{o3}, \qquad P = P_{o3}, \qquad Y = Y^{\text{wet}},$$

which corresponds to injecting fully vapourised water at compressor exit conditions.

3.11.4. Propagation of injected water through mixers and downstream zones

All downstream operations remain unchanged. Once each PZ1 subzone reaches steady state, its outlet stream enters the mixing procedure exactly as in the dry network. The mixer uses an enthalpy-preserving `Quantity` addition,

$$q_{\text{mix}} = \sum_i q_i,$$

where each q_i contains the wet mass flow $\dot{m}_{\text{wet},i}$ and the corresponding composition. As a result the injected water automatically participates in the adiabatic mixing step and flows into PZ2 with the correct mass weighting.

Because the secondary and dilution air flows are computed strictly from the dry fuel and air budget and the imposed equivalence ratios, the added steam does not influence the air split. It simply increases the total mass processed by each zone and modifies the temperature, specific heats and reaction pathways through the detailed mechanism.

3.11.5. Impact on residence times and downstream chemistry

The model does not change zone volumes when water injection is applied. The residence time in each zone therefore adjusts naturally according to

$$\tau = \frac{m_{\text{zone}}}{\frac{1}{2}\left(\dot{m}_{\text{in}} + \dot{m}_{\text{out}}\right)}, \tag{3.14}$$

where $\dot{m}_{\text{in}}$ and $\dot{m}_{\text{out}}$ include the added water. Injected steam increases the total mass flow and reduces local flame temperatures, which shifts NO_x production primarily through thermal-NO suppression and altered radical pathways. These effects arise entirely from the detailed kinetics and thermodynamics; no empirical correction is applied to the chemistry.

3.11.6. Diagnostic output and consistency checks

For each run the model records the injected water mass flow and prints the total water added into the primary zone, which provides a straightforward validation of the imposed $\lambda_{w/f}$. No dedicated emission-index modifications are required because all quantities are evaluated directly from the DZ2 outlet composition using the standard procedure.

In summary, the water injection implementation is fully conservative with respect to fuel and air flows, preserves all equivalence-ratio definitions, adds steam at the compressor exit state, and allows the detailed chemistry to determine the effects on ignition delay, temperature, CO oxidation and NO_x formation throughout the CRN.

3.12. Methodology Summary

The modelling framework developed in this work constructs a detailed chemical reactor network representation of an RQL combustor and systematically ensures numerical consistency before any emission predictions are interpreted. The reactor network is assembled from ideal reactor elements, connected through valves, mass flow controllers and pressure controllers that enforce the required mass flow distribution and global combustor pressure. To guarantee a stable and physically meaningful flow field, the coefficients of these device connections are first tuned in an iterative procedure that suppresses unintended recirculation and minimises pressure differences between connected zones. Once the device network is stabilised, all reactors are advanced to steady state and their initialisation is fully overwritten by the converged chemical solution imposed by the inlet flows and network topology.

Mixing in the primary zone is represented by a parallel set of PZ1 subzones that discretise the mixture fraction distribution defined by the unmixedness parameter. A dedicated convergence study determines the minimum number of subzones required for emission predictions to be insensitive to numerical resolution. Approach and Idle conditions are used as the most restrictive operating points and the smallest number of subzones that reproduces both NO_x and CO emission indices within the defined tolerances is selected. This yields a numerically efficient yet physically representative configuration that is fixed for all subsequent simulations.

Together these steps establish a reactor network that is stable, consistent and free from artefacts introduced by the numerical setup. The model can thus be used reliably to examine the influence of mixture preparation, residence times and water injection on the formation pathways of NO_x and CO in an RQL combustor across the relevant operating conditions.

4

Validation

4.1. CF6 Engine Validation

4.1.1. Reference inputs and targets

For the CF6 engine the four landing-takeoff (LTO) operating points are used as a reference. For each thrust setting the ICAO databank provides target emission indices of NO_x and CO on a fuel based basis. These values are used as optimisation targets for each thrust setting.

The model computes $EI_{\mathrm{NO_x}}$ with the NO_2 weighting consistent with the ICAO definition and EI_{CO} directly from the CRN outlet. A small print helper reports the relative deviations

$$\varepsilon_{\mathrm{NO_x}} = \left| \frac{EI_{\mathrm{NO_x}} - EI_{\mathrm{NO_x}}^{\mathrm{ICAO}}}{EI_{\mathrm{NO_x}}^{\mathrm{ICAO}}} \right|, \qquad \varepsilon_{\mathrm{CO}} = \left| \frac{EI_{\mathrm{CO}} - EI_{\mathrm{CO}}^{\mathrm{ICAO}}}{EI_{\mathrm{CO}}^{\mathrm{ICAO}}} \right|,$$

for each run. This gives a direct and transparent view of how close a given parameter set comes to the ICAO values.

4.1.2. Optimisation setup and objective function

Each power setting is tuned with an Optuna study that wraps the CF6 CRN model in a black box objective function. The optimisation script imports the `CF6Engine` class, which returns the ICAO based NO_x emission index and the CO emission index for a given combination of $\phi_{\mathrm{PZ1}}, \phi_{\mathrm{PZ2}}, \phi_{\mathrm{SZ}}$ and the unmixedness parameter S. The search variables are:

- ϕ_{PZ1}: rich primary zone one equivalence ratio,
- ϕ_{PZ2}: premixed mixture at the outlet of PZ1,
- ϕ_{SZ}: lean mixture in the secondary zone,
- S: unmixedness parameter that controls the spread of the PZ1 subzone distribution.

Each trial therefore corresponds to a full CRN evaluation. Inside the objective, the engine is instantiated with the current candidate parameters and advanced to steady state. Considering the computational time this requires, the script writes the trials to a shared file so that multiprocessing can be performed. The model returns $(EI_{\mathrm{NO_x}}, EI_{\mathrm{CO}})$ for the power setting under consideration. These are compared to the ICAO values and combined into a single scalar cost. In code this is a simple function of the relative errors in NO_x and CO; conceptually it can be written as

$$J(\phi_{\mathrm{PZ1}}, \phi_{\mathrm{PZ2}}, \phi_{\mathrm{SZ}}, s) = w_{\mathrm{NO_x}}\, \varepsilon_{\mathrm{NO_x}}^2 + w_{\mathrm{CO}}\, \varepsilon_{\mathrm{CO}}^2,$$

with equal weighting for the two pollutants. Trials for which the reactor network fails to converge or Cantera throws an exception are marked as unusable and pruned by raising `TrialPruned` inside the exception handler. Optuna then avoids revisiting such regions of parameter space.

The Optuna study is configured with a tree structured Parzen estimator sampler and a median based pruner. In code this is done through

```
study = optuna.create_study(
    direction = "minimize",
    sampler   = optuna.samplers.TPESampler(n_startup_trials=40),
    pruner    = optuna.pruners.MedianPruner(),
)
```

The TPE sampler first performs a set of exploratory startup trials to map the response surface and then builds two probabilistic models for good and bad parameter regions. New candidates are sampled from the distribution that is more likely to improve the current best objective. The pruner can terminate trials early when they are clearly worse than the median of completed trials, which limits the time spent on unpromising combinations.

Finally, a warm start is provided by enqueueing a physically reasonable parameter set before the main optimisation loop. For example, for the climbout point the script enqueues

```
study.enqueue_trial({
    'phi_PZ1': 1.64,
    'phi_PZ2': 0.621,
    'phi_SZ':  0.561,
    's':       0.21,
})
```

This seeds the search near a known good region and allows the TPE sampler to refine around it while still exploring alternatives during the startup phase.

4.1.3. Sequential optimisation strategy and manual supervision

The CF6 validation does not treat each power setting in isolation. Instead the optimisation is done in a sequence from high to low thrust. First the takeoff point is optimised, then climbout, then approach and finally idle. At takeoff all four variables have the most freedom. For the lower power settings the same four variables are allowed to vary in the Optuna study, but their range is constrained within the script to enforce a physically consistent cascade:

- $\phi_{\text{PZ1}}, \phi_{\text{PZ2}}, \phi_{\text{SZ}}$ must decrease with decreasing thrust,
- S must increase slightly with decreasing thrust.

This means that whatever equivalence ratios were found to be the optimum for takeoff, will subsequently serve as the upper limits of the optimization script used in climbout. Whatever s was found for takeoff will be the lower limit of the range in s for climbout, and so on. During the optimisation the runs are monitored in real time. The helper prints the current EIs and errors for each trial, which makes it possible to see when the study has converged to a basin that both matches the ICAO values reasonably well and respects the expected trends in ϕ and s. For each power setting the final parameter set is therefore chosen as the Optuna trial that has the lowest objective value among those that also satisfy the monotonicity constraints between LTO points. This combination of automatic search and manual intervention between thrust settings avoids pathological optima that would produce nonphysical parameter jumps between neighbouring power settings.

4.1.4. Optimised mixture parameters

The resulting mixture parameters for CF6 are summarised in Table 4.1. They show a smooth evolution from rich, strongly mixed takeoff conditions towards leaner and slightly more unmixed operation at idle.

Table 4.1: Optimised mixture parameters for CF6 at the four LTO power settings.

Thrust setting	ϕ_{PZ1}	ϕ_{PZ2}	ϕ_{SZ}	s
T/O	1.82	0.704	0.593	0.327
C/O	1.64	0.621	0.561	0.373
AP	1.63	0.520	0.506	0.375
ID	1.58	0.410	0.374	0.387

All three equivalence ratios decrease as thrust is reduced. The rich primary zone becomes gradually less rich and both PZ2 and SZ move further into the lean regime. At the same time the unmixedness parameter rises from $S = 0.327$ at takeoff to $S = 0.387$ at idle. The small increase between climbout and approach and the further increase towards idle are qualitatively consistent with lower mass flows and weaker mixing at low thrust. The final parameter set therefore conforms to a realistic RQL operating envelope.

4.1.5. Comparison against ICAO emission indices

Table 4.2 compares the modelled emission indices, found using the optimized parameters, with the ICAO databank values for NO_x and CO at the four LTO points.

Table 4.2: CF6 emission indices from ICAO databank and from the CRN model.

Thrust setting	$EI_{NO_x}^{ICAO}$ [g/kg fuel]	$EI_{NO_x}^{model}$ [g/kg fuel]	NO_x error [%]	EI_{CO}^{ICAO} [g/kg fuel]	EI_{CO}^{model} [g/kg fuel]	CO error [%]
T/O	28.11	28.19	0.28	0.58	0.58	-0.64
C/O	21.26	21.12	-0.67	0.55	0.55	-0.09
AP	8.83	10.80	22.40	2.37	2.38	0.54
ID	3.73	6.41	71.80	43.22	31.72	-26.60

At takeoff and climbout the agreement is excellent. NO_x errors remain below one percent in magnitude and CO is matched to within one percent as well. This is a strong indication that the combination of residence time formulation, mixing model and Dagaut mechanism captures the dominant NO_x and CO chemistry in the hot RQL regime.

At approach the model slightly overpredicts NO_x, with an error of about 22 percent. In absolute terms this corresponds to a difference of less than two grams of NO_x per kilogram of fuel, because the reference value itself is small. CO at approach is matched almost perfectly. The model reproduces the transition towards lower NO_x and higher CO at intermediate thrust, even though the NO_x level is shifted upward modestly.

At idle the relative NO_x error appears large at about seventy two percent. However, the absolute difference between model and databank is still modest: roughly $6.41 - 3.73 \approx 2.7$ g/kg fuel. NO_x levels at idle are very small and therefore highly sensitive to both modelling details and measurement uncertainties in the ICAO dataset. For CO the model underpredicts the idle value by about eleven grams per kilogram of fuel. Despite this offset the qualitative trend is captured correctly. CO increases strongly when going from takeoff to idle and the model reproduces that monotonic rise.

Overall, the model recovers the key emission trends across the LTO cycle. NO_x decreases with decreasing thrust, CO increases sharply towards idle and both pollutants exhibit the expected intermediate behaviour at climbout and approach. Where percent errors are large this is mainly due to the very small reference values, rather than extremely large absolute discrepancies. The ICAO databank itself also carries measurement uncertainty and engine to engine variability, especially at low power where sampling and instrument limitations are most pronounced. Within this context the remaining deviations are acceptable for the purpose of using CF6 as a validated reference case.

In summary, the CF6 optimisation reproduces the ICAO emission indices at the most chemically demanding points, takeoff and climbout, with excellent accuracy. At approach and idle the absolute deviations remain modest, especially considering the uncertainty margin of both the ICAO databank and low-power CRN predictions. Crucially, the evolution of the optimised parameters $\phi_{PZ1}, \phi_{PZ2}, \phi_{SZ}$ and s across the LTO cycle, together with the corresponding NO_x and CO trends, is physically consistent and follows the expected behaviour of an RQL combustor as thrust decreases.

For the purposes of this research the agreement in *trends* is the primary requirement. The central research questions focus on the mechanisms and relative changes in NO_x formation under water-injected conditions, which depend more strongly on how the model responds to variations in mixture preparation, temperature and residence time than on exact matching of idle emissions. Furthermore, water injection is neither relevant nor intended for the idle setting, making the high relative idle errors less consequential for the intended application.

Taken together, the accurate high-power predictions, the physically coherent behaviour across the full LTO sequence and the acceptable absolute deviations at low power demonstrate that the CF6 case

provides a sufficiently robust and representative validation of the modelling framework for the scope of this study.

4.2. Residence time transfer and calibration for XWB-84

The XWB-84 combustor geometry is constructed using a two-stage residence-time transfer and calibration procedure. The starting point is the validated CF6 takeoff solution, from which a set of reference residence times τ_{ref} is extracted for all zones. These times encode the chemical time scales that produced the correct NO_x-CO balance in the CF6 reference case. The XWB geometry is then generated such that each zone satisfies

$$V_{\text{zone}} = \dot{m}_{\text{zone}}\ \tau_{\text{ref}},$$

using the XWB-84 mass flows at the new operating point. This ensures that the characteristic reaction times are preserved under changes in inlet flow, pressure and temperature. The resulting volumes are written to a JSON file and reused across all XWB-84 modes.

Because the detailed combustor geometry of the XWB-84 is not publicly available, a direct volume-based reconstruction would require unverifiable assumptions about liner shape and zone partitioning. In contrast, the CF6 geometry used in earlier work is well characterised and has already produced validated NO_x-CO behaviour within this CRN framework. Transferring the CF6 residence times therefore provides a physically grounded way to impose realistic chemical time scales on the XWB-84 model without relying on speculative geometric inputs. A calibration step remains necessary because the numerical residence times in the PSR network depend on the steady-state reactor mass, which shifts under the new XWB inlet conditions due to changes in density and temperature. These effects cause τ_{num} to deviate from the intended τ_{ref}. The one-pass calibration restores consistency by rescaling volumes so that the numerical residence times match the reference chemical time scales across all zones.

After this initial sizing, the model performs a one-pass $\tau \rightarrow V$ calibration round at XWB-84 takeoff, implemented in `calibrate_tau_once()` in the engine code. First the network is assembled with the transferred volumes and advanced to steady state. The code then measures the numerical residence times in all zones using the internal diagnostic function `_measure_taus()`, which computes

$$\tau_{\text{num}} = \frac{m_{\text{reactor}}}{0.5\,(\dot{m}_{\text{in}} + \dot{m}_{\text{out}})}$$

for every reactor and averages over all PZ1 subzones. For each zone a scale factor

$$s = \frac{\tau_{\text{ref}}}{\tau_{\text{num}}}$$

is computed. PZ1 volumes are scaled uniformly to preserve identical τ across subzones, while downstream zones (PZ2, SZ, DZ1, DZ2) are rescaled individually. The network is rebuilt once with these calibrated volumes and advanced again. The final volumes are those written into the XWB-84 geometry JSON and used for all LTO and cruise simulations.

The CF6 reference residence times used for transfer are listed in Table 4.3. Values are shown in milliseconds.

Table 4.3: CF6 reference residence times at takeoff (rounded).

Zone	τ [ms]
PZ1	5.523
PZ2	0.390
SZ	1.512
DZ1	1.086
DZ2	0.655
Total	9.166

The XWB-84 volumes resulting from the full transfer and calibration step are listed in Table 4.4.

Table 4.4: XWB-84 volumes obtained from residence-time transfer and calibration.

Zone	V [m^3]
PZ1 (total)	0.020706
PZ2	0.003051
SZ	0.012816
DZ1	0.011661
DZ2	0.007031
Total	0.055265

4.3. Validation protocol for XWB-84

4.3.1. LTO comparison

The XWB-84 LTO validation follows the same optimisation and comparison procedure as for the CF6. Thrust levels are taken from the ICAO databank. Combustor inlet data (P_3, T_3, total inlet mass flow and fuel flow) were obtained from engine performance maps supplied within the , see Appendix A. These values were digitised where necessary and cross-checked for consistency. All XWB-84 LTO inputs used in the model are listed in Table 4.5.

Table 4.5: XWB-84 LTO inputs used for validation.

Setting	Thrust [kN]	$\dot{m}_{\text{fuel}}$ [kg/s]	$\dot{m}_{\text{total}}$ [kg/s]	FAR	P_3 [bar]	T_3 [K]
T/O	379.0	2.819	115.0	0.0251	53.1	860
C/O	322.2	2.306	104.0	0.0227	45.5	850
AP	113.7	0.801	50.8	0.0160	19.3	675
ID	26.5	0.291	20.6	0.0143	6.9	516

The optimised mixture parameters for XWB-84 across the LTO cycle are given in Table 4.6.

Table 4.6: Optimised XWB-84 mixture parameters across LTO.

Setting	ϕ_{PZ1}	ϕ_{PZ2}	ϕ_{SZ}	s
T/O	1.73	0.717	0.600	0.178
C/O	1.54	0.651	0.590	0.239
AP	1.51	0.524	0.468	0.285
ID	1.49	0.439	0.400	0.300

Modelled and ICAO emission indices for these LTO points are summarised in Table 4.7.

Table 4.7: XWB-84 LTO emission indices: model vs. ICAO.

Setting	$EI_{\text{NO}_x}^{\text{ICAO}}$	$EI_{\text{NO}_x}^{\text{model}}$	NO_x err [%]	$EI_{\text{CO}}^{\text{ICAO}}$	$EI_{\text{CO}}^{\text{model}}$	CO err [%]
T/O	45.48	45.63	0.32	0.39	0.0941	-75.88
C/O	34.53	34.75	0.63	0.39	0.0996	-74.45
AP	11.46	13.44	17.25	1.20	1.184	-1.35
ID	4.73	7.75	63.79	20.66	22.01	6.52

The mixture parameters evolve smoothly with decreasing thrust: all three equivalence ratios become leaner and the unmixedness parameter increases. This behaviour mirrors the CF6 optimisation and is consistent with physical expectations for an RQL combustor across the LTO cycle.

The NO_x comparison shows excellent agreement at T/O and C/O. At AP the absolute deviation remains modest despite a larger percentage error. At idle the absolute NO_x discrepancy is small in absolute terms due to the low baseline value. CO is underpredicted at high thrust but follows the correct qualitative trend. Given the uncertainties in ICAO CO measurements and the relative insensitivity of the present study to idle emissions, these deviations are acceptable for the intended purpose.

4.3.2. Cruise comparison

A key strength of the Trent XWB-84 as a validation case is the availability of recent in-flight reactive nitrogen measurements from the ECLIF3 project, reported by Harlass et al. [39]. These data provide the first NO_x-relevant measurements for a latest-generation, high-bypass turbofan at cruise altitudes and therefore form an essential benchmark for the present model, particularly because the subsequent water injection analysis targets cruise conditions.

4.3.3. Corrected net thrust as common load parameter

Firstly, to compare combustor behaviour and emissions between LTO and cruise on a single axis, this work uses a corrected net thrust fraction as the operating parameter. The idea is to remove the trivial effect of ambient pressure so that sea level LTO points and high altitude cruise can be plotted consistently.

Let the ambient pressure be p_∞ and the reference pressure be $p_{\text{ref}} = 101{,}300$ Pa (ISA sea level). The non dimensional pressure ratio is

$$\delta = \frac{p_\infty}{p_{\text{ref}}}. \tag{4.1}$$

The corrected net thrust for mode i is defined as

$$F_{\text{corr},i} = \frac{F_{\text{net},i}}{\delta_i}, \tag{4.2}$$

where $F_{\text{net},i}$ is the net thrust of the engine in kilonewton at that operating condition and δ_i is the corresponding ambient pressure ratio.

For the LTO modes (idle, approach, climb out, take off) the engine is operated near sea level so $\delta_{\text{LTO}} \approx 1$ and the corrected thrust is essentially equal to the actual thrust. For the cruise modes the ambient pressure at 11 km is much lower, so the same net thrust corresponds to a larger corrected thrust. This correction shifts cruise to higher effective load, in line with its higher combustor temperature and fuel flow.

The non dimensional load parameter used on the horizontal axis is the corrected net thrust fraction relative to take off,

$$\Theta_{F,i} = 100\,\frac{F_{\text{corr},i}}{F_{\text{corr,TO}}} \quad [\%], \tag{4.3}$$

which is equivalent to a percent rated corrected thrust. All LTO and cruise points are then plotted against Θ_F rather than the raw thrust. This ensures that the cruise conditions appear between approach and climb out on the load axis, consistent with their thermodynamic severity.

Table 4.8 summarises the actual net thrust values and the resulting corrected thrust fractions used in the figures.

Table 4.8: Actual net thrust and corrected net thrust fraction Θ_F relative to take off.

Power setting	F_{net} [kN]	Θ_F [%]
T/O	379.0	100.0
C/O	322.2	85.0
CR70	70.0	82.7
CR60	60.0	70.9
AP	113.7	30.0
ID	26.5	7.0

In all thrust resolved plots, the horizontal axis therefore represents Θ_F. This allows LTO and cruise to be interpreted on a single continuous load scale while maintaining the correct physical ordering between idle, approach, climb out, take off and the two cruise points.

In-flight reactive nitrogen measurements from the ECLIF3 project

During ECLIF3, the DLR Falcon probed the *young* exhaust plume (0.3-3.5 s plume age) of an A350-941 equipped with Trent XWB-84 engines. Total reactive nitrogen NO_y was measured using a heated gold converter at $290°$C with hydrogen reduction, followed by chemiluminescence detection of NO [39, Sect. 2.1]. This technique converts all NO_y species (NO, NO_2, HNO_3, PAN, etc.) quantitatively to

NO, ensuring that derived EI_{NO_x} values represent the full engine-emitted reactive nitrogen budget. Simultaneous CO_2 measurements were taken with a high-frequency modified LI-7000 NDIR system, enabling dilution correction and calculation of EI_{NO_x} on a g kg^{-1} fuel basis. Reported uncertainties are approximately 14 % [39, Table 3].

For combustor inlet temperatures comparable to those considered here, Harlass et al. report EI_{NO_x} values in the range 16-22 g kg^{-1} fuel [39, Fig. 5a]. These values serve as the primary comparison for cruise validation.

Cruise operating inputs

Two cruise operating points are considered, at 60 kN and 70 kN net thrust (CR60 and CR70). These thrust levels bracket the typical in-service cruise thrust of the Trent XWB-84 on the A350-900, so realistic cruise operation is expected to lie between them. They are listed in Table 4.9. They were sourced from the supplied project files on engine performance shown in Appendix B.

Table 4.9: XWB-84 cruise inputs used for validation.

Setting	Thrust [kN]	$\dot{m}_{fuel}$ [kg/s]	$\dot{m}_{total}$ [kg/s]	FAR	P_3 [bar]	T_3 [K]
CR70	70	1.000	43.5	0.0235	18.0	802
CR60	60	0.846	40.7	0.0212	16.5	764

Optimised mixture parameters at cruise

The optimised primary and secondary zone equivalence ratios and mixing parameter s for cruise are listed in Table 4.10.

Table 4.10: Optimised mixture parameters ($\phi_{PZ1}, \phi_{PZ2}, \phi_{SZ}, s$) at cruise.

Setting	ϕ_{PZ1}	ϕ_{PZ2}	ϕ_{SZ}	s
CR70	1.53	0.591	0.590	0.265
CR60	1.53	0.585	0.530	0.265

The parameters evolve smoothly with thrust: from CR60 to CR70, the slight increase in ϕ_{PZ2} and ϕ_{SZ} reflects the higher fuel flow and T_3, while s remains constant, consistent with the reduced sensitivity of cruise unmixedness to thrust compared with LTO operation. This is visualized in the plots against corrected net thrust.

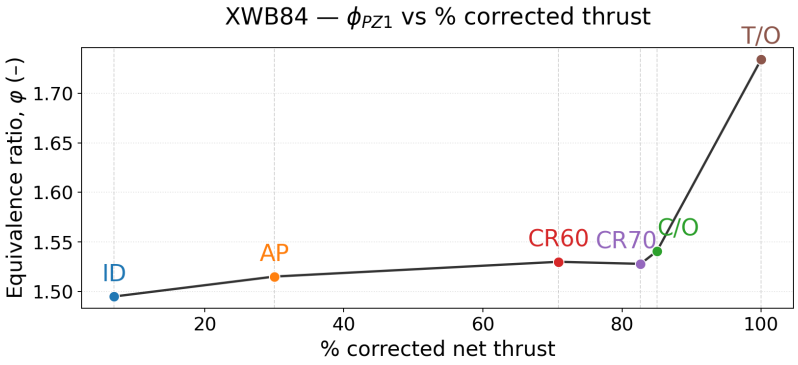

Figure 4.1: Trend in equivalence ratios of primary zone 1, mean of subzones.

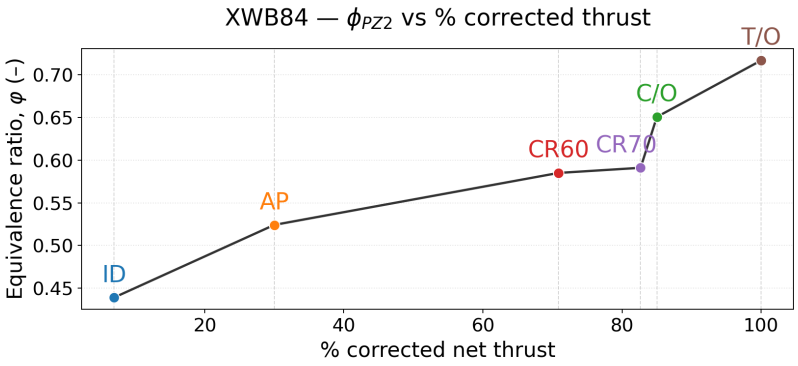

Figure 4.2: Trend in equivalence ratios of primary zone 2.

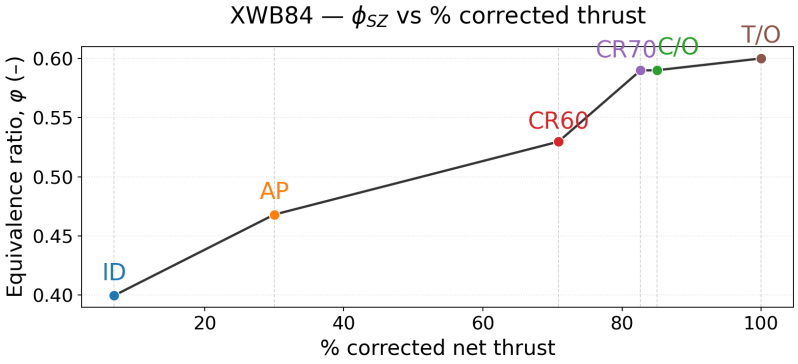

Figure 4.3: Trend in equivalence ratios of the secondary zone.

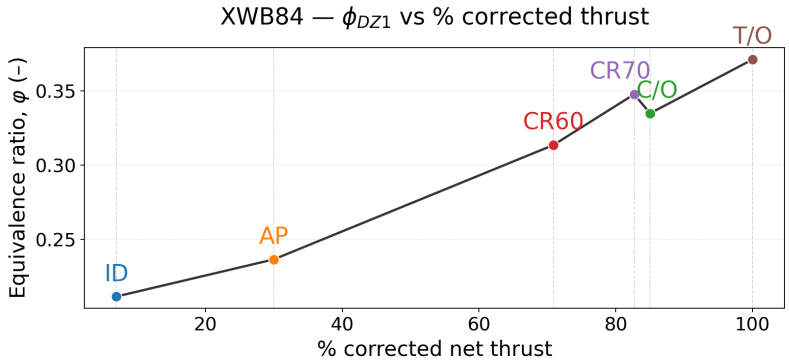

Figure 4.4: Trend in equivalence ratios of dilution zone 1.

Cruise emission comparison

Modelled cruise emission indices are summarised in Table 4.11.

Table 4.11: Modelled XWB-84 cruise emission indices. The in-flight EI_{NO_x} range reported by Harlass et al. [39] for comparable T_3 levels is approximately 16-22 g kg^{-1} fuel.

Setting	EI_{NO_x} [g kg^{-1}]	EI_{CO} [g kg^{-1}]
CR70	22.44	0.32
CR60	17.82	0.38

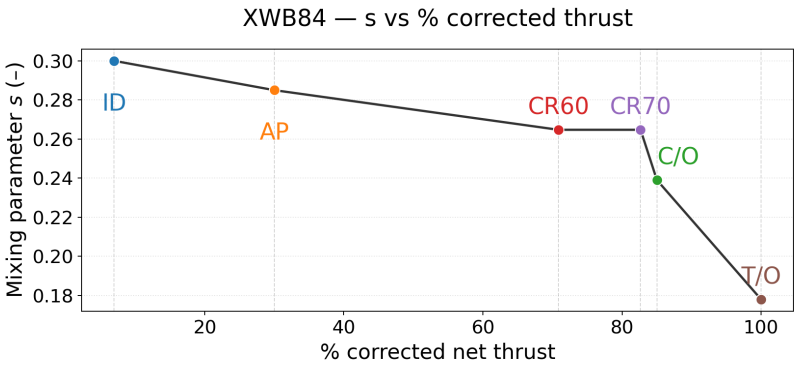

Figure 4.5: Trend in the unmixedness parameter.

Both cruise points fall within or directly at the upper edge of the measured 16-22 g kg^{-1} range. Crucially, the model reproduces the expected positive correlation between $EI_{\mathrm{NO_x}}$ and combustor inlet temperature: $EI_{\mathrm{NO_x}}$ increases from CR60 to CR70 in line with the monotonic trend observed in the ECLIF3 dataset. The CO levels remain low, consistent with lean cruise operation and the short post-flame residence times typical of high-altitude conditions. These trends will be further analyzed in subsection 6.1.1.

Interpretation and relevance

Considering the 14 % measurement uncertainty and the fact that ECLIF3 cruise points were obtained under flight test constraints (including thrust offsets and off-design altitude segments), the agreement between the model and the in-flight $EI_{\mathrm{NO_x}}$ range is good. More importantly for the present research, the model reproduces the *trend* of NO_x formation across cruise power levels. Because the subsequent water injection study relies on understanding relative changes in thermal NO_x sensitivity with T_3, ϕ distribution, and residence time, capturing these trends is of primary importance. The cruise validation therefore confirms that the XWB-84 model provides a robust and physically grounded foundation for analysing water injection at cruise.

4.4. Summary of XWB-84 validation

The XWB-84 validation demonstrates that the residence-time transfer method, combined with the CF6-validated mixing parameters, produces a consistent and physically coherent set of predictions across both LTO and cruise conditions. The optimised ϕ and s values evolve smoothly with decreasing thrust and mirror the expected behaviour of an RQL combustor as mass flow and inlet temperature drop. Emission indices at takeoff and climbout match the ICAO databank closely, while deviations at approach and idle remain acceptable in absolute terms and follow the correct qualitative trends. Cruise predictions fall squarely within the range of published in-flight NO_x data for the Trent XWB-84 and show the expected increase with thrust from CR60 to CR70. Since the research focus lies on understanding relative changes in NO_x formation, water-injection effects and the interplay of mixing and residence times, the trend fidelity demonstrated here is more important than exact matching at low power. Taken together, the LTO and cruise comparisons confirm that the residence-time-based XWB-84 model forms a reliable foundation for the water-injection analysis that follows.

5

Correlation-Based Methods for Emission Prediction

This chapter evaluates two widely used correlation methods for predicting gas turbine emissions, namely the P3T3 method and the Boeing Fuel Flow Method (BFFM2). Both approaches were originally developed to extrapolate emission behaviour from limited ground based measurements and are widely used in inventory modelling and regulatory analysis [40]–[42]. In this work they are used as external benchmarks for the chemical reactor network (CRN) model developed in the previous chapters. The correlations are applied to the CF6-80C2B1F and Trent XWB-84 engines and their predictions are compared to ICAO data, to in flight measurements where available and to the CRN results.

5.1. Motivation and Scope

Emission certification for civil aero engines is based on the ICAO Landing and Takeoff (LTO) cycle. The LTO cycle provides standardised emission indices for four operating modes near the ground, but does not cover climb or cruise conditions. To bridge this gap several correlation based methods were developed that predict emissions from easily available engine parameters. The P3T3 method relates emissions to combustor inlet pressure and temperature, while the Boeing fuel flow method correlates emissions with corrected fuel flow. Neither method resolves local mixture distributions or detailed chemical pathways, but both have become standard tools in aircraft emission inventories and regulatory guidance [40]–[42].

In this chapter the two methods are first described in general form. They are then applied to the CF6-80C2B1F and the Trent XWB-84 using the inlet conditions and ICAO emission indices. For the XWB-84 the Boeing method is also evaluated at cruise conditions, using in flight NO_x measurements as a reference. The final section compares the correlation results to the CRN predictions for both engines.

5.2. The P3T3 Method

5.2.1. General formulation

The P3T3 method was introduced by Rudey and Koff [40] who demonstrated that engine NO_x emissions correlate strongly with combustor inlet pressure and temperature. For practical emission inventories a simplified form is widely used, in which emission indices at different operating points are related by power laws in combustor inlet pressure P_{03} (and sometimes temperature T_{03}).

For NO_x the emission index at a given operating point is written as

$$EI_{\mathrm{NO_x}} = EI_{\mathrm{NO_x,ref}} \left(\frac{P_{03}}{P_{03,\mathrm{ref}}} \right)^{n}, \tag{5.1}$$

where $EI_{\mathrm{NO_x,ref}}$ is the reference emission index at a chosen reference mode, $P_{03,\mathrm{ref}}$ is the corresponding combustor inlet pressure and n is an empirical exponent. Values of n between 0.3 and 0.5 are commonly used in the literature [40], and $n = 0.4$ is adopted here.

For CO the inverse relation is typically used

$$EI_{\mathrm{CO}} = EI_{\mathrm{CO,ref}} \left(\frac{P_{03,\mathrm{ref}}}{P_{03}} \right)^{p}, \tag{5.2}$$

with an exponent p of order unity. In this work $p = 1.0$ is used. The reference mode must be chosen for each engine. For NO_x the Climbout (C/O) mode is used as reference, because its operating condition is closer to typical climb and early cruise conditions than Takeoff. For CO the Approach (AP) mode is used as reference, because the strong rise in CO occurs towards low power and AP provides a more representative anchor point for that behaviour than the leaner C/O condition.

In principle the P3T3 method can include explicit temperature corrections and humidity effects [40], [42], but for the present analysis only the pressure dependence is retained and a single representative humidity level is assumed for all operating points. This simplifies the comparison with the Boeing method, which applies the ambient corrections explicitly.

5.2.2. Application to the CF6-80C2B1F

The CF6 combustor inlet conditions used for the P3T3 calculations are given in Table 5.1, as previously described in chapter 3. The certified ICAO emission indices are reproduced in Table 5.2 for convenience.

Table 5.1: CF6-80C2B1F combustor inlet conditions used for P3T3 calculations.

Quantity	T/O	C/O	AP	ID
P_{03} [bar]	30.48	26.42	12.14	5.88
T_{03} [K]	796.56	768.54	626.44	508.71
$\dot{m}_{\mathrm{fuel}}$ [kg/s]	2.29	1.91	0.69	0.24
$\dot{m}_{\mathrm{air}}$ [kg/s]	124.10	109.97	58.06	33.00

Table 5.2: ICAO certified emission indices for the CF6-80C2B1F.

Quantity [g/kg fuel]	T/O	C/O	AP	ID
$EI_{\mathrm{NO_x}}$	28.11	21.26	8.83	3.73
EI_{CO}	0.58	0.55	2.37	43.22

For NO_x the Climbout point is used as reference, so $EI_{\mathrm{NO_x,ref}} = 21.26$ g/kg and $P_{03,\mathrm{ref}} = 26.42$ bar. For CO the Approach point is used as reference, with $EI_{\mathrm{CO,ref}} = 2.37$ g/kg and $P_{03,\mathrm{ref}} = 12.14$ bar. Equations (5.1) and (5.2) are then evaluated at T/O, C/O and ID with $n = 0.4$ and $p = 1.0$. The resulting P3T3 predictions and their deviations from ICAO values are listed in Table 5.3. The NO_x and CO error columns are provided only for the LTO modes considered here.

Table 5.3: P3T3 predictions for the CF6-80C2B1F LTO cycle.

Mode	$EI_{\mathrm{NO_x}}^{\mathrm{P3T3}}$ [g/kg]	NO_x error [%]	$EI_{\mathrm{CO}}^{\mathrm{P3T3}}$ [g/kg]	CO error [%]
T/O	22.51	-19.9	0.94	+62.8
C/O	21.26	0.0	1.09	+98.0
AP	15.58	+76.4	2.37	0.0
ID	11.66	+212.5	4.89	-88.7

5.2.3. Application to the Trent XWB-84

For the Trent XWB-84 the P3T3 method is applied to the four LTO modes and to two cruise operating points at 11 km and Mach 0.85. The combustor inlet conditions used here are summarised in Table 5.4. The total combustor inlet mass flow $\dot{m}_{\mathrm{total}}$ combines air and fuel, while the fuel to air ratio (FAR) is provided for reference.

Table 5.4: Trent XWB-84 combustor inlet conditions used for P3T3 and Boeing calculations.

Mode	P_{03} [bar]	T_{03} [K]	$\dot{m}_{\text{fuel}}$ [kg/s]	$\dot{m}_{\text{total}}$ [kg/s]	FAR	Thrust [kN]
T/O	53.1	860	2.819	115.0	0.0251	379.0
C/O	45.5	850	2.306	104.0	0.0227	322.2
AP	19.3	675	0.801	50.8	0.0160	113.7
ID	6.9	516	0.291	20.6	0.0143	26.5
CR70	18.0	802	1.000	43.5	0.0235	70.0
CR60	16.5	764	0.846	40.7	0.0212	60.0

The NO_x emission indices are taken from ICAO and from in flight measurements at cruise, as listed in Table 5.5. At T/O, C/O, AP and ID the NO_x values correspond to ICAO certification data. At CR60 and CR70 only an in flight range of approximately 16 to 22 g/kg fuel is available. For the P3T3 comparison the midpoint of this range, 19 g/kg fuel, is used as a reference value in the tables, while the full range is retained in the discussion. CO emission indices are available only for the LTO modes.

Table 5.5: NO_x and CO emission indices for the Trent XWB-84.

Mode	EI_{NO_x} [g/kg]	EI_{CO} [g/kg]
T/O	45.48	0.39
C/O	34.53	0.39
AP	11.46	1.20
ID	4.73	20.66
CR70	16.00-22.00	-
CR60	16.00-22.00	-

As for the CF6, the Climbout mode is used as reference for NO_x, so $EI_{\text{NO}_x,\text{ref}} = 34.53$ g/kg and $P_{03,\text{ref}} = 45.5$ bar. For CO the Approach mode is used as reference, with $EI_{\text{CO,ref}} = 1.20$ g/kg and $P_{03,\text{ref}} = 19.3$ bar. The P3T3 equations (5.1) and (5.2) are then evaluated for all modes. The resulting emission indices are summarised in Table 5.6. For the LTO modes the error columns report deviations from the ICAO values. For CR60 and CR70 the table reports P3T3 values without assigning an error, because only a range of in flight NO_x measurements is available.

Table 5.6: P3T3 predictions for the Trent XWB-84 LTO and cruise modes.

Mode	$EI_{\text{NO}_x}^{\text{P3T3}}$ [g/kg]	NO_x error [%]	$EI_{\text{CO}}^{\text{P3T3}}$ [g/kg]	CO error [%]
T/O	36.73	-19.2	0.44	+11.8
C/O	34.53	0.0	0.51	+30.5
AP	24.50	+113.8	1.20	0.0
ID	16.24	+243.3	3.36	-83.8
CR60	23.01	-	1.40	-
CR70	23.83	-	1.29	-

5.3. The Boeing Fuel Flow Method 2 (BFFM2)

5.3.1. General formulation

The Boeing fuel flow method 2 was developed to provide a robust framework for estimating NO_x, CO and HC emissions from fuel flow data [41]. The method is implemented in ICAO Forecasting and Economic Analysis guidance (FOA3) and in several emission inventory tools [42], [43]. It proceeds in four conceptual steps: installation correction of fuel flow, removal of ambient effects to form reference emission indices (REI), logarithmic regression of REI against a corrected fuel flow factor and reconstruction of emission indices at arbitrary ambient conditions.

Installation corrected fuel flow

The raw fuel mass flow rate $\dot{m}_f$ is converted into an installation corrected fuel flow

$$W_f = \dot{m}_f \, f_{\text{inst}}, \tag{5.3}$$

where f_{inst} is an empirically defined installation factor. These factors account for differences between engine test stand conditions and the reference conditions used to develop the correlations [41], [42]. In this work the LTO installation factors are taken from FOA guidelines, while cruise points use $f_{\text{inst}} = 1$ due to the absence of published values.

Following FOA3, a fuel flow factor W_{ff} is introduced to normalise W_f to reference sea level static conditions. It rescales W_f by ambient pressure, temperature and Mach number. For the static LTO data considered here W_{ff} differs from W_f only by a constant factor. At cruise conditions W_{ff} captures the combined effect of lower pressure, temperature and finite flight Mach number on the effective fuel flow level.

Reference emission indices

The next step removes ambient temperature, pressure and humidity effects from the measured emission indices. This yields reference emission indices EI_{REI} that represent the emission level under standard sea level conditions. The corrections for NO_x and CO follow FOA3 [42]:

$$EI_{\text{NO}_x,\text{REI}} = \frac{EI_{\text{NO}_x}}{\left(\dfrac{\delta_{\text{amb}}^{1.02}}{\theta_{\text{amb}}^{3.3}}\right)^{1/2} \exp(H)}, \tag{5.4}$$

$$EI_{\text{CO,REI}} = \frac{EI_{\text{CO}}}{\theta_{\text{amb}}^{3.3} / \delta_{\text{amb}}^{1.02}}, \tag{5.5}$$

with

$$\theta_{\text{amb}} = \frac{T_{\text{amb}}}{288.15}, \qquad \delta_{\text{amb}} = \frac{P_{\text{amb}}}{101.325},$$

and

$$H = -19\,(\omega - 0.0063)$$

where T_{amb} and P_{amb} are ambient temperature and pressure, ω is the ambient humidity ratio and the reference conditions correspond to ISA sea level. The Mach number enters the definition of the fuel flow factor and the derivation of θ_{amb} for flight conditions, but does not appear explicitly in the REI correction formulas above.

Logarithmic regression

For each pollutant the reference emission indices obtained from LTO measurements are correlated with the fuel flow factor using a logarithmic relation

$$\log_{10} EI_{\text{REI}} = a + b \, \log_{10} W_{ff}, \tag{5.6}$$

where a and b are empirical coefficients. Separate regressions are performed for NO_x and CO.

Reconstruction of operational emission indices

Once the coefficients a and b have been determined from LTO data, the method can be used to predict emissions at any operating point for which the fuel flow and the ambient conditions are known. The predicted reference emission index is obtained from (5.6) and converted back to an operational emission index by reapplying the ambient factors [41], [42]:

$$EI_{\text{NO}_x,\text{BFFM2}} = EI_{\text{NO}_x,\text{REI}} \left(\frac{\delta_{\text{amb}}^{1.02}}{\theta_{\text{amb}}^{3.3}}\right)^{1/2} \exp(H), \tag{5.7}$$

$$EI_{\text{CO,BFFM2}} = EI_{\text{CO,REI}} \frac{\theta_{\text{amb}}^{3.3}}{\delta_{\text{amb}}^{1.02}}. \tag{5.8}$$

For LTO conditions this procedure should reproduce the original emission indices if the regression fits are exact. For other operating points such as cruise the method provides predictions based on the LTO calibrated trends.

5.3.2. Application to the CF6-80C2B1F

For the CF6-80C2B1F the Boeing method is calibrated using the four LTO modes. Ambient temperature and pressure ranges are taken from the ICAO databank and averaged to obtain representative values. The installation factors used here follow FOA guidance [42]: $f_{\text{inst}} = 1.010$ for T/O, 1.013 for C/O, 1.020 for AP and 1.100 for ID. The reference emission indices are formed using the ambient corrections in (5.4) and (5.5), and a logarithmic regression is performed against the fuel flow factor W_{ff} for the four LTO points. The resulting regression coefficients are

$$\log_{10} EI_{\text{NO}_x,\text{REI}} = 1.117 + 0.909 \log_{10} W_{ff}, \tag{5.9}$$

$$\log_{10} EI_{\text{CO},\text{REI}} = 0.376 - 1.985 \log_{10} W_{ff}. \tag{5.10}$$

Figure 5.1 shows the NO_x reference emission indices as a function of installation corrected fuel flow together with the fitted regression line. The four LTO modes lie close to a straight line in logarithmic space. The corresponding CO reference emission indices are shown in Figure 5.2. The scatter is larger for CO, especially at the low power idle point, but is still consistent with a single log linear relation.

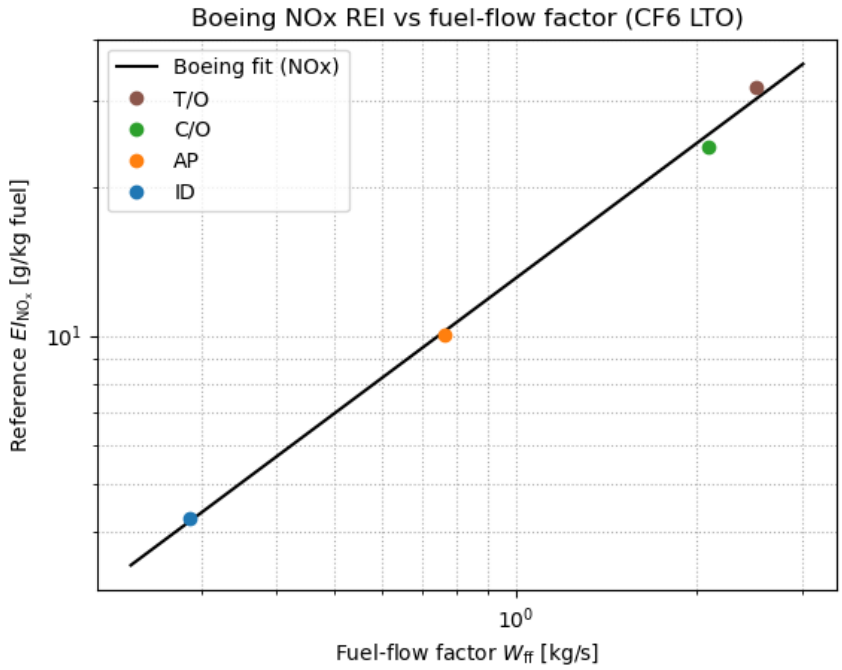

Figure 5.1: NO_x reference emission index versus installation corrected fuel flow for the CF6-80C2B1F. The markers show LTO reference emission indices and the line shows the Boeing fit.

The BFFM2 predictions for the CF6 LTO cycle are summarised in Table 5.7, together with their deviations from ICAO values. The method reproduces NO_x emission indices within roughly six percent at all four modes. For CO the deviations are larger, particularly at idle where the model underpredicts the strong CO rise.

Table 5.7: BFFM2 predictions for the CF6-80C2B1F LTO cycle.

Mode	$EI_{\text{NO}_x}^{\text{BFFM2}}$ [g/kg]	NO_x error [%]	$EI_{\text{CO}}^{\text{BFFM2}}$ [g/kg]	CO error [%]
T/O	26.48	-5.8	0.41	-28.8
C/O	22.51	+5.9	0.59	+7.0
AP	8.98	+1.6	4.38	+84.9
ID	3.68	-1.4	30.69	-29.0

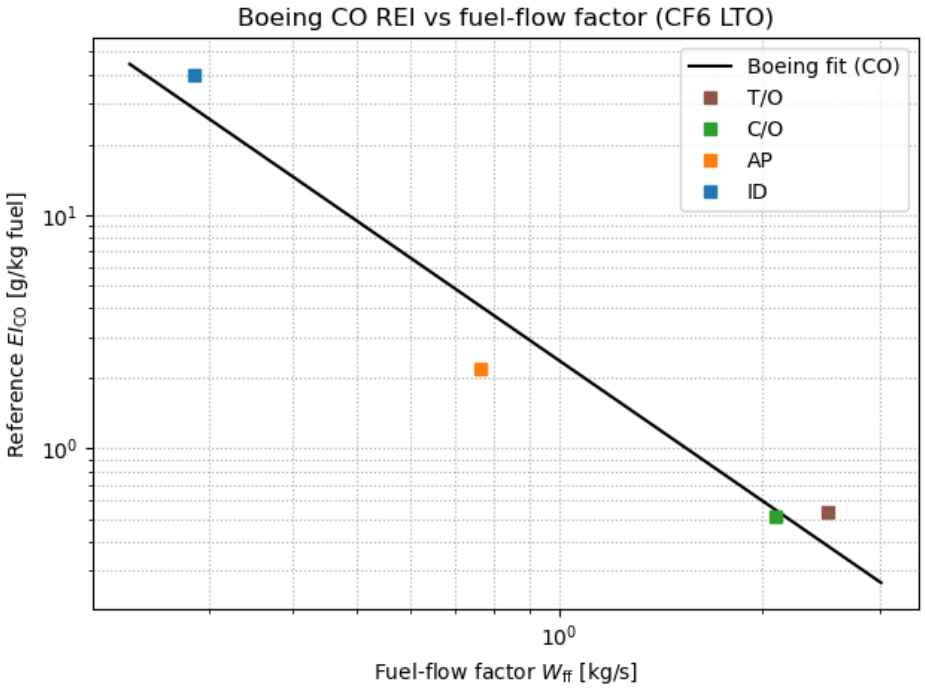

Figure 5.2: CO reference emission index versus installation corrected fuel flow for the CF6-80C2B1F. The markers show LTO reference emission indices and the line shows the Boeing fit.

5.3.3. Application to the Trent XWB-84

For the Trent XWB-84 the Boeing method is again calibrated from the four LTO modes and then applied to two cruise operating points at 11 km and Mach 0.85. The installation factors for the LTO modes follow FOA guidance, while the cruise modes use $f_{\text{inst}} = 1$:

$$f_{\text{inst}} = \begin{cases} 1.010 & \text{T/O}, \\ 1.013 & \text{C/O}, \\ 1.020 & \text{AP}, \\ 1.100 & \text{ID}, \\ 1.000 & \text{CR60, CR70}. \end{cases}$$

The ambient temperature and pressure at LTO are taken from ICAO ranges, averaged to obtain representative values, while cruise conditions are based on ISA at 11 km with Mach 0.85. A single representative humidity ratio of $\omega \approx 0.00606$ kg/kg is used for all modes, consistent with the FOA formulation.

Using the LTO modes only, the regression coefficients for the XWB-84 are

$$\log_{10} EI_{\text{NO}_x,\text{REI}} = 1.170 + 1.029 \log_{10} W_f, \tag{5.11}$$

$$\log_{10} EI_{\text{CO,REI}} = 0.248 - 1.773 \log_{10} W_f. \tag{5.12}$$

Figure 5.3 shows the NO_x reference emission indices against installation corrected fuel flow W_f together with the fitted line. The four LTO points lie close to the regression and the two cruise points are shown as hollow markers to indicate that they are predictions obtained from the fit rather than calibration data. Figure 5.4 presents the corresponding CO reference indices and regression.

Table 5.8 summarises the BFFM2 predictions for the XWB-84 LTO modes. As for the CF6, the method reproduces LTO NO_x closely once calibrated on the same points. For CO the deviations are larger, especially at Approach and Idle.

For the two cruise operating points, Table 5.9 presents the BFFM2 predictions together with the range of in flight NO_x measurements. CO emission indices at cruise are not available from measurement, but the Boeing predictions are included for later comparison with the CRN model.

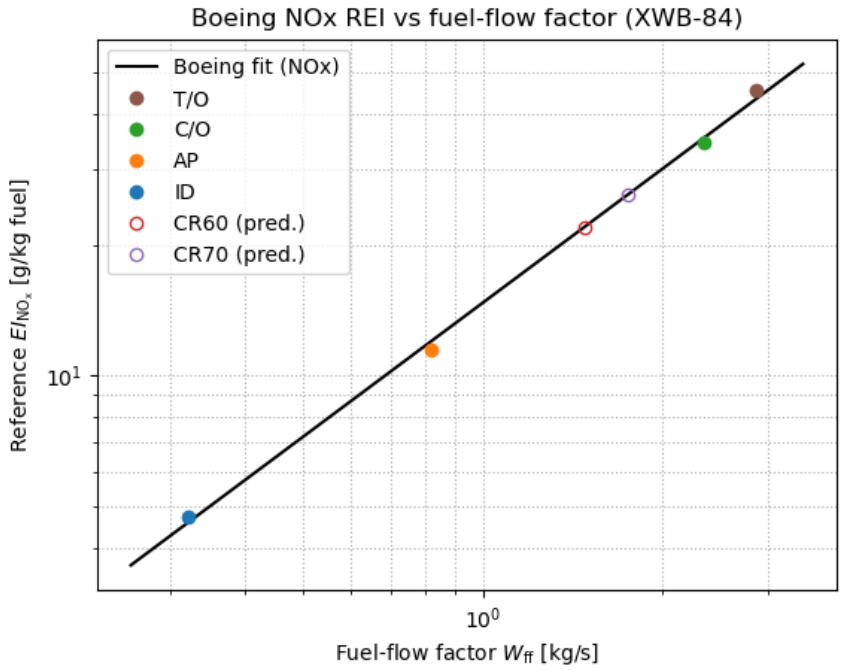

Figure 5.3: NO_x reference emission index versus installation corrected fuel flow for the Trent XWB-84. Filled markers show LTO reference emission indices and hollow markers show cruise values predicted from the regression.

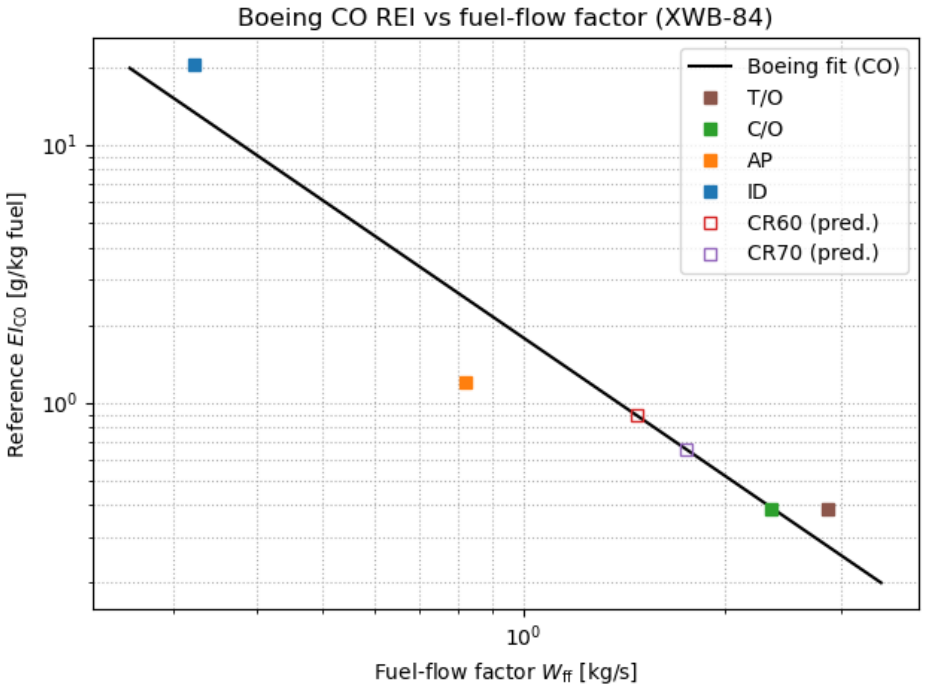

Figure 5.4: CO reference emission index versus installation corrected fuel flow for the Trent XWB-84. Filled markers show LTO reference emission indices and hollow markers show cruise values predicted from the regression.

5.4. Comparison with the Detailed CRN Model

The correlation methods described above provide simple estimates of NO_x and CO emissions based on a small set of engine level inputs. The CRN model developed in this thesis resolves the combustor

Table 5.8: BFFM2 predictions for the Trent XWB-84 LTO cycle.

Mode	$EI_{NO_x}^{BFFM2}$ [g/kg]	NO_x error [%]	EI_{CO}^{BFFM2} [g/kg]	CO error [%]
T/O	43.47	-4.4	0.28	-28.5
C/O	35.46	+2.7	0.40	+1.5
AP	12.03	+5.0	2.55	+112.3
ID	4.59	-3.0	13.42	-35.0

Table 5.9: BFFM2 predictions for Trent XWB-84 cruise modes at 11 km, compared to in flight NO_x ranges [39].

Mode	$EI_{NO_x}^{meas}$ [g/kg]	$EI_{NO_x}^{BFFM2}$ [g/kg]	EI_{CO}^{BFFM2} [g/kg]
CR70	16 to 22	19.60	1.19
CR60	16 to 22	16.50	1.60

zones, mixture distributions and chemical kinetics in more detail. This section summarises how the correlation predictions and CRN results compare to ICAO data for both engines. No interpretation is attempted here; the trends are discussed in the next chapters.

5.4.1. CF6-80C2B1F

Table 5.10 compares NO_x and CO emission indices for the CF6 LTO cycle. For each mode the table lists ICAO values, P3T3 and BFFM2 predictions and the CRN model results, together with the corresponding percentage errors relative to ICAO. The CRN emission indices were taken from the model validation in Chapter 4.1.

Table 5.10: Comparison between ICAO data, correlation methods and CRN model for the CF6-80C2B1F LTO cycle. All emission indices in g/kg fuel.

	EI_{ICAO}	EI_{P3T3}	P3T3 error [%]	EI_{BFFM2}	BFFM2 error [%]	EI_{CRN}	CRN error [%]
				EI_{NO_x}			
T/O	28.11	22.51	-19.9	26.48	-5.8	28.19	+0.3
C/O	21.26	21.26	0.0	22.51	+5.9	21.12	-0.7
AP	8.83	15.58	+76.4	8.98	+1.6	10.80	+22.3
ID	3.73	11.66	+212.5	3.68	-1.3	6.41	+71.8
				EI_{CO}			
T/O	0.58	0.94	+62.8	0.41	-28.8	0.58	0.0
C/O	0.55	1.09	+98.0	0.59	+7.1	0.55	0.0
AP	2.37	2.37	0.0	4.38	+84.9	2.38	+0.4
ID	43.22	4.89	-88.7	30.69	-29.0	31.72	-26.6

The CRN model matches NO_x within about one percent at T/O and C/O and within roughly twenty to seventy percent at AP and ID. CO is reproduced closely at T/O, C/O and AP, while idle CO is under-predicted relative to ICAO. Both correlation methods show similar qualitative features, but with different magnitudes.

5.4.2. Trent XWB-84

For the Trent XWB-84 the CRN model was validated against ICAO LTO data in Chapter 4.3. Table 5.11 compares NO_x and CO emission indices from ICAO, P3T3, BFFM2 and the CRN model for the four LTO modes, again including percentage errors relative to ICAO.

Table 5.11: Comparison between ICAO data, correlation methods and CRN model for the Trent XWB-84 LTO cycle. All emission indices in g/kg fuel.

	EI_{ICAO}	EI_{P3T3}	P3T3 error [%]	EI_{BFFM2}	BFFM2 error [%]	EI_{CRN}	CRN error [%]
				EI_{NO_x}			
T/O	45.48	36.73	-19.2	43.47	-4.4	45.63	+0.3
C/O	34.53	34.53	0.0	35.46	+2.7	34.75	+0.6
AP	11.46	24.50	+113.8	12.03	+5.0	13.44	+17.3
ID	4.73	16.24	+243.3	4.59	-3.0	7.75	+63.8
				EI_{CO}			
T/O	0.39	0.44	+11.8	0.28	-28.5	0.09	-75.9
C/O	0.39	0.51	+30.5	0.40	+1.5	0.10	-74.5
AP	1.20	1.20	0.0	2.55	+112.3	1.18	-1.3
ID	20.66	3.36	-83.8	13.42	-35.0	22.01	+6.5

For the two cruise modes CR60 and CR70 the available reference is an in flight range of NO_x emission indices between 16 and 22 g/kg fuel. Table 5.12 compares these ranges to the P3T3, BFFM2 and CRN predictions. For the error columns a nominal reference of 19 g/kg fuel is used, corresponding to the midpoint of the measured range. Note that the ECLIF3 meassurements do include values within the entire range, so as long as the method result falls within that range it should be considered valid. There are no measured CO emission indices at cruise, so the CO error columns are left empty.

Table 5.12: Comparison between measured emissions [39], correlation methods and CRN model for the Trent XWB-84 cruise modes at 11 km. NO_x errors are computed relative to a nominal reference of 19 g/kg fuel. All emission indices in g/kg fuel.

	Measured range	EI_{P3T3}	P3T3 error [%]	EI_{BFFM2}	BFFM2 error [%]	EI_{CRN}	CRN error [%]
				EI_{NO_x}			
CR70	16-22	23.83	+25.4	19.60	+3.1	22.44	+18.1
CR60	16-22	23.01	+21.1	16.50	-13.2	17.82	-6.2
				EI_{CO}			
CR70	-	0.99	-	1.19	-	0.32	-
CR60	-	1.08	-	1.60	-	0.38	-

Taken together, the tables show that the correlation based methods and the CRN model each reproduce different aspects of the emission behaviour for both engines. The P3T3 and BFFM2 correlations provide compact trends in NO_x versus pressure and fuel flow and give reasonable LTO NO_x estimates once calibrated, but they struggle with CO and with the strong variation between Approach and Idle. The CRN model remains close to ICAO NO_x at T/O and C/O for both engines and tracks the measured cruise NO_x range more closely for the Trent XWB-84, while still showing notable discrepancies at low power CO, particularly at idle. These patterns motivate the more detailed analysis of mixing, temperature and chemistry in the subsequent chapters and provide context for assessing the added value of the CRN model in water injection studies.

6

Results of the Chemical Reactor Network

This chapter presents the results obtained from the detailed chemical reactor network (CRN) simulations. The focus lies on the predicted temperature fields, species evolution, emission indices and reaction-rate distribution across the RQL combustor. On top of that, reaction pathways were investigated. These results form the basis for the subsequent interpretation of water-injection effects and ultimately address the research questions introduced in Chapter 1.2.

The chapter is organised in two parts. The first part examines the dry (non-water-injected) operating conditions of the XWB-84 model and establishes the baseline behaviour of the combustor. The second part investigates how water addition alters the thermochemical environment, pollutant formation and zone behaviour across the same operating envelope.

6.1. Results of the CRN before water injection

This section analyses the dry operating points without water injection. These results establish the baseline performance of the RQL combustor and provide a reference against which the water-injected cases in Section 6.2 can be compared. The key quantities of interest are the emission indices of NO_x and CO, followed by temperature and species evolution within each zone of the network.

6.1.1. Trend in emission indices

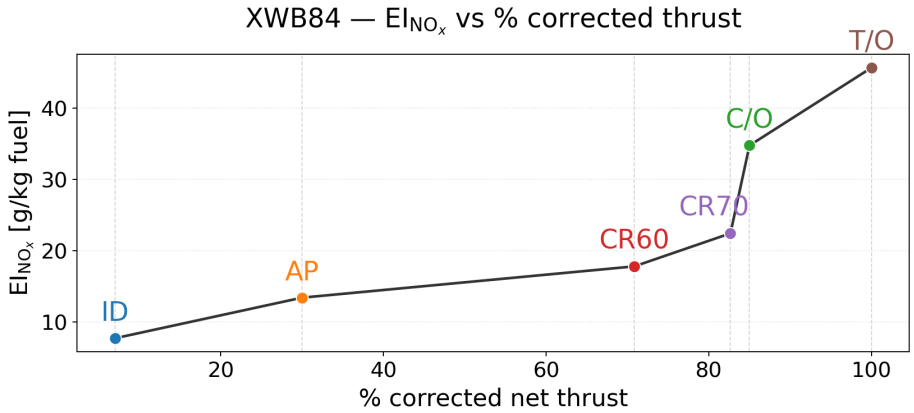

Figure 6.1: Dry case: EI_{NO_x} as a function of corrected net thrust.

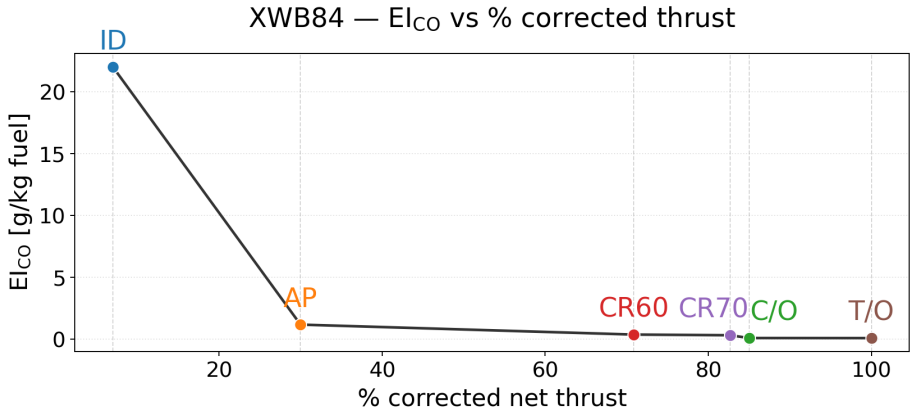

Figure 6.2: Dry case: EI_{CO} as a function of corrected net thrust.

Figure 6.1 shows that the modelled emission index of NO_x increases with corrected net thrust. The idle point lies near $10\,\mathrm{g\,kg^{-1}}$ fuel, after which $EINO_x$ rises smoothly through approach and the two cruise conditions, before reaching approximately $45\,\mathrm{g\,kg^{-1}}$ fuel at take-off. This shape is fully consistent with the RQL combustion principles introduced in Chapter 2. Higher thrust settings correspond to higher combustor inlet temperatures and pressures, together with richer mixtures in the primary zone, all of which favour the Zeldovich thermal pathway. The steep rise between CR70, C/O and T/O in particular reflects the strong temperature sensitivity of thermal NO formation. The absence of any non-monotonic behaviour confirms that the network maintains a stable rich-quench-lean structure throughout the operating envelope.

Figure 6.2 shows the corresponding trend in the emission index of CO. Here the behaviour is strongly non-linear and inverted relative to NO_x. The idle point exhibits a much larger EI_{CO} than any other operating mode, with values exceeding $20\,\mathrm{g\,kg^{-1}}$ fuel. This high CO level is expected, since idle is characterised by a low global temperature and a short effective residence time in the downstream lean zones, which together limit the oxidation of CO to CO_2. As thrust increases from idle to approach, EI_{CO} drops sharply by more than an order of magnitude. At approach and above, the combustor becomes sufficiently hot for CO oxidation to proceed nearly to completion, and the remaining operating points cluster near zero. By CR70, C/O and T/O the emission index of CO is essentially negligible, consistent with efficient burnout in the secondary and dilution regions.

Taken together, Figures 6.1 and 6.2 reproduce the classical behaviour of an RQL combustor: high NO_x at high power due to thermal formation in the hot rich and quench zones, and high CO at low power where temperatures are insufficient for complete oxidation. This opposing behaviour of the two pollutants forms an important baseline for interpreting the effect of water injection in Section 6.2.

6.1.2. Temperature evolution

The temperature fields predicted by the CRN provide direct insight into how each zone of the RQL combustor behaves across the operating envelope. Figures 6.3-6.6 summarise the dry-case temperature evolution both as a function of residence time and as a function of discrete stage index.

Across all figures, the same characteristic pattern is observed. The rich primary zone produces the highest temperatures of the entire combustor, followed by a temperature decrease in the quench and lean stages, and a further drop in the dilution region. This behaviour reflects the intended rich-quench-lean sequence of the RQL concept. The blue arrows in the stage-index plots indicate the locations where dilution air is added, and the temperature drops at these points clearly confirm that the mixing model is operating as designed.

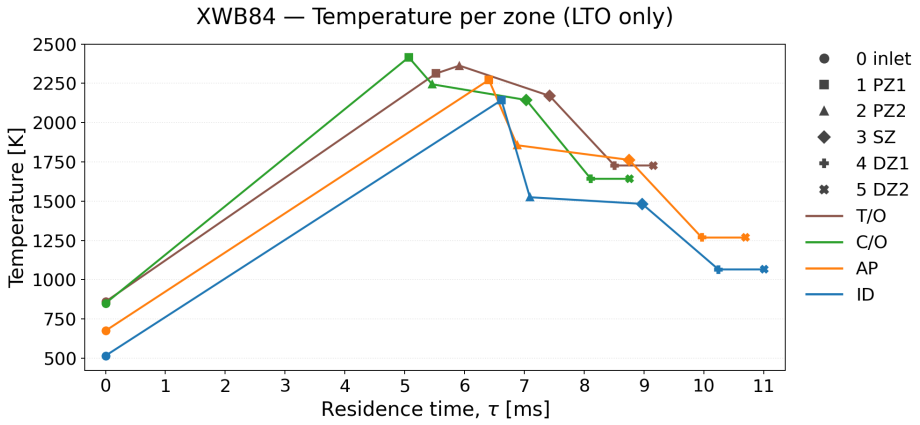

Figure 6.3: Dry case: temperature evolution across zones for all LTO settings.

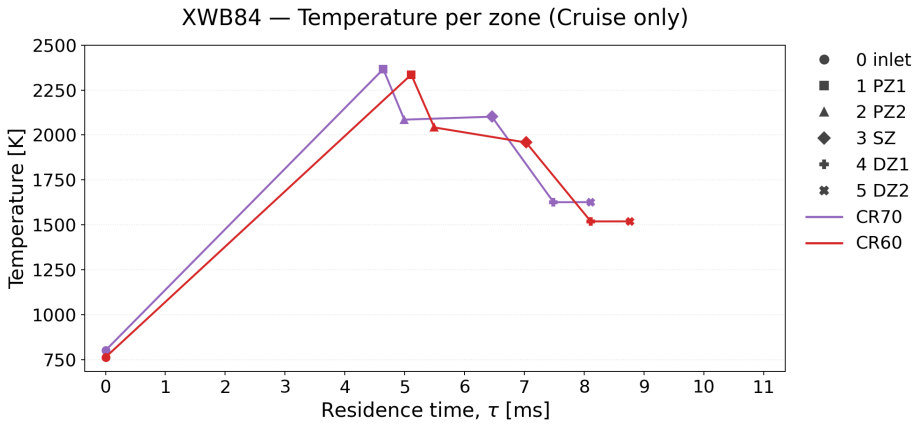

Figure 6.4: Dry case: temperature evolution across zones for the cruise settings.

Figures 6.3 and 6.4 show the temperature development for the LTO and cruise points, plotted against the cumulative residence time through the combustor.

For the LTO settings, the temperature rises steeply from the inlet to the end of the primary zone, where it reaches approximately 2200-$2400\,\mathrm{K}$ depending on the power setting. Take-off and climb-out achieve the highest peak temperatures, consistent with their higher primary-zone equivalence ratios and combustor inlet conditions. The subsequent zones exhibit progressively lower temperatures as secondary and dilution air is admixed. Idle shows the lowest overall temperature profile, peaking near $1400\,\mathrm{K}$ and decreasing rapidly after the quench.

The cruise settings in Figure 6.4 follow the same qualitative behaviour, although the peak temperatures are lower than those at take-off. CR70 exhibits slightly higher temperatures than CR60, as

expected from the corresponding thrust levels. The smooth progression of each curve confirms that the thermochemical evolution across the residence-time coordinate remains physically consistent for all modes.

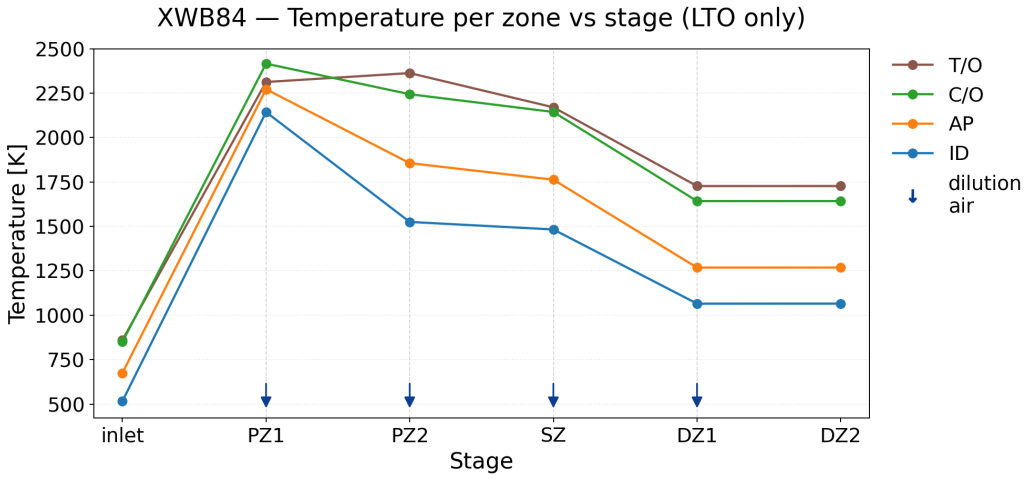

Figure 6.5: Dry case: temperature per stage index for all LTO settings.

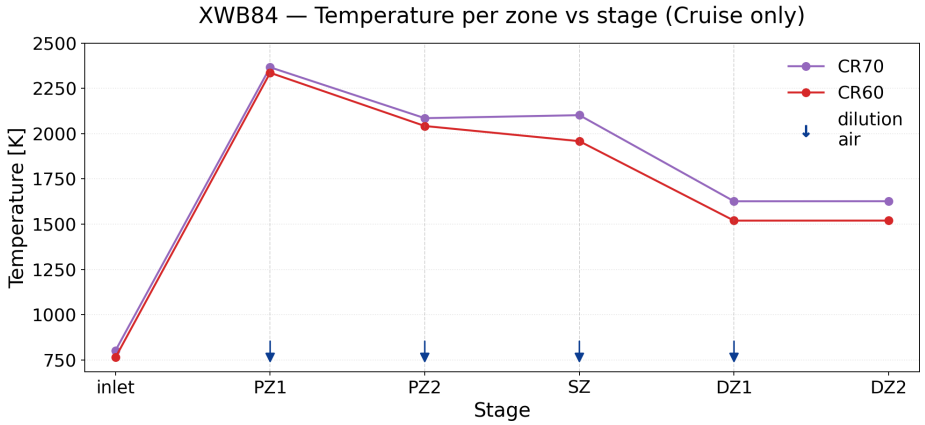

Figure 6.6: Dry case: temperature per stage index for the cruise settings.

Figures 6.5 and 6.6 display the same information as a function of discrete stage index, highlighting the effect of each mixing step. These plots make the influence of dilution air particularly clear. At the transition from the secondary zone to the first dilution zone (SZ $\rightarrow$ DZ1), the temperature decreases abruptly for every operating point. This behaviour occurs at the location indicated by the plotted arrows, confirming that the implementation of staged air addition produces the intended thermodynamic response.

In both the LTO and cruise plots, the primary and quench zones form a high temperature plateau, followed by a gradual decay across the lean and dilution zones. The magnitude of the peak and the steepness of the downstream decline scale directly with power setting. Idle shows the shallowest temperature drop, whereas take-off shows the most pronounced decrease after dilution air is introduced. This reflects the strong temperature dependence of global combustion efficiency at low power and explains the CO trends seen earlier in Figure 6.2.

The slight decrease in PZ1 outlet temperature from C/O to T/O in Figure 6.7 is a consequence of how air and fuel are redistributed at the highest power setting. From ID to C/O, both the local equivalence

ratio and the total mass flow through PZ1 increase, leading to the expected temperature rise. Between C/O and T/O, however, additional air is routed through PZ1 to control the overall combustor equivalence ratio and limit NO_x formation, while part of the extra fuel is burned further downstream in PZ2 and the SZ. The enthalpy flow out of PZ1 still increases, but it is distributed over a larger mass flow and partly shifted to later zones, which produces the small temperature drop at T/O.

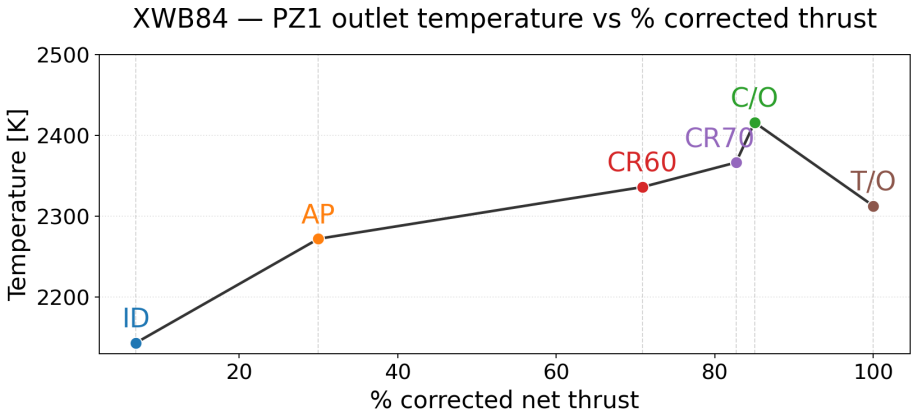

Figure 6.7: Dry case: PZ1 outlet temperature versus corrected net thrust.

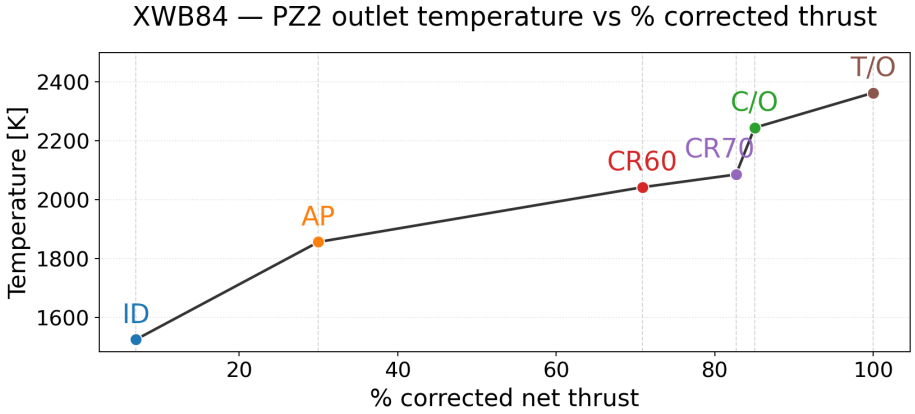

Figure 6.8: Dry case: PZ2 outlet temperature versus corrected net thrust.

Figures 6.7-6.10 show the outlet temperature of each major zone as a function of corrected net thrust. All four zones exhibit smooth, monotonic increases with power setting, but with different sensitivities.

The PZ1 outlet temperature rises from roughly $2150\,\mathrm{K}$ at idle to nearly $2400\,\mathrm{K}$ at climb-out before decreasing slightly at take-off (Figure 6.7). This decrease is a direct consequence of the richer mixture and the strong quenching effect caused by the redistribution of air at the highest power setting. PZ2 follows a similar trend but remains systematically cooler, with temperatures near $1600\,\mathrm{K}$ at idle and approaching $2300\,\mathrm{K}$ at take-off (Figure 6.8).

The secondary zone temperatures in Figure 6.9 lie between those of PZ2 and DZ1 and show a comparatively linear dependence on thrust. This reflects the gradual leaning of the mixture and the controlled addition of secondary air. The DZ1 temperatures (Figure 6.10) are consistently the lowest, ranging from about $1100\,\mathrm{K}$ at idle to $1900\,\mathrm{K}$ at take-off. These temperatures fall into the regime where CO oxidation becomes slow, explaining the high EI_{CO} seen in Figure 6.2 at very low thrust.

Taken together, the outlet-temperature plots highlight that the temperature ordering PZ1 $>$ PZ2 $>$ SZ $>$ DZ1 is preserved across all operating conditions. This ordering plays a central role in shaping the NO_x and CO emission behaviour discussed in Sections 6.1.1 and 6.1.3.

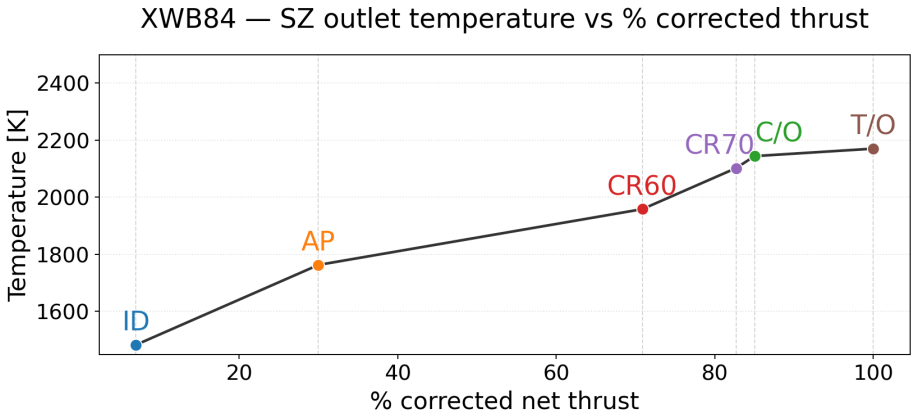

Figure 6.9: Dry case: SZ outlet temperature versus corrected net thrust.

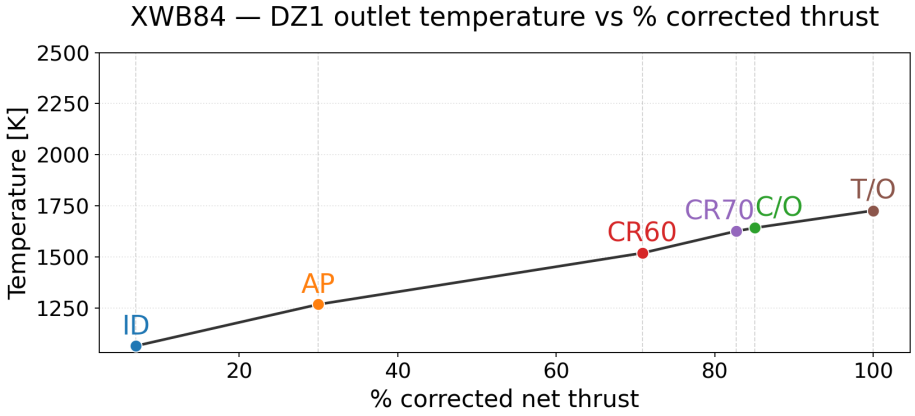

Figure 6.10: Dry case: DZ1 outlet temperature versus corrected net thrust.

6.1.3. Species evolution and NO_x rates per operating mode

The following subsections analyse the thermochemical evolution within each operating mode by examining the temperature history, the major and minor species distributions and the NO_x creation and destruction rates across the RQL combustor. Together, these figures provide a mechanistic explanation for the emission-index trends presented in Section 6.1.1.

Across all modes the same broad features appear. CO_2 and H_2O rise sharply in the primary zone and remain near their equilibrium plateau downstream, CO decreases monotonically as the mixture becomes leaner, and the nitrogen species exhibit a transition from rich-zone fuel-bound intermediates to thermal-NO dominated behaviour in the hot quench and secondary zones. The NO_x rate plots indicate where net formation occurs and where destruction dominates. The relative strength of these processes varies significantly with operating mode due to the strong temperature dependence of thermal NO formation.

Take-off (T/O)

Figure 6.11 shows that the T/O condition reaches the highest temperatures of all operating modes, peaking at approximately $2350\,\mathrm{K}$ near the PZ2-SZ transition. This creates a favourable environment for thermal NO formation.

The major-species profiles in Figure 6.12 are fully consistent with a hot, well-stabilised rich primary zone followed by a lean burnout region. CO_2 and H_2O reach values near their equilibrium plateau as early as PZ2-out and remain nearly constant throughout the rest of the combustor. CO, in contrast,

is highest immediately downstream of PZ1 and decreases continuously across SZ and DZ1, reaching trace levels by the dilution zone due to the high temperature and ample oxidiser availability.

Figure 6.13 shows that NO dominates the nitrogen-species pool, followed by NO_2 and N_2O. NO_2 appears first in the quench zone and increases slightly downstream, while N_2O remains at minor levels. These trends follow naturally from the strong temperature regime in which the Zeldovich mechanism is highly active.

The NO_x rate distribution in Figure 6.14 confirms that the majority of net NO formation occurs in the quench region (PZ2) and early lean zone (SZ). For each operating point the balance between NO_x formation and destruction in the different zones is visualised using bar charts of the volume-specific reaction rates. The bars represent the gross formation, gross destruction and net production rates of NO and NO_2 combined, evaluated from the Cantera `creation_rates`, `destruction_rates` and `net_production_rates` arrays at the converged steady state (units kmol m^{-3} s^{-1}). In PZ1 these rates are first computed for each subzone and then averaged with the corresponding inlet mass flows as weights in order to obtain a single effective rate for the primary rich zone. Downstream, in DZ1 and DZ2, the destruction and creation rates become comparable, leading to near-zero net change. This zone-resolved behaviour directly explains the high EI_{NO_x} at T/O.

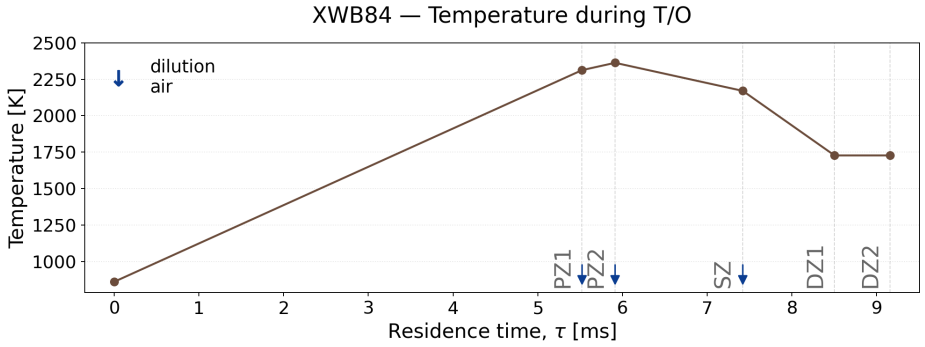

Figure 6.11: Take-off (T/O): temperature evolution across zones.

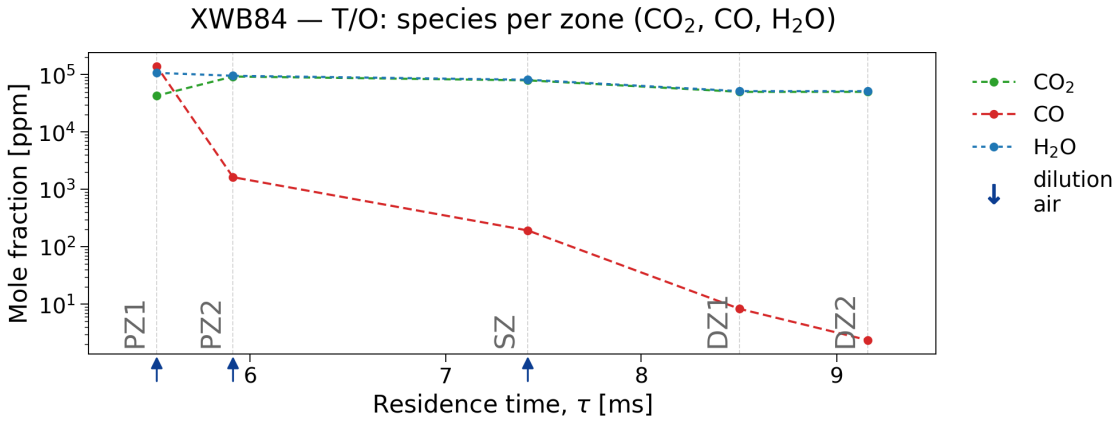

Figure 6.12: Take-off (T/O): CO_2, CO and H_2O mole fractions (log scale).

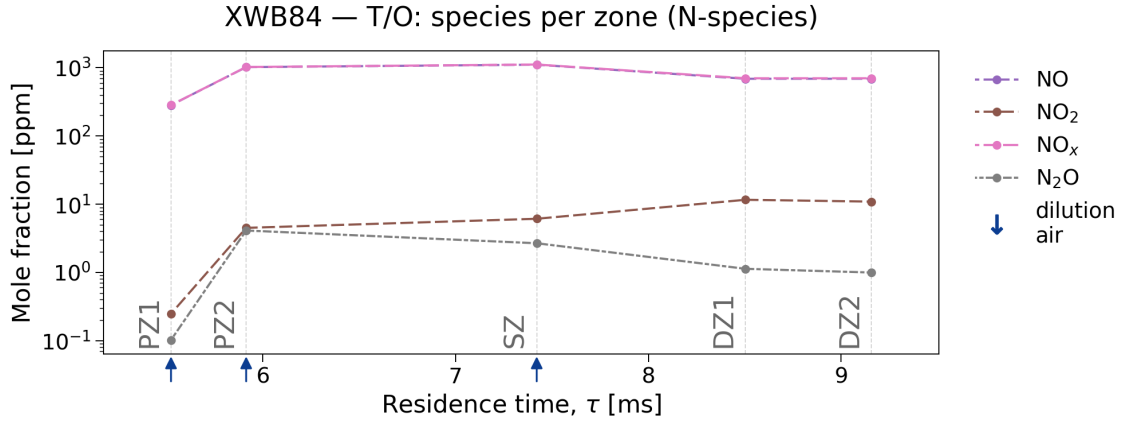

Figure 6.13: Take-off (T/O): nitrogen-containing species (log scale).

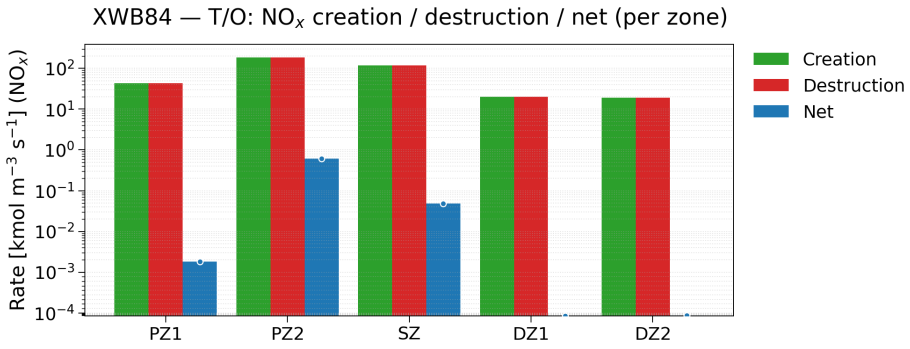

Figure 6.14: Take-off (T/O): NO_x creation, destruction and net rates per zone.

Climb-out (C/O)

The temperature trace in Figure 6.15 remains similar in shape to T/O but with slightly lower peak temperature. As a result, the major species in Figure 6.16 show almost identical trends to T/O, albeit with marginally higher CO levels downstream due to the reduced burnout temperature.

The nitrogen-species profiles in Figure 6.17 continue to show NO as the dominant species, with NO_2 and N_2O at much lower levels. The absolute magnitude of NO is slightly reduced relative to T/O because of the lower peak temperature.

The NO_x rate bars in Figure 6.18 again highlight PZ2 and SZ as the principal formation zones. Both creation and destruction rates are lower than in T/O, consistent with the lower temperatures. The net production remains clearly positive, explaining the still-high (but reduced) EI_{NO_x}.

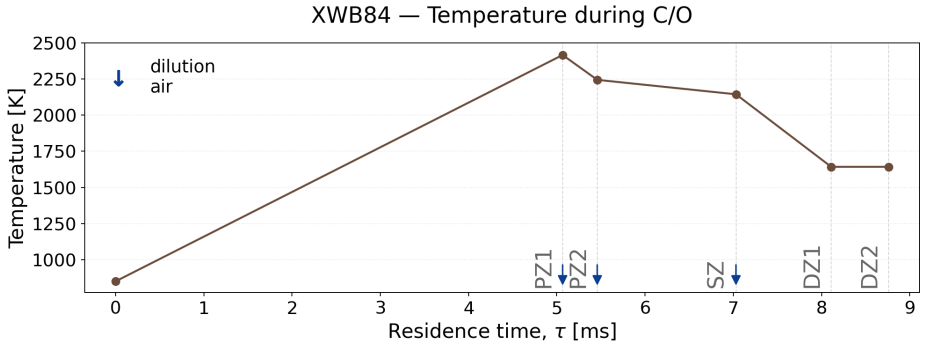

Figure 6.15: Climb-out (C/O): temperature evolution across zones.

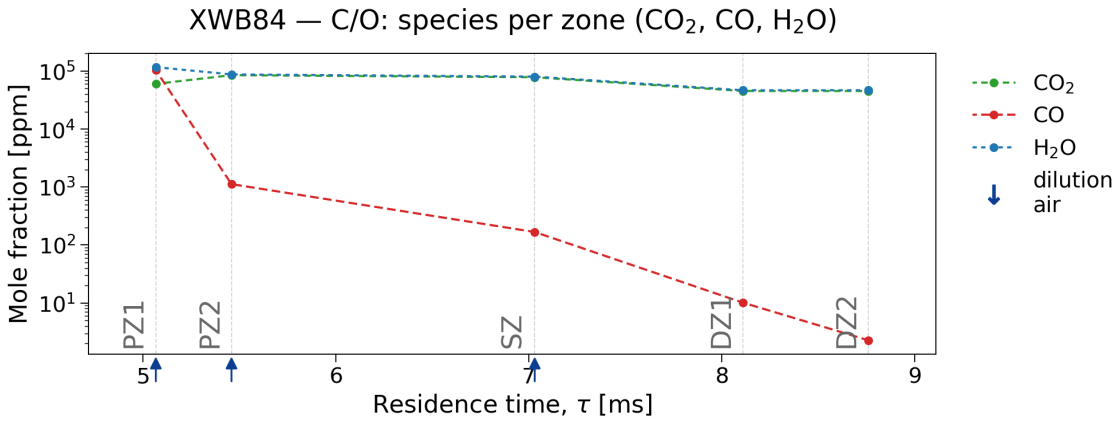

Figure 6.16: Climb-out (C/O): CO_2, CO and H_2O mole fractions (log scale).

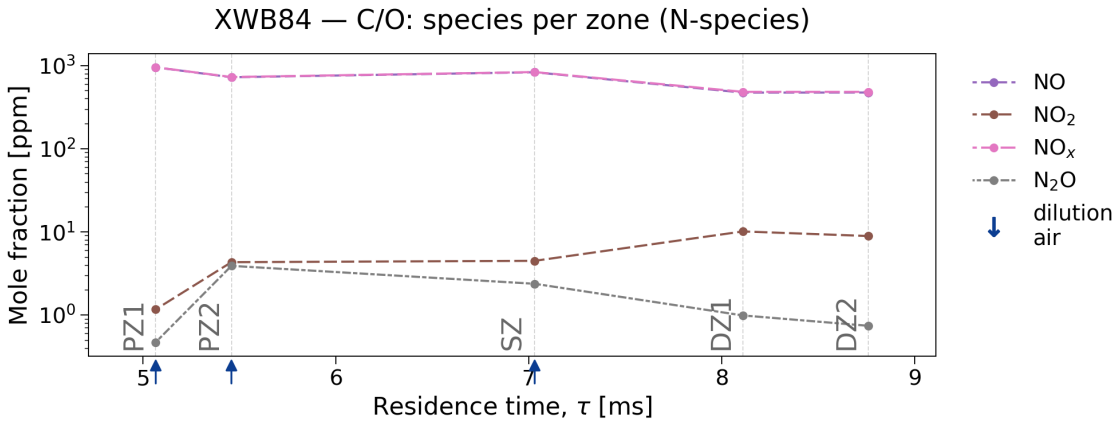

Figure 6.17: Climb-out (C/O): nitrogen-containing species (log scale).

Cruise 70 kN (CR70)

Figure 6.19 shows that CR70 operates at lower temperatures than the LTO modes, but remains in a regime where thermal NO formation is still efficient.

The major-species behaviour in Figure 6.20 matches expectations for moderately lean conditions. CO_2 and H_2O retain a flat profile after PZ2-out, whereas CO falls steadily across the lean zones. Be-

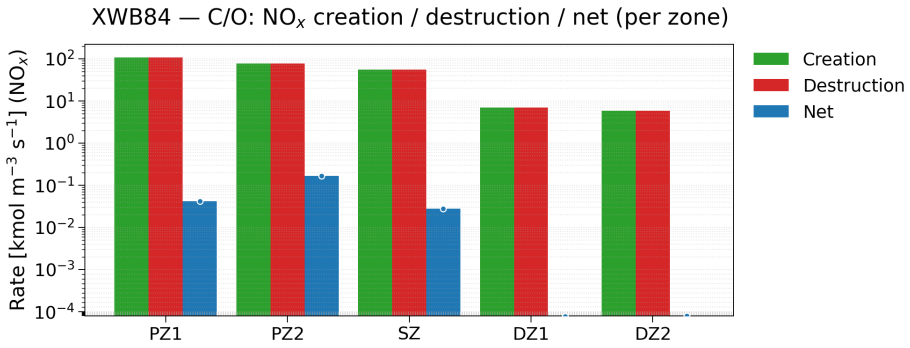

Figure 6.18: Climb-out (C/O): NO_x creation, destruction and net rates per zone.

cause temperatures remain above $1800\,\mathrm{K}$ in SZ, CO continues to oxidise efficiently.

The nitrogen-species trends in Figure 6.21 show a slight reduction in NO relative to T/O and C/O, but still at levels where thermal-NO dominates. NO_2 and N_2O remain minor species, yet the NO_2 fraction increases modestly downstream due to oxidation of NO at cooler, oxygen-rich conditions.

Figure 6.22 confirms that net NO production is concentrated entirely in PZ2 and SZ. In contrast, DZ1 and DZ2 show very small net production, with destruction increasingly competing at the lowest temperatures. This explains why cruise EI_{NO_x} is lower than LTO but still substantial.

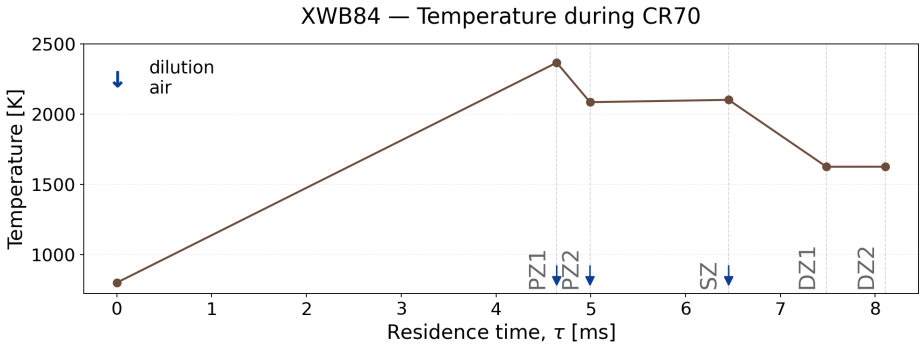

Figure 6.19: Cruise 70 kN (CR70): temperature evolution across zones.

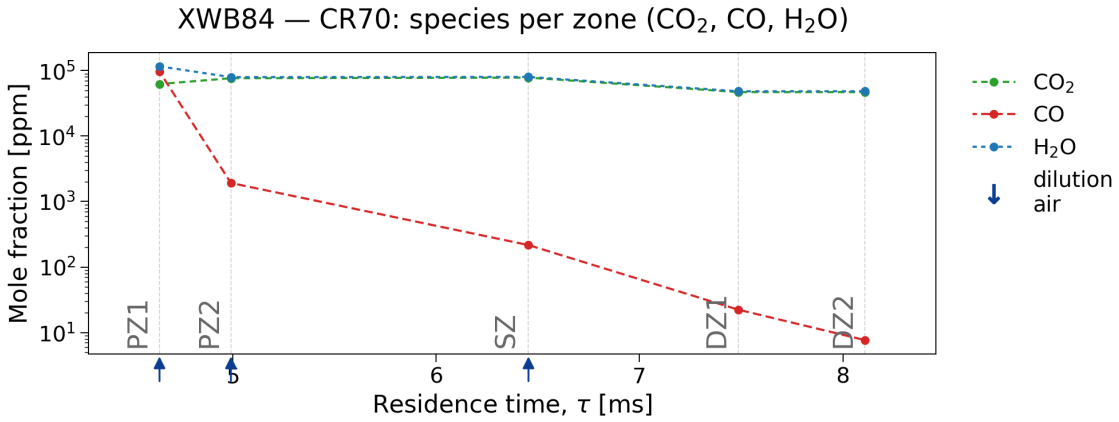

Figure 6.20: Cruise 70 kN (CR70): CO_2, CO and H_2O mole fractions (log scale).

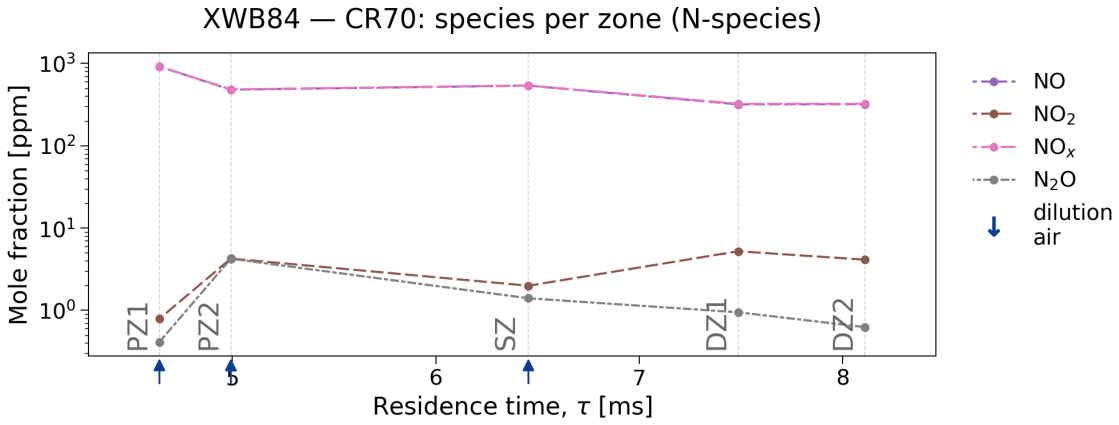

Figure 6.21: Cruise 70 kN (CR70): nitrogen-containing species (log scale).

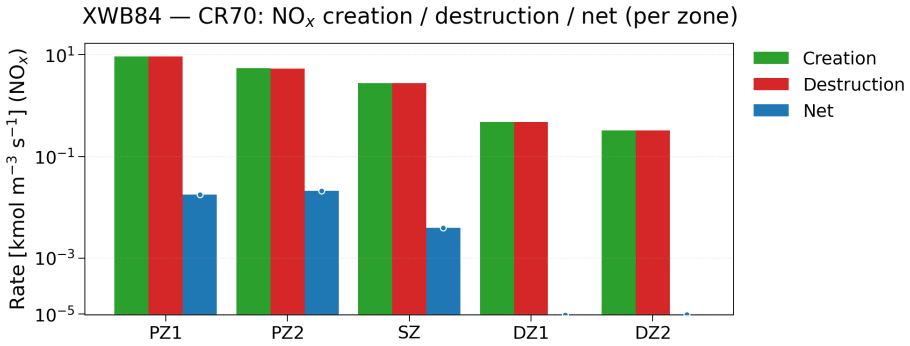

Figure 6.22: Cruise 70 kN (CR70): NO_x creation, destruction and net rates per zone.

Cruise 60 kN (CR60)

The temperature evolution in Figure 6.23 sits slightly below CR70 across all zones, resulting in higher CO levels (Figure 6.24) and correspondingly lower NO levels (Figure 6.25).

The CO decay remains monotonic, confirming that the lean zones still provide sufficient oxidation time. NO remains the dominant nitrogen species, but its magnitude drops compared with CR70 due to

the cooler primary and secondary zones.

The NO_x rate distribution in Figure 6.26 shows a clear reduction in the net formation in PZ2 and SZ, and a noticeable relative increase in destruction in DZ1. The dilution region thus contributes more strongly to net NO reduction than in the higher-power settings.

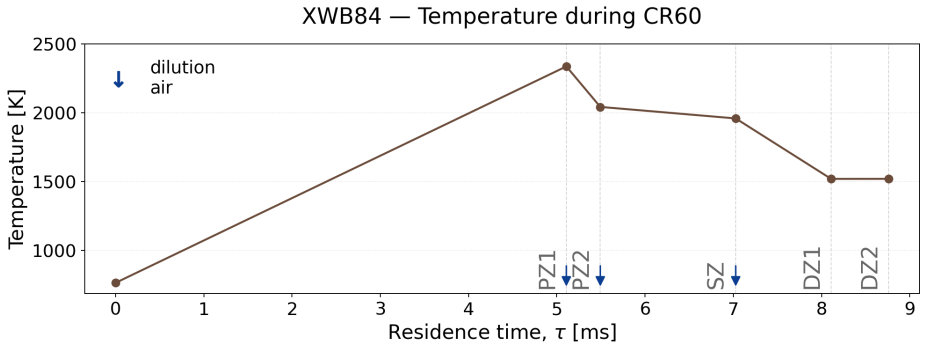

Figure 6.23: Cruise 60 kN (CR60): temperature evolution across zones.

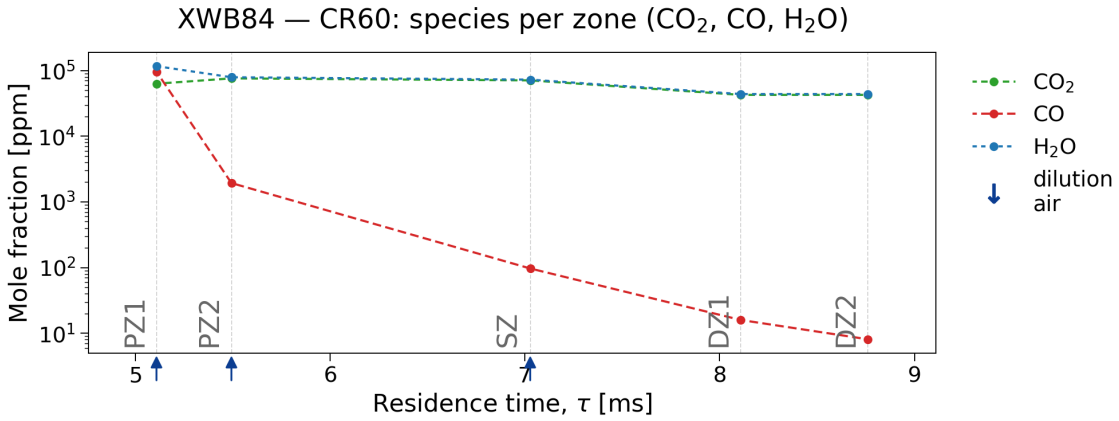

Figure 6.24: Cruise 60 kN (CR60): CO_2, CO and H_2O mole fractions (log scale).

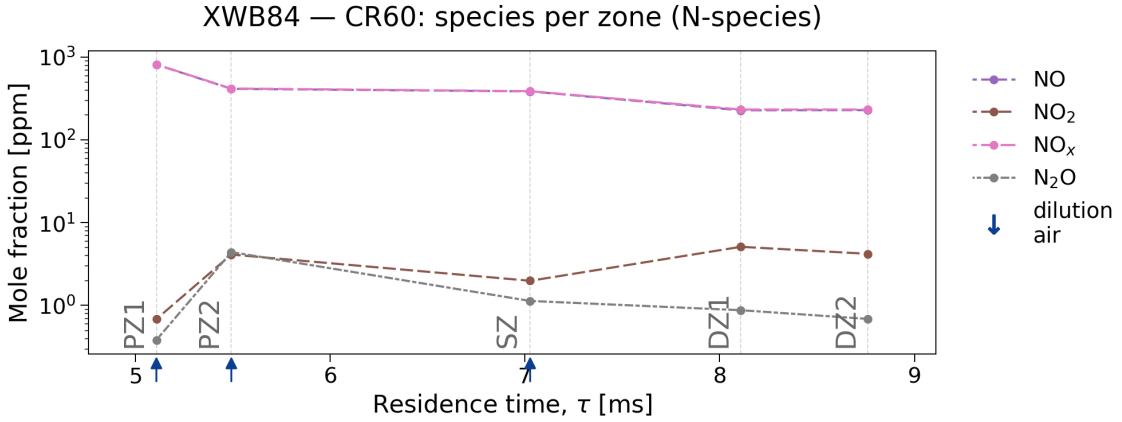

Figure 6.25: Cruise 60 kN (CR60): nitrogen-containing species (log scale).

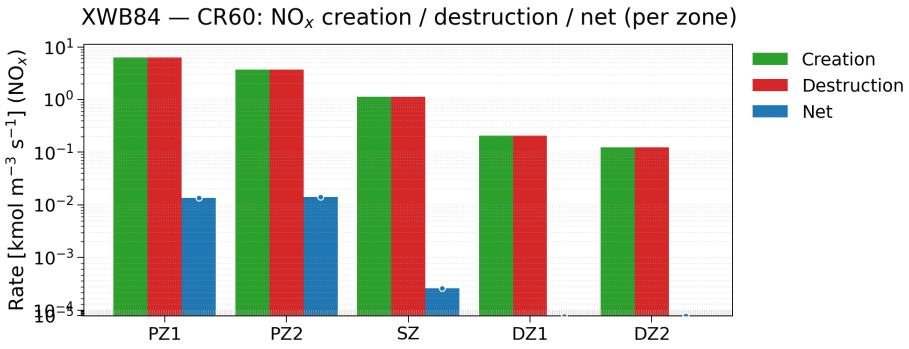

Figure 6.26: Cruise 60 kN (CR60): NO_x creation, destruction and net rates per zone.

Approach (AP)

Figure 6.27 shows that AP operates at substantially lower temperatures than any cruise or climb condition. CO oxidation becomes noticeably less complete, as reflected in the elevated downstream CO levels in Figure 6.28. CO_2 and H_2O remain near a flat plateau, but their values are slightly lower than in cruise due to the overall leaner and cooler combustion.

The nitrogen-species profiles in Figure 6.29 display a marked reduction in NO relative to all higher-power modes. NO_2 begins to recover slightly downstream as temperatures fall and oxidation processes compete with thermal formation.

The NO_x rate bars in Figure 6.30 show a fundamental change: net NO formation in PZ2 is significantly reduced compared to cruise and essentially vanishes in the secondary zone. In DZ1 and DZ2, destruction and creation are of similar magnitude, leading to negligible net change. This behaviour aligns with the observed low EI_{NO_x} at approach.

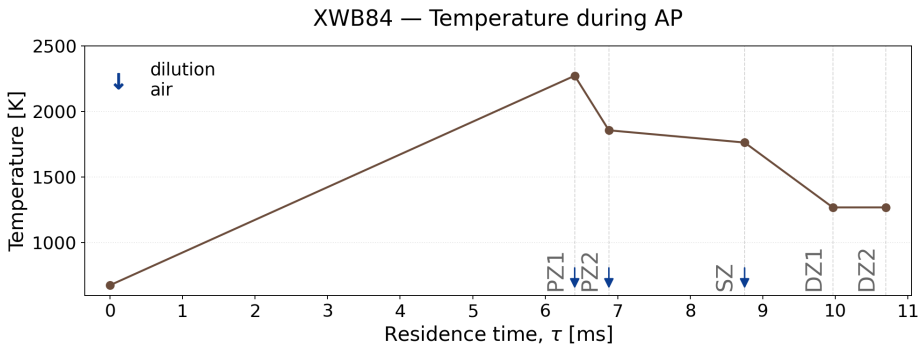

Figure 6.27: Approach (AP): temperature evolution across zones.

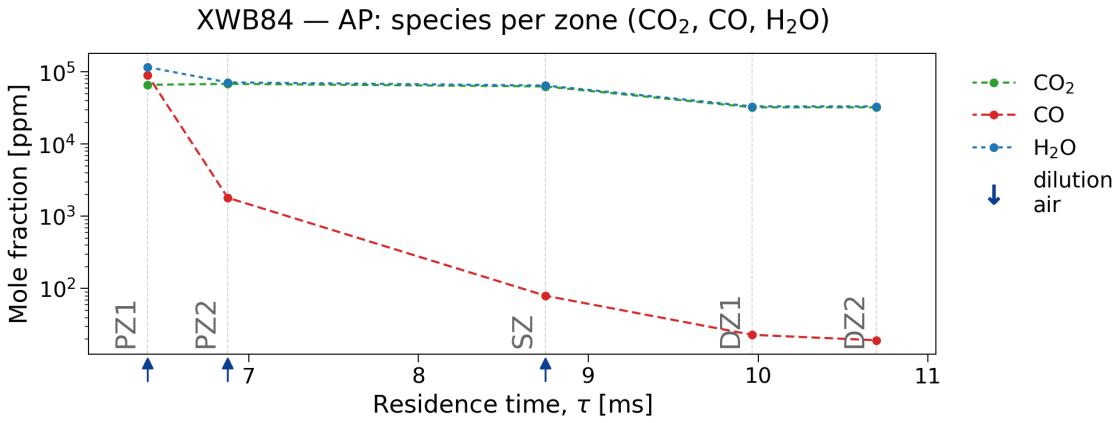

Figure 6.28: Approach (AP): CO_2, CO and H_2O mole fractions (log scale).

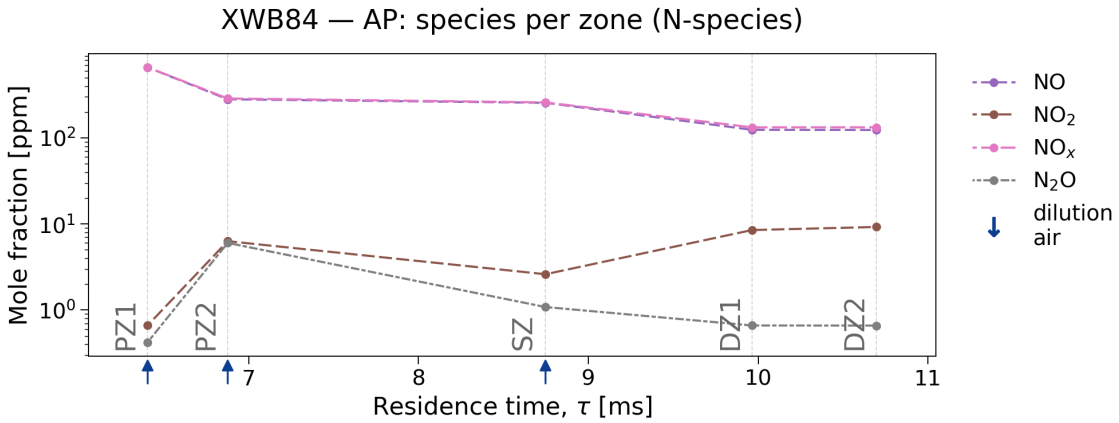

Figure 6.29: Approach (AP): nitrogen-containing species (log scale).

Idle (ID)

The idle temperature profile in Figure 6.31 represents the coldest operating regime of the combustor. CO oxidation is strongly temperature-limited, resulting in the highest CO levels observed in Figure 6.32. CO_2 and H_2O remain qualitatively similar to the other modes, but at lower absolute levels.

The nitrogen-species evolution in Figure 6.33 shows very low NO levels throughout the combustor.

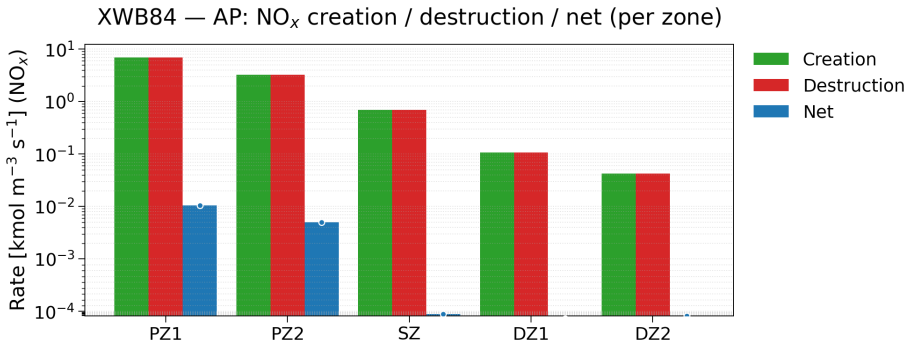

Figure 6.30: Approach (AP): NO_x creation, destruction and net rates per zone.

NO_2 and N_2O remain minor, and the differences between zones are small because thermal formation is suppressed at these temperatures.

The NO_x rate distribution in Figure 6.34 further confirms this. Creation and destruction rates in PZ1 and PZ2 are both orders of magnitude smaller than in cruise or LTO. PZ2 produces a small amount of NO, but this is almost entirely offset by destruction in the secondary and dilution zones. This explains the very low EI_{NO_x} at idle and completes the picture of temperature-controlled NO formation across the operating envelope.

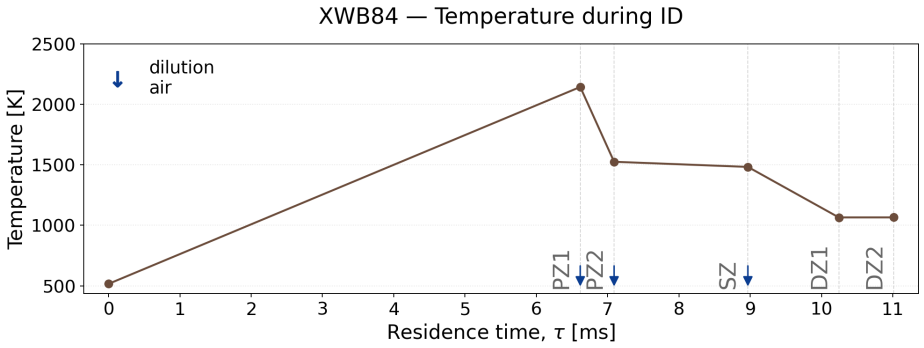

Figure 6.31: Idle (ID): temperature evolution across zones.

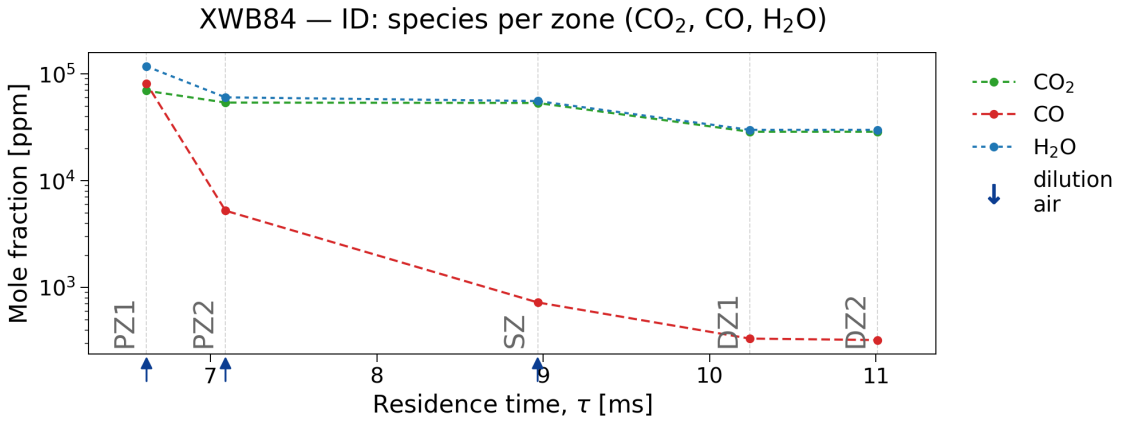

Figure 6.32: Idle (ID): CO_2, CO and H_2O mole fractions (log scale).

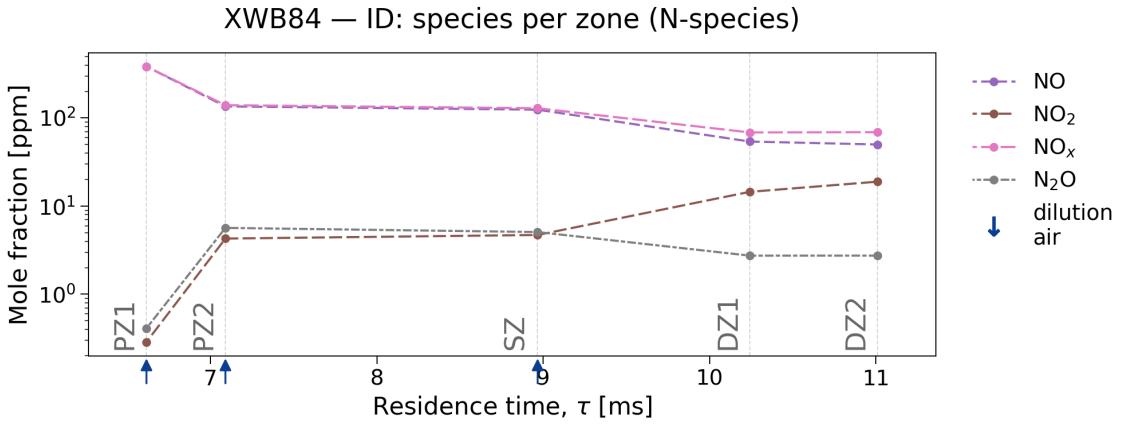

Figure 6.33: Idle (ID): nitrogen-containing species (log scale).

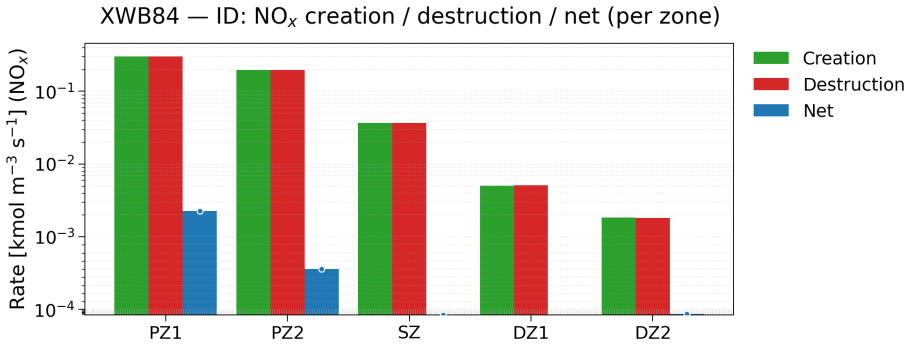

Figure 6.34: Idle (ID): NO_x creation, destruction and net rates per zone.

Summary of species and NO_x behaviour. Across all operating modes, species evolution follows the RQL sequence: rich primary-zone chemistry builds up the CO_2-H_2O pool and generates CO, quench and secondary zones oxidise CO as temperature allows, and the dilution zone governs the final burnout. Nitrogen chemistry is dominated by thermal-NO at high power, transitions to mixed thermal-oxidative behaviour at cruise and approach, and becomes destruction-limited at idle. This zone-resolved inter-

pretation is essential for understanding how water injection affects NO formation, as discussed in the next section.

6.2. Results of the CRN with water injection

This section presents the emission and temperature trends obtained when water is introduced into the chemical-reactor-network model. Only the operating conditions that are meaningful candidates for water injection are considered, namely T/O, C/O, AP, CR70 and CR60. ID is excluded, because water addition during idle operation is neither required nor desirable due to stability concerns and certification irrelevance.

The water-to-fuel ratio is varied from zero (dry case) to 2 $kg_{H_2O}\ kg_{fuel}^{-1}$, which spans the range typically found in experimental demonstrations of combustor water injection. The results are grouped into (i) emission indices, and (ii) temperature modifications in each combustor zone. Together, they clarify both the magnitude of achievable NO_x reduction and the mechanisms by which water influences RQL chemistry.

6.2.1. Emission indices as a function of water addition

Figure 6.35 summarises the behaviour of EI_{CO} and EI_{NO_x} across the water sweep. The trends are consistent with the physics of water-air mixing and the thermal sensitivity of NO formation.

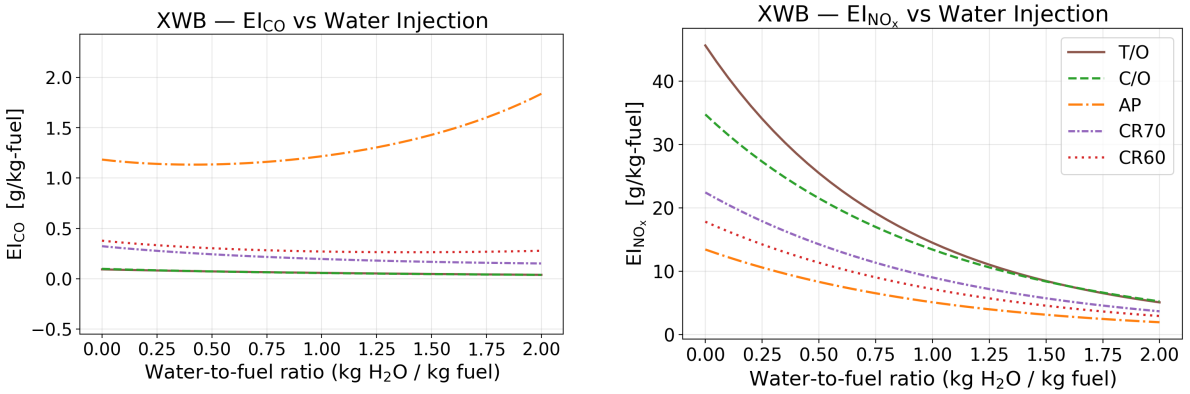

(a) EI_{CO} vs. water-to-fuel ratio.

(b) EI_{NO_x} vs. water-to-fuel ratio.

Figure 6.35: Emission indices of CO and NO_x as a function of the water-to-fuel ratio.

Across all power settings, the introduction of water decreases EI_{NO_x} monotonically. The reduction is largest at high-power settings, where baseline temperatures are highest and thermal NO formation dominates. At 2 kg_{H_2O}/kg_{fuel}, the model predicts reductions exceeding 85% for T/O and C/O, and slightly lower reductions for cruise conditions. This is consistent with the temperature sensitivity of the extended Zeldovich mechanism.

The behaviour of EI_{CO} is more nuanced. For all modes except AP, water causes a mild but systematic increase in CO emissions. This stems from reduced post-flame temperatures, which slow the oxidation of CO to CO_2. Approach (AP) is unique: here EI_{CO} exhibits a shallow minimum at moderate water levels before rising at high water content. This reflects the relatively low temperature margin of AP operation, where small thermal reductions push the secondary and dilution zones closer to the CO-oxidation-limited regime.

To clarify these trends, Figure 6.36 shows the percentage reduction relative to the dry baseline.

The percentage reduction plots highlight the key conclusion: water injection is an extremely effective lever for NO_x control in an RQL architecture, but its effect on CO emissions must be weighed carefully. At cruise powers (CR70 and CR60), the CO penalty remains modest. At take-off, the CO increase is also acceptable, as the combustor remains far above the temperature needed for complete CO

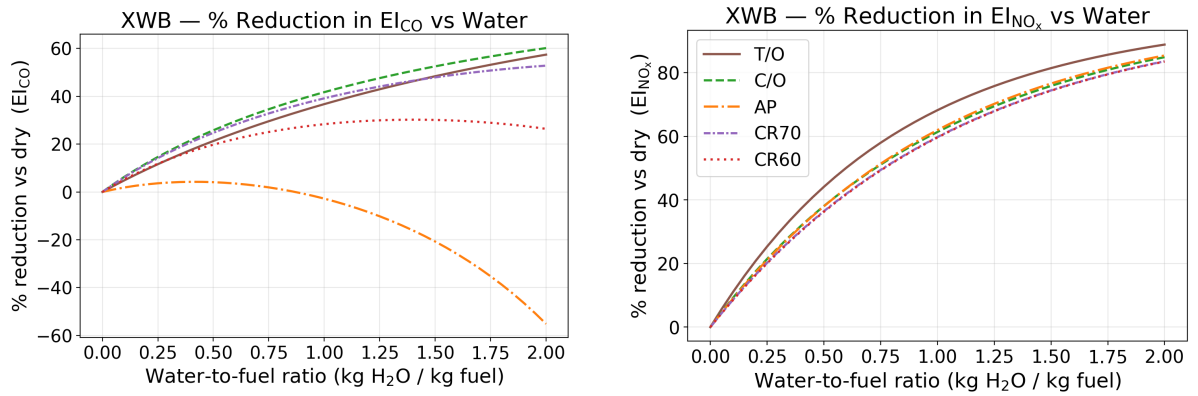

(a) Percentage change in CO emissions.

(b) Percentage reduction in NO_x emissions.

Figure 6.36: Percentage change in CO and NO_x relative to the dry baseline.

oxidation. The most sensitive condition is AP, where CO increases substantially at high water levels, suggesting that water augmentation during approach should be used conservatively.

6.2.2. Temperature reductions in the RQL zones

To connect the emission behaviour with the underlying thermochemical pathways, Figures 6.37-6.38 show the temperature reduction in each RQL zone while increasing the water to fuel ratio.

Primary Zone (PZ1 and PZ2). Water addition lowers temperatures in the rich primary zone at high water-to-fuel ratios. This cooling directly suppresses early-chain thermal NO formation. Since this zone controls the radical pool (O, OH, H), its cooling also reduces the rate of downstream NO formation through the extended Zeldovich mechanism.

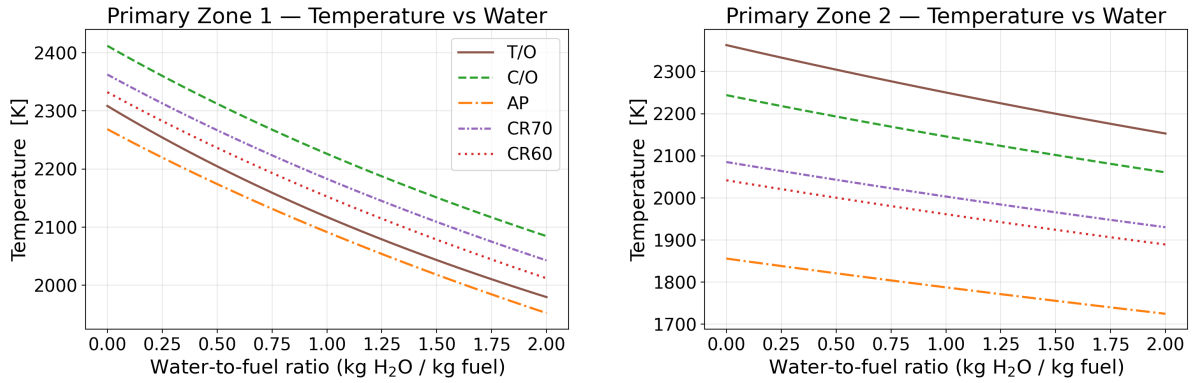

(a) PZ1: outlet temperature.

(b) PZ2: outlet temperature.

Figure 6.37: Temperature reduction in the primary zones as a function of water addition.

Secondary Zone (SZ). The SZ exhibits a nearly linear temperature decrease with water content. This zone is responsible for rapid quenching, and its temperature history controls the conversion of CO and the creation of intermediate NO. The observed reduction explains the systematic CO penalty at AP and CR60.

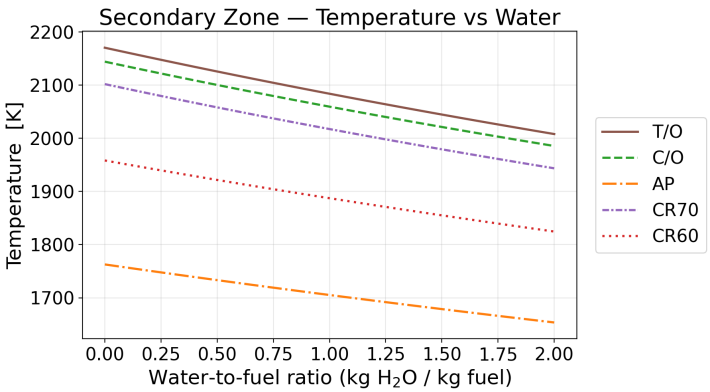

Figure 6.38: Temperature reduction in the secondary zone.

Dilution Zones (DZ1 and DZ2). Temperature reductions in DZ1 and DZ2 are modest but still meaningful. Because NO destruction pathways become increasingly slow at lower temperatures and larger residence times, the reduced temperatures in DZ1/DZ2 lead to a slight weakening of NO reduction capability, causing the net NO removal in these zones to decrease. This further reinforces the importance of suppressing NO formation upstream rather than relying on downstream burnout.

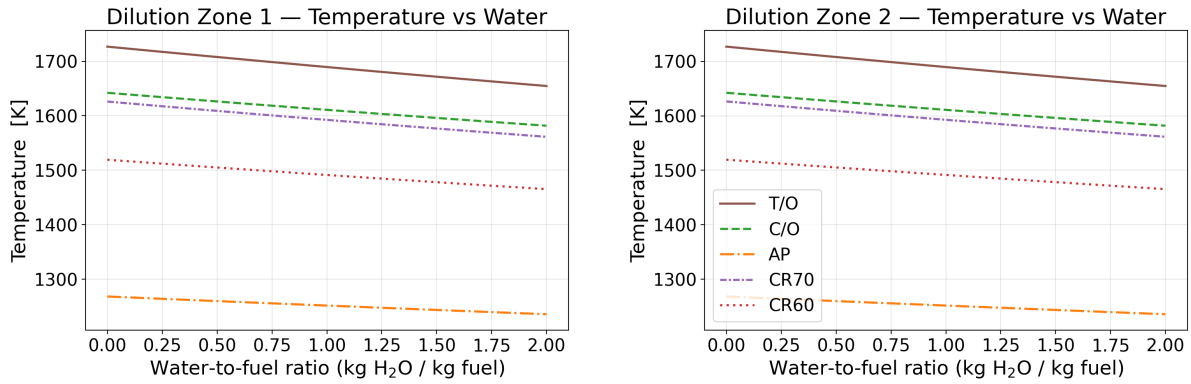

(a) DZ1: outlet temperature.

(b) DZ2: outlet temperature.

Figure 6.39: Temperature reduction in the dilution zones.

6.2.3. Summary of water injection behaviour

Across all operating conditions, water injection primarily reduces NO_x by lowering the temperature in the rich and quench zones, thereby suppressing thermal NO pathways. The magnitude of this reduction is strongly correlated with baseline temperature: the highest-power modes show the largest absolute benefits. CO emissions generally increase with water addition, with AP showing the greatest sensitivity due to already low oxidation temperatures.

These results demonstrate the dual effect of water: strong NO_x mitigation alongside a moderate CO penalty. The balance between these two outcomes determines the operational feasibility of water injection in practice, and the zone-resolved temperature trends provide a physically transparent explanation for the observed emission behaviour.

6.3. Reaction pathways

To complement the global emission indices, reaction-pathway analysis was performed for a single representative operating point. The CR60 condition was selected for this purpose. CR60 corresponds to the 60 kN cruise operating point of the XWB-84 and covers the largest fraction of a typical mission in terms of fuel burn and cumulative emissions. It also lies between take-off and climb in terms of temperature and mixture strength, so it is representative of the regime where both NO_x formation and incomplete CO oxidation are important. All analyses in this section were carried out twice: once for the dry combustor ($w/f = 0.0$) and once for a water-to-fuel mass ratio of $w/f = 1.0$.

The reaction-pathway post-processing is based on the elementary reaction rates provided by Cantera and the stoichiometric coefficients in the Dagaut mechanism. For each zone, the gross formation rate of a target species (CO or NO_x) is decomposed into contributions from predefined reaction families. The plots in this section therefore indicate *how* the modeled network forms and destroys CO and NO_x in each zone, rather than adding new information on the net emission indices themselves.

6.3.1. CO reaction pathways at CR60

Figure 6.40 shows the fractional contributions of three CO-related reaction classes to the gross CO formation rate in each zone. (i) “CO formation” (reactions that purely form CO), (ii) “mixed CO reactions” (reactions that both form and consume CO, such that their net effect can vary with conditions), and (iii) “CO destruction” (reactions that purely consume CO). The fractions in each bar add up to unity, so they provide a normalized measure of the local reaction balance.

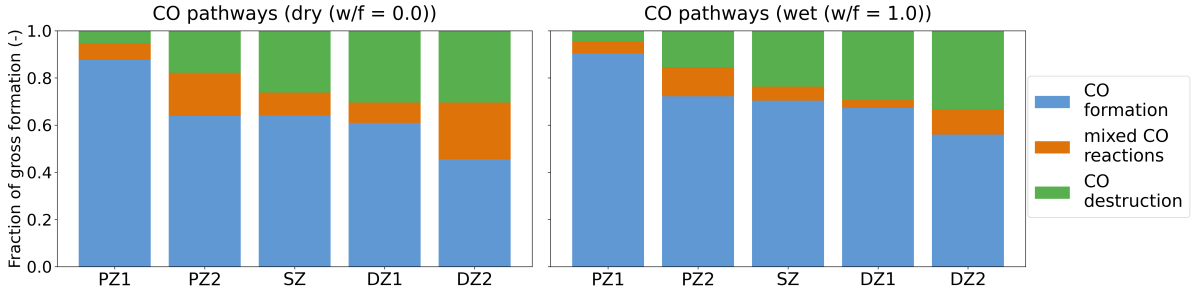

Figure 6.40: CO pathway contributions per zone at CR60. Stacked bars show the fraction of gross CO formation attributed to (i) CO-forming reactions, (ii) mixed CO reactions, and (iii) CO-destroying reactions in each zone.

In the dry case, CO formation dominates the gross production budget in all zones. PZ1 is almost entirely driven by CO-forming reactions, as expected for the rich primary region. Further downstream, the relative contribution of CO destruction increases, especially in SZ and the dilution zones, consistent with the trend towards leaner mixtures and lower CO emission indices at the outlet. Mixed CO reactions account for a modest but non-negligible fraction of the gross formation, particularly in PZ2 and DZ2, indicating that some elementary steps act as bidirectional exchange between CO and its precursors.

With water injection the overall pattern remains the same: CO formation still dominates, while CO destruction becomes most important in the downstream zones. However, the relative importance of mixed CO reactions is slightly reduced in several zones, and the fractional contribution of destruction in DZ2 increases compared with the dry case. These changes are consistent with the broader trends observed in the emission indices: water injection cools the flame and alters the radical pool, but does not fundamentally change the identity of the key CO-forming and CO-destroying pathways at CR60.

The underlying elementary reactions responsible for CO formation are shown in figure 6.41. The horizontal axis lists the ten reactions that contribute most to the *integrated* gross CO formation rate in the whole combustor, numbered 1-10 for ease of reference. The reaction labels give the corresponding stoichiometry; the bars compare the dry ($w/f = 0.0$) and wet ($w/f = 1.0$) cases. Some reactions in the Dagaut mechanism contain the species $CH_2(S)$. The symbol “(S)” denotes the electronically excited *singlet* state of the methylene radical. Both $CH_2(S)$ and the ground-state CH_2 radical participate in CO-forming pathways, with $CH_2(S)$ acting as a short-lived, highly reactive intermediate.

For both dry and wet operation, the ranking of the dominant reactions is almost unchanged. CO production is clearly dominated by the decomposition and oxidation of intermediate species such as HCO, CH_2CO and small radicals (e.g. H and CH). Water injection mainly reduces the absolute rates,

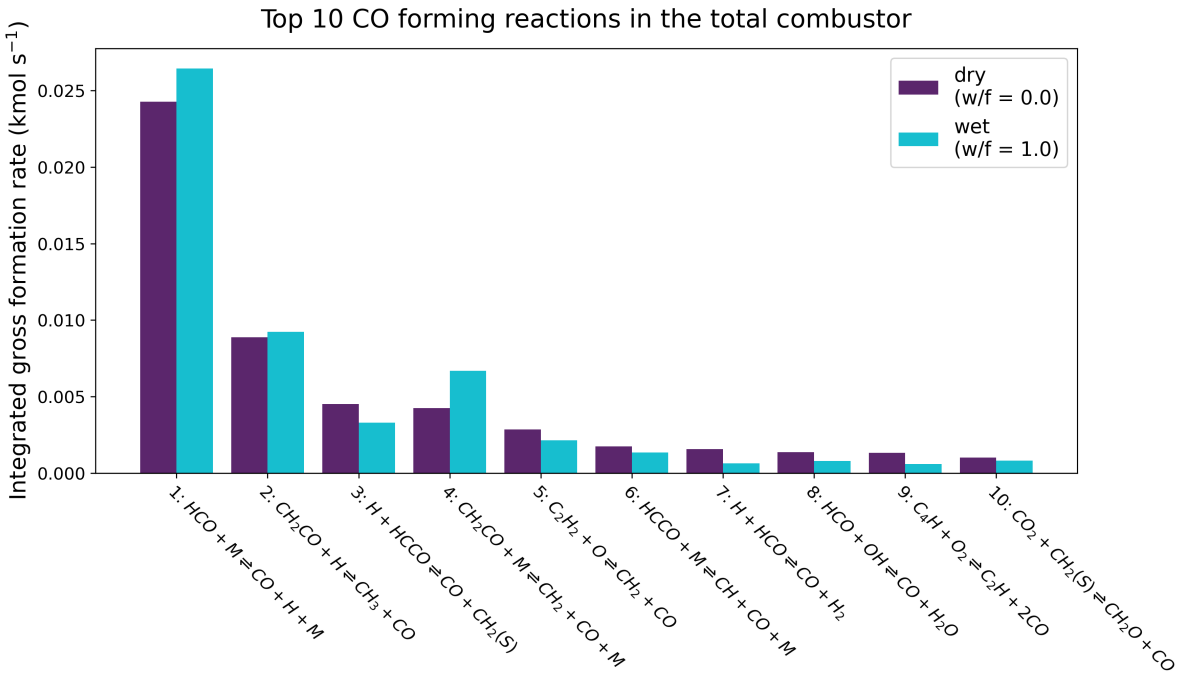

Figure 6.41: Top ten CO-forming reactions in the combustor at CR60. Bars show the integrated gross formation rate of CO (kmol s^{-1}) for the dry and wet cases. Reactions are numbered 1-10 on the horizontal axis; the labels give the full elementary reaction.

with only minor reordering of the weaker contributors. This suggests that, at CR60, the influence of water on CO emissions acts primarily through temperature and radical concentration changes within an otherwise similar reaction network, rather than by activating qualitatively different CO pathways. A more detailed interpretation of these trends is deferred to the discussion chapter.

6.3.2. NO_x reaction pathways at CR60

An analogous decomposition was applied to NO_x formation. In this work, the gross formation of NO and NO_2 is grouped into six classes:

- **Reduced-N cycle** groups all reactions that temporarily convert NO into HCN, HNO, or NH_x intermediates and back again; in a fuel without bound nitrogen this represents NO $\rightarrow$ NH_x $\rightarrow$ NO looping rather than oxidation of fuel-N.
- **N_2O path** contains reactions that form or consume N_2O as an intermediate (e.g. N_2O + H/O $\rightarrow$ NO).
- **Other NO_x routes** includes the remaining minor steps that interconvert NO, NO_2, NO_3, HO_2NO, and related species but do not belong to the classical mechanisms.
- **Prompt NO** contains Fenimore-type reactions where hydrocarbon radicals (CH, C_2H, etc.) attack N_2 to produce HCN.
- **Reburn** includes reactions that consume NO through CO, HCN, or NH_x (e.g. NO + NH_2 $\rightarrow$ N_2 + H_2O).
- **Thermal NO** corresponds to the extended Zeldovich sequence N_2 + O $\rightarrow$ NO + N, N + O_2 $\rightarrow$ NO + O, and N + OH $\rightarrow$ NO + H.

Figure 6.42 displays the fractional contributions of these six classes to the gross NO_x formation rate in each zone.

In the dry case, the reduced-N cycle and thermal NO dominate the gross NO_x formation in PZ1-SZ. PZ1 and PZ2 are particularly influenced by the reduced-N cycle, with thermal NO providing the main competing contribution. The N_2O path and prompt NO (through hydrocarbon radicals) account for a smaller, but still visible, fraction in PZ2 and SZ, while reburn acts as a minor NO-reduction channel. Further downstream, in DZ1 and DZ2, the “other NO_x routes” category becomes dominant. This reflects

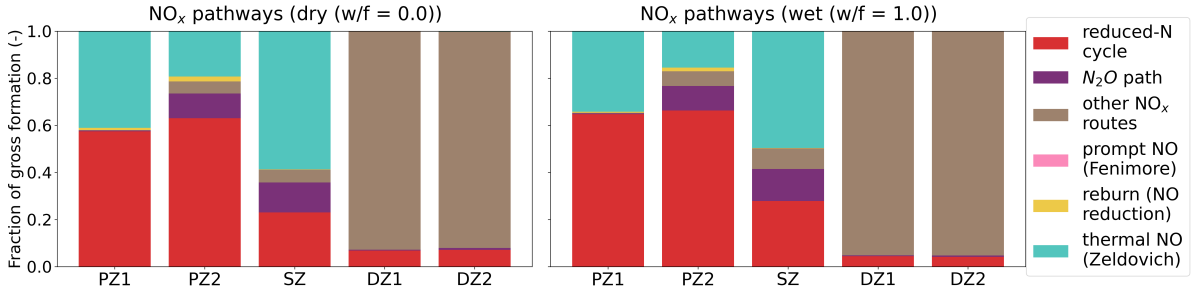

Figure 6.42: NO_x pathway contributions per zone at CR60. Stacked bars show the fraction of gross NO_x formation attributed to the reduced-N cycle, the N_2O path, other NO_x routes, prompt NO, reburn reactions and thermal NO (Zeldovich).

the fact that the lower-temperature, lean-dilution environment is less well captured by the classical thermal or prompt NO pictures and involves a broader mixture of minor reactions.

Water injection retains this overall structure but modifies the balance between the classes. The fractional contribution of the reduced-N cycle increases in PZ1-SZ, while the thermal NO fraction tends to decrease. In the dilution zones the gross formation is still dominated by the "other NO_x routes" class, consistent with the idea that water primarily affects the high-temperature core of the combustor. Again, these observations only describe how the modeled NO_x budget is redistributed between pathways under wet operation; a detailed assessment of whether this is desirable or robust will be made in the discussion chapter.

The elementary reactions that contribute most to gross NO_x formation in the whole combustor are summarised in figure 6.43. As for CO, the ten reactions with the largest integrated gross NO_x formation rate are shown, with dry and wet bars plotted side by side for each reaction index.

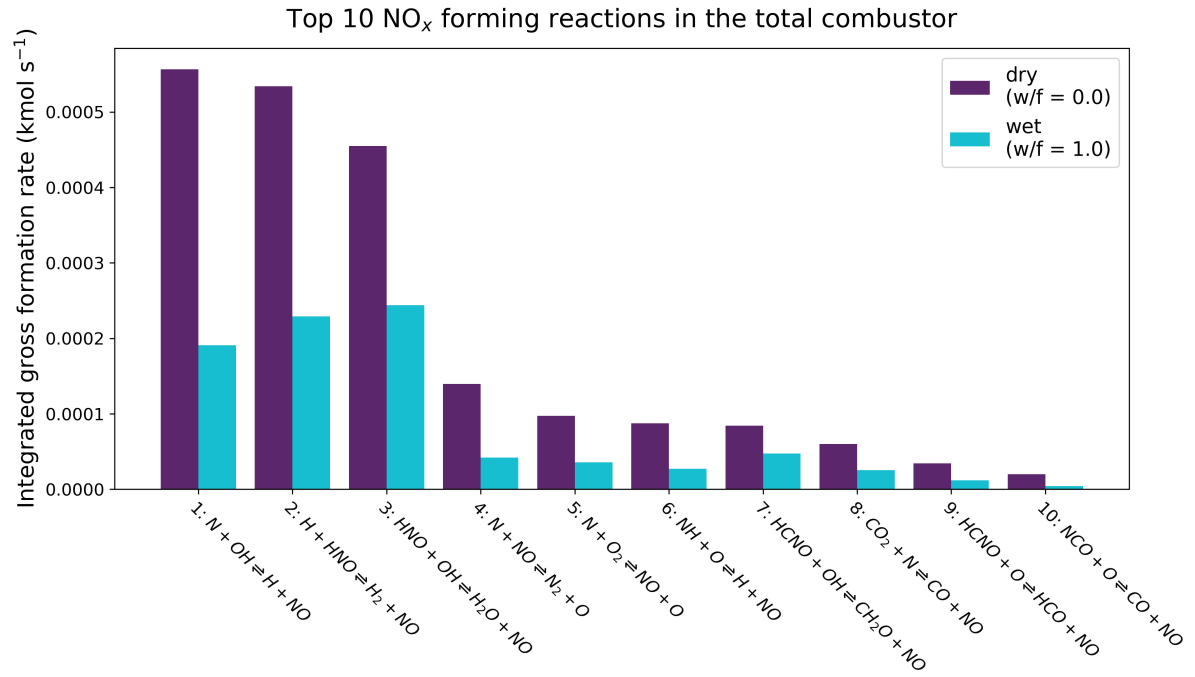

Figure 6.43: Top ten NO_x-forming reactions in the combustor at CR60. Bars show the integrated gross formation rate of NO_x (kmol s^{-1}) for the dry and wet cases. Reactions are numbered 1-10 on the horizontal axis; the labels give the full elementary reaction.

The leading reactions are all familiar high-temperature NO formation and interconversion steps, involving N, O, HNO and related radicals. Water injection reduces the absolute formation rates of almost all of these reactions, with some redistribution between them but no dramatic change in identity. This is consistent with the notion that water primarily damps the thermal and radical-driven components

of NO_x chemistry through cooling and dilution, while leaving the qualitative reaction network largely unchanged at CR60.

Overall, the reaction-pathway analysis confirms that the modeled changes in CO and NO_x emissions between dry and wet operation at CR60 arise from shifts within the same underlying reaction families, rather than from fundamentally new pathways. The implications of this for the robustness of water injection as an emissions-mitigation strategy will be examined in the subsequent discussion chapter.

7

Discussion

This chapter reflects on the behaviour of the CRN model and examines how well it explains the emission trends of an RQL combustor in both dry and water-injected operation. It also compares the CRN predictions to simpler engineering correlations and considers the model's performance at cruise.

The dry simulations follow the expected behaviour of an RQL combustor. NO_x increases with thrust because higher temperatures and richer primary-zone mixtures strengthen the thermal NO pathways. CO shows the opposite trend: it is highest at idle, where low temperatures limit oxidation rates, and it becomes almost negligible at higher thrust when the lean zones are sufficiently hot for complete burnout. These behaviours align with the validated CF6 and XWB results and indicate that the CRN captures the key roles of temperature, stoichiometry and residence time in setting NO_x and CO levels.

When comparing the CRN to correlation-based methods such as P3T3 and BFFM2, it is clear that the CRN is not a replacement for these models. They remain effective within the ICAO LTO range and require far less input data. In certain low-thrust cases, BFFM2 even reproduces CO more closely than the CRN. However, the correlations provide no information about the internal combustor processes that generate emissions. In contrast, the CRN resolves how emissions depend on local mixture variations, temperature distributions and reaction pathways. It also reproduces the idle CO peak that P3T3 cannot capture. Furthermore, the CRN predicts high-thrust NO_x with accuracy similar to BFFM2, while offering the advantage of being directly applicable at cruise without empirical extrapolation. Furthermore, the CRN predicts high-thrust NO_x with accuracy similar to BFFM2, while remaining applicable at cruise through a physically constrained optimisation of the mixture parameters under cruise boundary conditions. At cruise, P3T3 slightly overpredicts NO_x, while BFFM2 lies within the measured inflight range but, unlike the CRN, cannot resolve the internal mixture structure or reaction pathways.

The simulations with water injection show a consistent reduction in NO_x across all operating points, with the strongest reductions at high thrust where thermal NO production is most sensitive to temperature. The mechanism is fully consistent with theory: injected water lowers flame temperature and reduces the radical pool in the near-stoichiometric regions, directly weakening the thermal NO pathways. CO behaviour depends strongly on operating condition. At idle and approach, where temperatures are already low, further cooling slows CO oxidation and increases CO. At high thrust, CO is only mildly affected because temperatures remain high enough for nearly complete burnout. The CRN therefore reveals a clear NO_x-CO trade-off that depends on thrust level rather than on water loading alone.

The reaction-pathway analysis for CR60 confirms that water injection does not alter the qualitative structure of either the nitrogen or carbon reaction networks. The same thermal NO routes dominate in both wet and dry cases. Water simply slows these pathways by lowering temperature and reducing key radicals such as O, OH and H. Non-thermal contributions grow in relative importance only because the thermal channel weakens, not because new mechanisms appear. CO oxidation proceeds through the same intermediates, only at a slower rate. This consistency indicates that the CRN behaves in line with established combustion theory and with known characteristics of water-diluted flames.

Finally, the CRN predictions at cruise show NO_x values within the range of available inflight measurements for the XWB. This is encouraging, as no model retuning was performed for cruise. The same primary-zone structure, residence-time formulation and mixing model are retained, while the mixture parameters are re-optimised under cruise boundary conditions. While additional flight data and more

detailed combustor information would help reduce uncertainty, the agreement suggests that the CRN captures the dominant chemistry and mixing processes at cruise more accurately than the correlation methods. This supports the conclusion that chemically detailed, low-order models can provide reliable cruise predictions and offer insight into combustor modifications such as water injection that lie outside the scope of empirical correlations.

8

Conclusions

This thesis developed a detailed CRN model for an RQL combustor, validated it against two reference engines, and applied it to study water injection, reaction pathways and cruise emissions. The three subquestions together lead to the final answer to the main research question.

Subquestion 1: How can predictive modelling be extended to cruise despite limited data?

Cruise conditions were modelled directly by supplying cruise-specific inlet temperatures, pressures and mass flows to the CRN. The combustor geometry and primary-zone structure remained the same as in the validated take-off case. Because the CRN resolves zone-wise chemistry, this approach does not require empirical scaling of cruise conditions. The resulting cruise NO_x predictions for the XWB fall within the range of available inflight measurements. This shows that a validated CRN can be reliably used at cruise when the physical inputs are available.

Relative to correlation-based approaches, the P3T3 method and the Boeing Fuel Flow Method 2 (BFFM2) provide a useful but more limited baseline. Once calibrated on the LTO modes, BFFM2 reproduces EI_{NO_x} reasonably well but shows larger deviations for CO, especially at approach and idle, while P3T3 overpredicts low-power NO_x and cannot capture the idle CO peak. At cruise both correlations yield NO_x values of the correct order of magnitude, with BFFM2 lying within and P3T3 close to the measured in-flight range, but neither provides any information on local mixture structure or on the effects of water injection. The CRN therefore complements rather than replaces these methods: it retains their ability to match LTO emissions but extends predictive capability to cruise and to modified combustor physics.

Subquestion 2: What is the extent of NO_x reduction achievable with water injection?

Water injection consistently reduces NO_x at all operating points. The strongest reductions occur at high thrust, where thermal NO is highest and the temperature drop caused by water has the largest effect. At low thrust the reductions are smaller because the baseline NO_x levels are already low. CO increases at idle and approach due to reduced burnout temperatures, while the impact at high thrust is modest. The overall extent of NO_x reduction therefore depends on thrust, water fraction and acceptable CO levels.

Subquestion 3: What are the dominant pathways under water-injected conditions?

The main NO_x pathways do not change when water is added. The thermal NO pathway remains dominant in both dry and wet cases. Water lowers temperature and reduces O, H and OH radicals, slowing the same reactions rather than creating new ones. CO oxidation follows the same chain of

intermediates under wet conditions, only at a slower rate. The chemistry remains structurally the same.

Main Research Question: What is the effect of water injection on NO_x emissions in an aero-engine combustor across operating conditions?

Water injection lowers NO_x reliably across the operating envelope by cooling the flame and reducing the radical pool that drives thermal NO formation. The effect is strongest at high thrust, where near-stoichiometric subzones dominate NO_x production. At lower thrust the reductions are smaller and come with CO penalties due to cooler lean zones. Because the CRN can predict these effects at both LTO and cruise without per-condition tuning, it provides a clear and physically grounded explanation of how water injection changes NO_x behaviour in an RQL combustor.

Overall contributions

- A detailed CRN with parallel primary-zone subzones was developed and validated for two turbofan engines.
- The same CRN was used at cruise by providing cruise-specific inlet conditions, producing predictions consistent with available flight data.
- Water injection was quantified across operating points, revealing predictable NO_x reductions and CO trade-offs.
- Reaction-pathway analysis confirmed that water suppresses existing thermal-NO pathways without introducing new chemistry.

Together, these results show that CRN modelling is a powerful and transparent way to study water injection and to predict low-emission behaviour beyond standard LTO conditions.

9 Recommendations

The CRN built in this thesis provides a good basis for studying RQL emissions and water injection. Several improvements and follow-up steps can make the model more reliable and more useful in future work.

9.1. Model improvements

- **Mixing representation.** The current unmixedness parameter s is a simple way to describe how well the primary zone is mixed. In reality this mixing depends on swirl, jet penetration and local recirculation. If future work includes even basic flow information from CFD or experiments, s could be linked more directly to the actual flow and become less of a "free" parameter.
- **Different chemistry models.** The Dagaut mechanism works well for this study, but there are newer kerosene mechanisms with updated nitrogen chemistry. Comparing several mechanisms would show how sensitive the NO_x predictions are to the chemical model, especially with water present.
- **More pollutants.** The current CRN only looks at NO_x, CO and hydrocarbon emissions. Adding soot or sulphur chemistry in the future would allow a more complete environmental analysis of water injection.

9.2. Additional validation

- **Water injection tests.** Dedicated experiments with controlled water addition would be very valuable. They would allow a direct check of the modelled NO_x and CO reductions and help improve the way water is added inside the CRN.
- **More cruise data.** Cruise validation currently relies on a limited set of XWB measurements. More inflight data, ideally from different engines, would help confirm whether the CRN remains predictive at off-design conditions.
- **Better combustor information.** Many CRN inputs, such as air splits and volumes, come from public sources or literature and these are limited. Having access to more detailed geometry or flow information would reduce uncertainty and improve calibration.

9.3. Future applications

- **Design studies.** The CRN can be used inside an optimisation loop to explore alternative air splits, primary-zone distributions or water-injection schedules. This would help find strategies that reduce NO_x while keeping CO within limits.
- **Other combustor concepts.** The same modelling approach can be adapted to other combustor types, such as LDI or staged-lean designs. This would make it possible to compare how water injection performs across different architectures.
- **Mission-level analysis.** Linking the CRN with aircraft performance tools would allow the effect of water injection to be evaluated over a full flight, including the added mass of water and the operational penalties or benefits.

In summary, the CRN developed in this thesis forms a solid foundation for future studies on low-emission combustor strategies. With better data, improved mixing models and broader pollutant coverage, it can become a practical tool for design and assessment of next-generation engines.

References

[1] A. Huang, *A close-up of a jet engine on a table*, Photograph posted on Unsplash, Accessed: 2025-12-03. [Online]. Available: https://unsplash.com/photos/a-close-up-of-a-jet-engine-on-a-table-Qqr8dwAjqzw.

[2] D. S. Lee, D. W. Fahey, P. M. Forster, *et al.*, "The contribution of global aviation to anthropogenic climate forcing for 2000 to 2018," *Atmospheric Environment*, vol. 244, p. 117 834, 2021. DOI: 10.1016/j.atmosenv.2020.117834.

[3] J. H. Seinfeld and S. N. Pandis, *Atmospheric Chemistry and Physics: From Air Pollution to Climate Change*, 3rd ed. John Wiley & Sons, 2016, ISBN: 9781118947401.

[4] D. S. Stevenson, F. J. Dentener, W. J. Collins, R. G. Derwent, M. G. Schultz, *et al.*, "Multimodel ensemble simulations of present-day and near-future tropospheric ozone," *Journal of Geophysical Research: Atmospheres*, vol. 111, no. D8, p. D08301, 2006. DOI: 10.1029/2005JD006338.

[5] A. H. Lefebvre and D. R. Ballal, *Gas Turbine Combustion: Alternative Fuels and Emissions*, 3rd ed. CRC Press, 2010, ISBN: 9781420071823.

[6] S. M. Correa, "A review of nox formation under gas-turbine combustion conditions," *Combustion Science & Technology*, vol. 87, no. 1-6, pp. 329–362, 1993. DOI: 10.1080/00102209208947221.

[7] S. R. Turns, *An Introduction to Combustion: Concepts and Applications*, 3rd ed. McGraw-Hill, 2012, ISBN: 9780073380193.

[8] T. Telidevara, "Numerical simulation of emissions in rich-quench-lean (rql) combustors," MSc thesis, Delft University of Technology, Delft, The Netherlands, 2015.

[9] S. Saxena and F. A. Williams, "Enhancement of nox reduction in combustion by water and steam injection: A review," *Combustion Science and Technology*, vol. 178, no. 2, pp. 371–384, 2006. DOI: 10.1080/00102200500293848.

[10] N. R. Marchionna, L. A. Diehl, and A. M. Trout, "Effect of water injection on nitric oxide emissions of a gas-turbine combustor burning astm jet-a fuel," NASA Lewis Research Center, Tech. Rep. NASA TM X-2958, 1973.

[11] M. Farokhipour, J. A. Esfahani, and E. Amini, "Effects of fuel and water injection on nox formation in gas turbine combustors," *Fuel*, vol. 230, pp. 377–388, 2018. DOI: 10.1016/j.fuel.2018.06.031.

[12] C. H. Wey, B. Anderson, F. Blinzler, *et al.*, "Overview on the aircraft particle emissions experiment (apex)," NASA Glenn Research Center, Tech. Rep. NASA TM-2006-214382, 2006.

[13] T. Poinsot and D. Veynante, *Theoretical and Numerical Combustion*, 2nd ed. R. T. Edwards, Inc., 2005, ISBN: 9781930217130.

[14] J. Bisson, P. Seers, M. Huegel, and F. Garnier, "Numerical prediction of gaseous aerosol precursors and particles in an aircraft engine," *Journal of Propulsion and Power*, vol. 32, no. 4, pp. 918–928, 2016. DOI: 10.2514/1.B35943.

[15] S. A. Shakariyants, "Flow characteristics in lean direct injection combustors," Ph.D. dissertation, Delft University of Technology, Delft, The Netherlands, 2012, ISBN: 978-94-6191-467-5.

[16] C. M. Madrid, "Chemical reactor network for ldi combustor: Crn development and analysis of different fuels," MSc thesis, Delft University of Technology, Delft, The Netherlands, 2017.

[17] P. Dagaut and M. Cathonnet, "The oxidation of kerosene: Experimental and kinetic modeling study," *Combustion Science and Technology*, vol. 121, no. 1-6, pp. 131–176, 1996. DOI: 10.1080/00102209608951992.

[18] P. Dagaut, B. Fremont, and M. Cathonnet, "Kerosene combustion: Jet-stirred reactor, rapid compression machine, and shock tube studies," *Combustion and Flame*, vol. 130, pp. 197–209, 2002. DOI: 10.1016/S0010-2180(02)00393-4.

[19] J. Warnatz, U. Maas, and R. W. Dibble, *Combustion: Physical and Chemical Fundamentals, Modelling and Simulation*, 4th ed. Springer, 2006, ISBN: 9783540259923.

[20] R. P. Sampat, "Automatic generation of chemical reactor networks for combustion simulations," MSc thesis, Delft University of Technology, Delft, The Netherlands, 2018.

[21] L. F. J. Brink, "Modeling the impact of fuel composition on aircraft engine nox, co and soot emissions," Department of Aeronautics and Astronautics, MSc thesis, Massachusetts Institute of Technology, Cambridge, MA, USA, 2020.

[22] D. Dewanji, "Flow characteristics in lean direct injection combustors," Ph.D. dissertation, Delft University of Technology, Delft, The Netherlands, 2012, ISBN: 978-94-6191-467-5.

[23] J. D. Holdeman, "Mixing of multiple jets with a confined crossflow: A review," NASA Lewis Research Center, Cleveland, OH, USA, Tech. Rep. NASA TM-106055, 1994.

[24] N. Peters, *Turbulent Combustion*. Cambridge, UK: Cambridge University Press, 2000.

[25] H. Pitsch, "Large-eddy simulation of turbulent combustion," *Annual Review of Fluid Mechanics*, vol. 38, pp. 453–482, 2006. DOI: 10.1146/annurev.fluid.38.050304.092133.

[26] P. Moin and S. Apte, "Large-eddy simulation of realistic gas turbine combustors," *AIAA Journal*, vol. 44, no. 4, pp. 698–708, 2006. DOI: 10.2514/1.14606.

[27] International Civil Aviation Organization, *Annex 16 to the Convention on International Civil Aviation, Volume II: Aircraft Engine Emissions*, 4th ed. Montréal, Canada, 2021, Incorporating CAEP/10 and CAEP/11 standards. [Online]. Available: https://www.icao.int/environmental-protection/Pages/Annex-16-Volume-II.aspx.

[28] European Union Aviation Safety Agency, "Introduction to the icao engine emissions databank," EASA, Cologne, Germany, Tech. Rep. TE.GEN.00301-006, 2022. [Online]. Available: https://www.easa.europa.eu/en/downloads/128344/en.

[29] Federal Aviation Administration, *Advisory circular 34-1b: Fuel venting and exhaust emission requirements for turbine engine powered airplanes*, AC 34-1B, issued 27 June 2003, Washington, DC, USA, 2003.

[30] B. C. Singer, R. A. Harley, and A. H. Winer, "Measurement of gas-phase organic compound emission factors from motor vehicles using a flame ionization detector," *Journal of the Air & Waste Management Association*, vol. 46, no. 5, pp. 435–448, 1996. DOI: 10.1080/10473289.1996.10467483.

[31] S. C. Herndon, T. B. Onasch, J. T. Jayne, and et al., "Hydrocarbon emissions from in-use commercial aircraft," *Environmental Science & Technology*, vol. 38, no. 20, pp. 6078–6088, 2004. DOI: 10.1021/es049701q.

[32] K. Schaefer and S. Bartosch, "Empirical correlation of icao emission indices for predictive modeling of gas turbine engines," Deutsches Zentrum für Luft- und Raumfahrt (DLR), Cologne, Germany, Tech. Rep. DLR-IB-325-13-01, 2013.

[33] S. Ravisankar, "Emissions prediction in rql-based aero engines," MSc thesis, Delft University of Technology, Delft, The Netherlands, 2019.

[34] H. C. Mongia, J. D. Holdeman, and P. P. Bennett, "Rql combustor aerodynamics, mixing, and performance," NASA Glenn Research Center, Cleveland, OH, USA, Tech. Rep. NASA CR-201706, 1998.

[35] J. H. Allaire, "Development of a chemical reactor network model for aircraft engine combustors," Ph.D. dissertation, University of Toronto, 2006.

[36] F. Pompei and J. B. Heywood, "The effects of fuel–air mixing on nitric oxide formation in turbulent flames," *Combustion Science and Technology*, vol. 5, no. 5, pp. 257–267, 1972. DOI: 10.1080/00102207208952133.

[37] G. Sturgess, M. Story, and S. Tuttle, "Primary zone fuel–air mixing: Impact on combustion and emissions," in *ASME Turbo Expo*, 2005. DOI: 10.1115/GT2005-68676.

[38] Cantera Project, *Cantera user documentation, detailed reference documentation*, Available at https://cantera.org/stable/reference/index.html, Cantera Developers.

[39] T. Harlass, R. Dischl, S. Kaufmann, *et al.*, “Measurement report: In-flight and ground-based measurements of nitrogen oxide emissions from latest-generation jet engines and 100 % sustainable aviation fuel,” *Atmospheric Chemistry and Physics*, vol. 24, pp. 11 807–11 822, 2024. DOI: 10.5194/acp-24-11807-2024.

[40] R. A. Rudey, “The impact of emission standards on the design of aircraft gas turbine combustors,” *Journal of the Air Pollution Control Association*, 1976, Discusses how combustor inlet temperature, pressure and fuel–air ratio affect emissions and motivated P3T3–type correlations.

[41] D. P. DuBois and G. C. Paynter, “Fuel Flow Method2 for estimating aircraft emissions,” in *SAE Technical Paper Series*, Original description and update of the Boeing Fuel Flow Method 2 (BFFM2), including ambient and humidity corrections, Warrendale, PA, USA: SAE International, 2006. DOI: 10.4271/2006-01-1987.

[42] International Civil Aviation Organization, *Airport Air Quality Manual*. Montreal, Canada: ICAO, 2011, First edition.

[43] D. Poles, A. Nuic, and V. Mouillet, “Base of aircraft data (BADA): Aircraft performance modelling,” EUROCONTROL Experimental Centre, Brétigny-sur-Orge, France, Tech. Rep. EEC Note No. 10/08, 2009, Describes the BADA performance model used as input to many inventory tools that apply P3T3/BFFM2–type correlations.

A

Engine operating-point data for the LTO cycle

This appendix documents the engine operating-point data that were used to construct the chemical reactor network input set for the LTO cycle. The plots are taken directly from project files that were provided by the supervisors and show the variation of compressor outlet pressure P_3, compressor outlet temperature T_3, fuel flow and total core mass flow with thrust setting. These quantities were not available in the ICAO databank but were required to define the boundary conditions of the CRN model for each LTO mode.

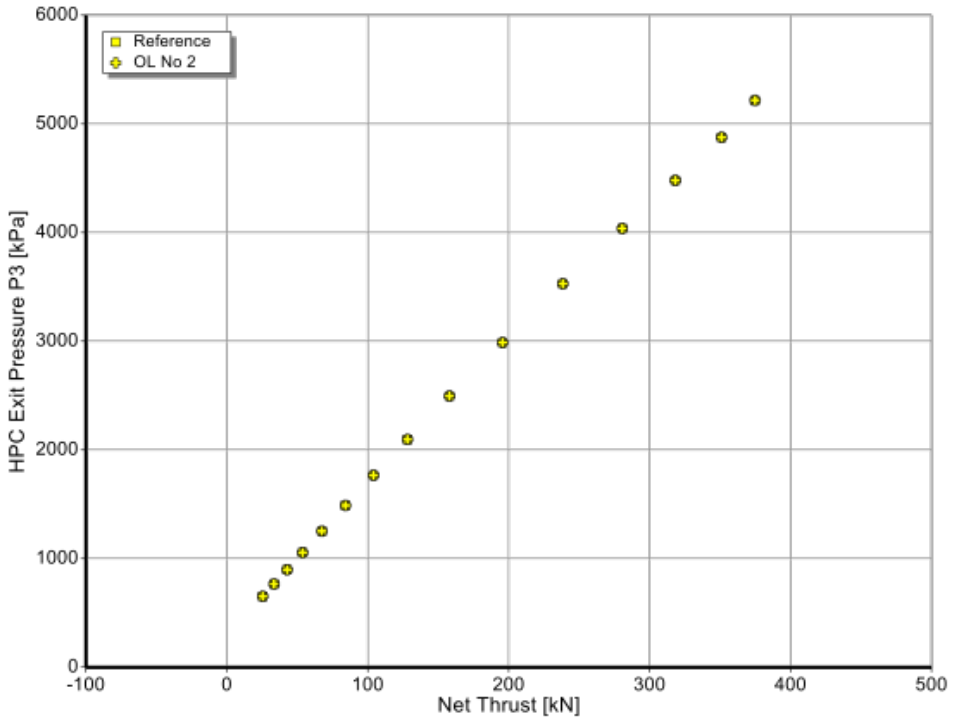

Figure A.1: Variation of compressor outlet pressure P_3 with net thrust for the LTO operating points used in the CRN model.

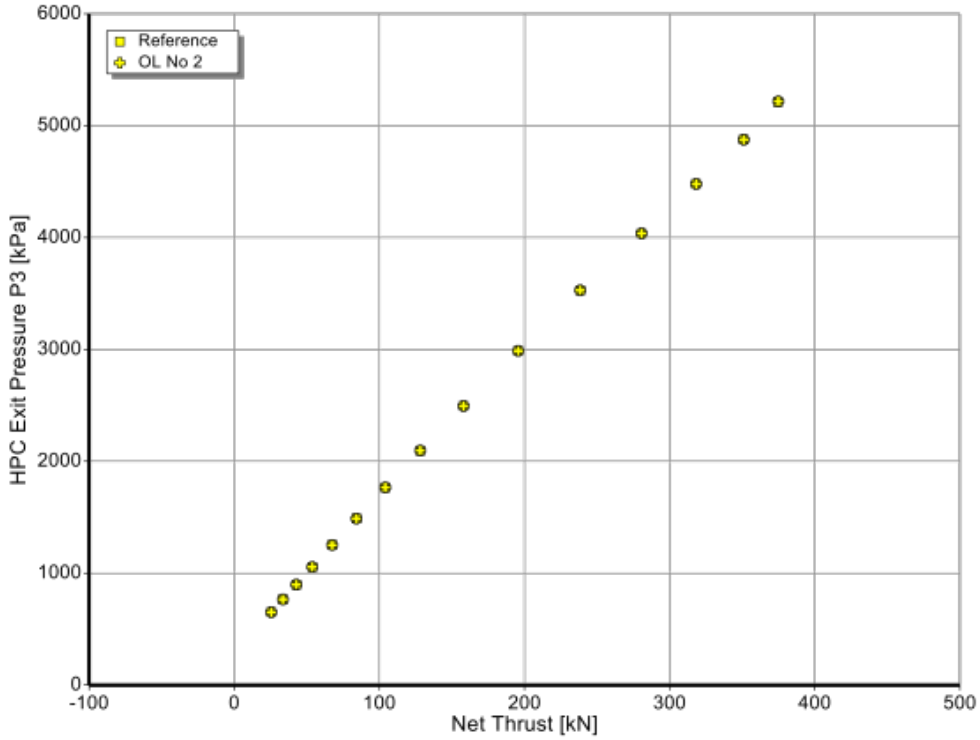

Figure A.2: Variation of compressor outlet temperature T_3 with net thrust for the LTO operating points used in the CRN model.

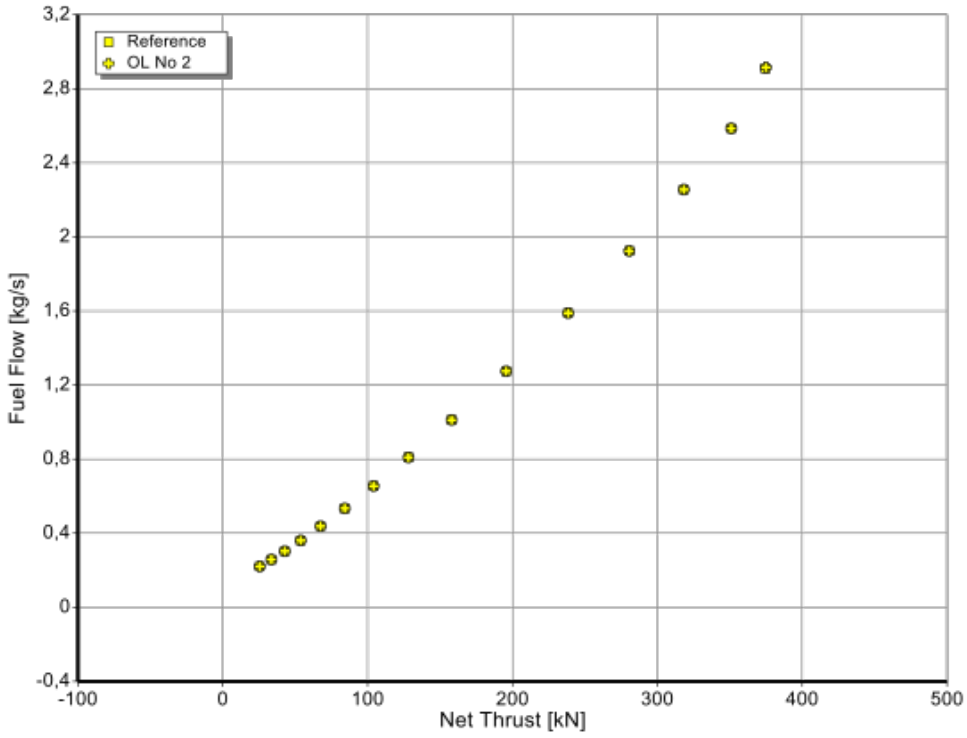

Figure A.3: Variation of fuel mass flow with net thrust for the LTO operating points used in the CRN model.

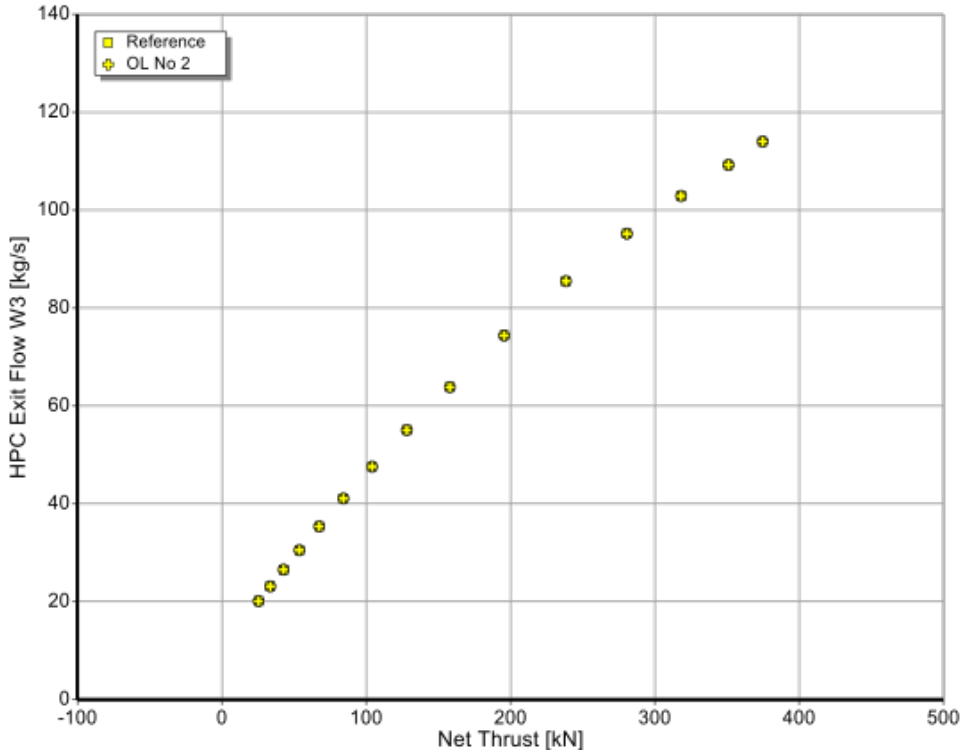

Figure A.4: Variation of total core mass flow with net thrust for the LTO operating points used in the CRN model.

B

Engine operating-point data for cruise conditions

This appendix provides the corresponding operating-point data for the cruise conditions considered in this work. The plots are again taken from the project files provided by the supervisors and show P_3, T_3, fuel flow and total core mass flow as functions of cruise thrust setting. These curves were used to define the boundary conditions of the CRN model at the selected cruise thrust levels (CR60 and CR70), which bracket the expected in-service cruise thrust of the Trent XWB-84.

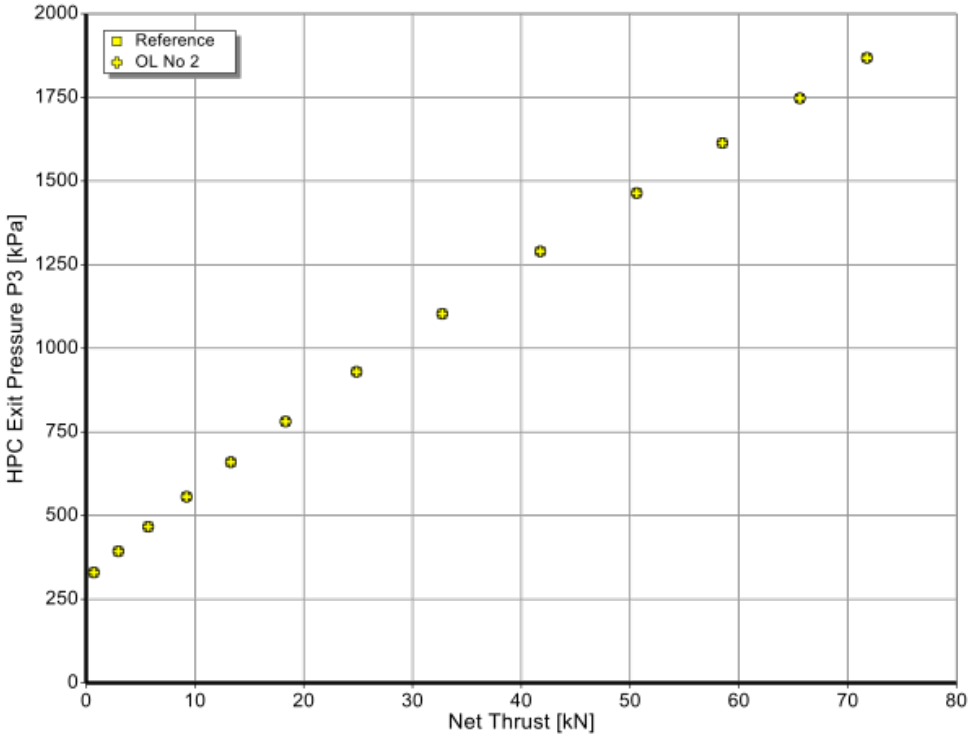

Figure B.1: Variation of compressor outlet pressure P_3 with net thrust for cruise operating points.

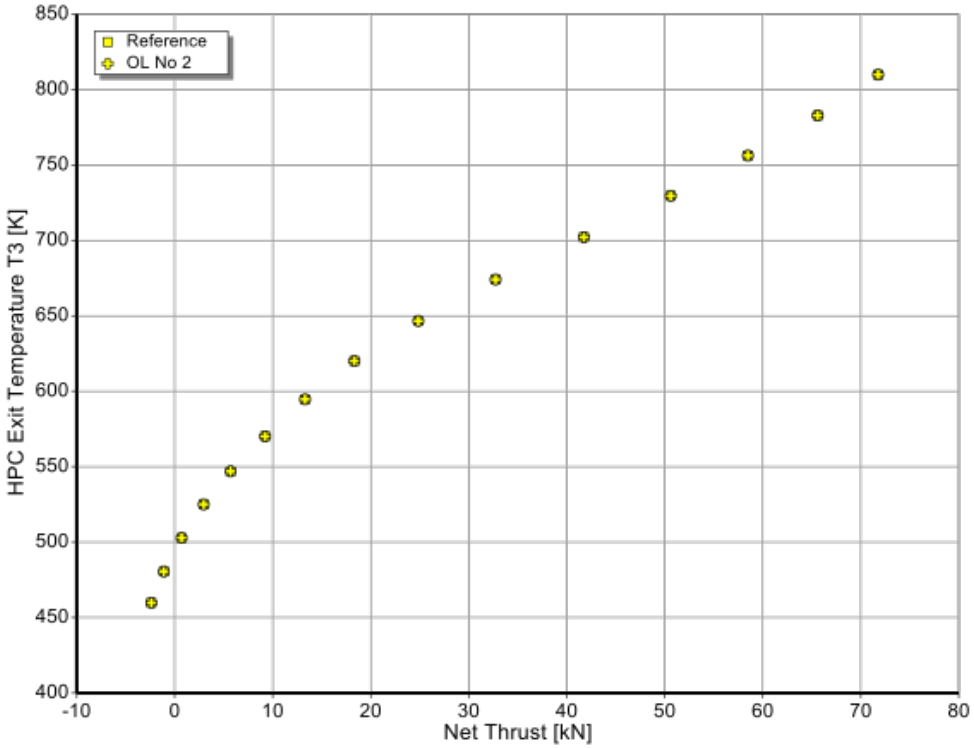

Figure B.2: Variation of compressor outlet temperature T_3 with net thrust for cruise operating points.

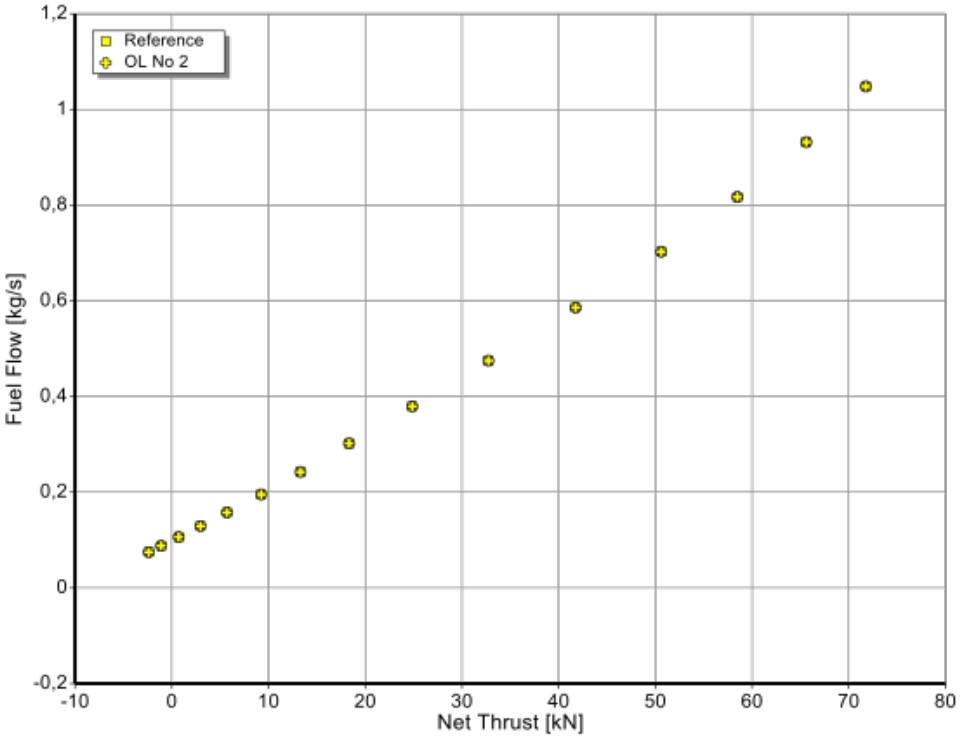

Figure B.3: Variation of fuel mass flow with net thrust for cruise operating points.

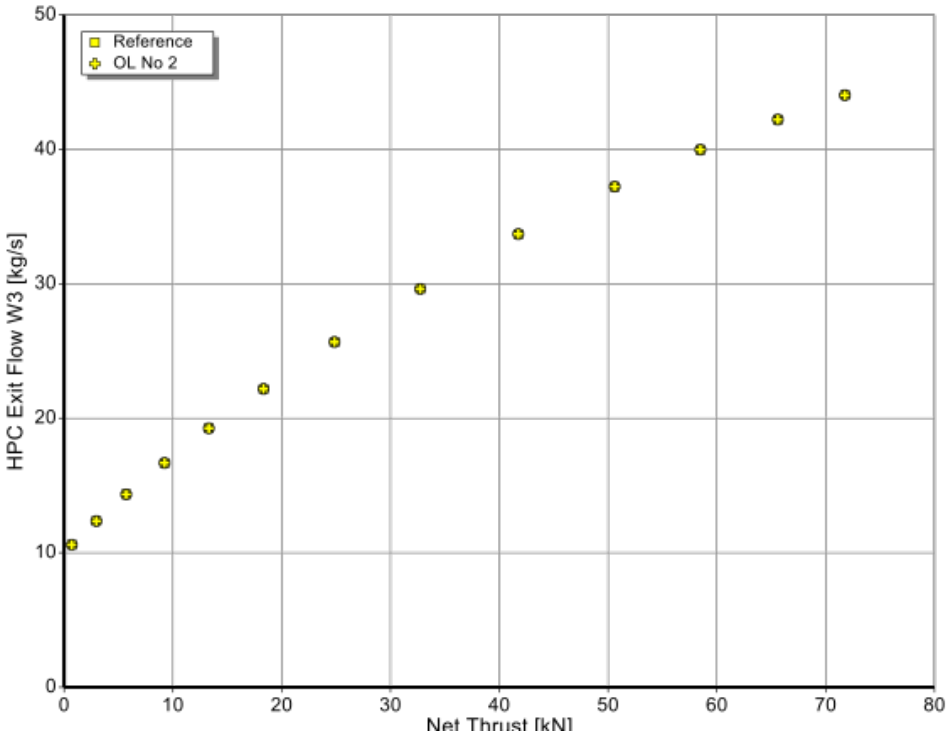

Figure B.4: Variation of total core mass flow with net thrust for cruise operating points.